CORRECTION OF SPHERICAL SINGLE LENS ABERRATION USING DIGITAL IMAGE PROCESSING FOR CELLULAR PHONE CAMERA

ZHANG, Yupeng

February 2011

Waseda University Doctoral Dissertation

CORRECTION OF SPHERICAL SINGLE LENS ABERRATION USING DIGITAL IMAGE PROCESSING FOR CELLULAR PHONE CAMERA

ZHANG, Yupeng

Graduate School of Information, Production and Systems
Waseda University

February 2011

Contents

Preface 5

Abbreviations and Significant Notation 7

Chapter 1 Introduction 11
1.1 History and future of cellular phone camera 12
1.2 Development of lens aberration correction technologies 13
1.3 Application of digital image processing techniques for cellular phone camera 14
1.4 Objectives of this research 15
1.5 Originality of this research 20
1.6 References 21

Chapter 2 Comparison of conventional and new optical imaging systems 23
2.1 Introduction 24
2.2 Structure comparison between conventional and newly proposed optical imaging system 24
2.3 Comparison of optical aberrations between conventional and newly proposed optical imaging system 31
2.4 The feasibility to compensate for single lens aberrations using digital image processing techniques 36
2.5 Conclusion 37

Chapter 3 Correction of distortion 40
3.1 Introduction 41
3.2 Methods 42
3.2.1 Distortion coefficient depending on field angles 42
3.2.2 Comparison between forward and backward mapping methods 43
3.3 Results and discussions 51
3.3.1 Simulation environment and preparation 51
3.3.2 Simulation results and discussions 51
3.4 Conclusion 59
3.5 References 60

Chapter 4 Correction of chromatic aberration 63
4.1 Introduction 64
4.2 Methods 64
The improved chromatic aberration equation for Lateral chromatic aberration (LCA) 64

4.3 Results and discussions 66
4.3.1 Description of simulations 66
4.3.2 Simulation results and discussions 66
4.4 Conclusion 77
4.5 References 77

Chapter 5 Blur restoration for single lens 79
5.1 Introduction 80
5.2 Comparison between Wiener Filter and filter used in this research 81
5.3 Methods 82
5.3.1 Radially variant PSFs 82
5.3.2 Image conversion between Cartesian coordinate system and polar coordinate system 83
5.3.3 PSF conversion between Cartesian coordinate system and polar coordinate system 88
5.3.4 Comparison between traditional BTTB structure and the special BTCB structure of PSF matrix 91
5.3.5 Deblurring of the radially variant blurred image 97
5.4 Results and discussions 97
5.4.1 Deblurring of blurred images produced by 4.5mm double convex single lens 97
5.4.2 Deblurring of blurred images produced by 1.0mm plano-convex single lens 106
5.5 Conclusion 113
5.6 References 114

Chapter 6 Experiment using real single lens system 116
6.1 Introduction 117
6.2 Methods 117
6.2.1 The real double-convex single lens system 117
6.2.2 The improved blur restoration algorithm 119
6.3 Comparison between simulation and experiment results 120
6.4 Discussions and improvement in the future 123
6.5 Conclusion 124

Chapter 7 Conclusions 126

Acknowledgments 128

Achievements 129

Preface

This research introduces lens aberration correction methods using digital image processing for spherical single lens system embedded in cell phone cameras. This provides a new idea for future cell phone camera because the number of lens elements has been reduced to one and the ISP (Image Signal Processor) will process vast data for aberration correction. The current cell phone cameras, however, use compound lens that is three or more elements of lens structure, in which the lens aberrations can be corrected optically but the thickness of the imaging system will unavoidably increase. This newly proposed single lens imaging system can reduce the thickness of the cell phone body to an unprecedented level if proper lens is used, such as high refractive index lens with thinner CT (Central Thickness), while still obtains high quality images with few aberrations provided a powerful real time ISP is embedded. The objective of this research is to realize ultra-thin cell phone camera body (in this research 4.5mm overall thickness from the center of lens' front surface to the image sensor is achieved compared to 7~10mm thickness of this part for most of the current cell phone cameras. We are currently developing a plano-convex single lens system that can further reduce this distance to approximately 1.0 mm), competitive wide field angle (maximum 96 degree, currently is approximately 50 degree or below for normal cell phone cameras) and low optical aberrations achieved by our proposed digital image processing techniques in this research.

However, single lens imaging system results in dramatic aberrations compared to compound lens system in that the latter can reduce or eliminate lens aberrations by assembling together two or more single lenses that have different curvature of surfaces or refractive indices (hence different dispersion of light beams), which should also be aberration complementary. For example, achromatic doublet is utilized to correct chromatic aberrations by attaching a double-convex crown lens which has low refractive index and low dispersion with a double-concave flint lens that have high refractive index and high dispersion; and an anastigmatic optical system can effectively eliminate spherical aberrations, coma and astigmatism by using compound lens groups. Therefore, a single lens imaging system has to rely on other methods to correct aberrations. This research found that the spherical single lens aberrations can be corrected by proposed innovative digital image processing techniques as follows: forward and backward mapping method and field-dependent coefficient method for distortion correction; improved first-order chromatic aberration equations for lateral chromatic aberration correction and the polar coordinate domain deconvolution technique for radially blurred image restoration.

Firstly, forward mapping and backward mapping proposed for distortion correction differ in that the former obtains the distortion-corrected image from the distorted image while the latter maps pixels from a distortion-free, ideal image to a distorted image. We found that the backward mapping is superior to forward mapping because 1) no pixel vacancies will be created after distortion correction, thus the additional interpolation process is unnecessary; 2) higher precision of pixel values is obtainable because bilinear interpolation is used compared to nearest neighbor interpolation used in forward mapping method. The other technique: field angle dependent coefficient, is proposed because the traditional third order distortion component of the Seidel aberration equation is not accurate to represent distortion value for high field angle (e.g. we demonstrated that half field angle 48 degree will result in 0.3710mm deviation from the real distortion value if third order distortion equation is used). As the name suggested, this technique considers distortion coefficient S as a function of field angle (thus the image height) rather than a constant. Simulation results indicated that field angle dependent coefficient method surpasses Seidel aberration third order distortion component, which showed only 5×10^{-4}mm maximum deviation from the real distortion value.

Secondly, we proposed an improved first-order (paraxial) chromatic aberration equation to correct lateral chromatic aberration (LCA). This method suggests that the distance from intersection point of the chief ray and the first lens surface to the optical axis should be a function of real image height of the reference color beams so that the traditional paraxial chromatic aberration equation becomes a higher order polynomial equation. Therefore the accuracy of the real chromatic aberration representation increased compared to traditional first-order equation. Satisfactory results were obtained by image simulation: maximum deviation 2.511×10^{-6}mm from the real LAT values between Fraunhofer F line (486.1nm light beams) and C line (656.2nm light beams) compared to 0.0027mm of the first order case and maximum deviation 2.99×10^{-6}mm from the real LAT values between F line and d line (587.6nm light beams) compared to 0.0019mm of the first order case. The other kind of chromatic aberration: axial chromatic aberration (ACA) cannot be corrected by this technique, because it results in color blur on the image plane, whose correction methods fall into the image deblurring area.

Thirdly, the blur restoration (or deblurring) technique was introduced to solve the problem of radially variant blurring which is inherent defect of spherical single lens system. This is a novel method because the restoration is realized by deconvolving polar blurred image and polar Point Spread Functions (PSFs) converted from Cartesian coordinate system. The merit of this method is that the restoration in polar coordinate domain simplifies the matrix calculation between image and PSF by using locally invariant PSFs. Restoration in Cartesian coordinate domain, however, is very complicated in matrix manipulation because PSFs are spatially variant everywhere. We carried out image simulation on both computer generated gray scale images (produced by 656.3nm light beams) and natural color photographs (produced by light beams ranges from 410nm to 700nm) and the deblurring results were satisfactory.

Finally, a real double convex spherical single lens camera module has been designed and fabricated to testify the aberration correction algorithms proposed in this study. The distortion and chromatic aberration are almost undetectable compared to blur effect due to the limitation of the maximum semi-field angle. Therefore, we only evaluate the blur restoration algorithm on this system. Experiment results suggest that the blur restoration algorithm is also effective for the real system for both monochromatic and RGB images.

Abbreviations and Significant Notation

Abbreviations

ACA	axial chromatic aberration
AE	auto exposure
AF	auto focus
AWB	auto white balance
BFL	back focal length
BTTB	Block Toeplitz with Toeplitz Blocks
BTCB	Block Toeplitz with Circulant Blocks
BCCB	Block Circulant with Circulant Blocks
CT	central thickness
ED	effective diameter
EFL	effective focal length
HMFA	half maximum field angle
ISP	image signal processor
LCA	lateral chromatic aberration
MFA	maximum field angle
MSE	Mean Square Error
PIR	polar image resolution
PSF	point spread function
SVPSF	spatially variant point spread function
SIPSF	spatially invariant point spread function

Significant Notation

Chapter 1

R_1	radius of curvature
P	front principal point
P'	rear principal point
F'	rear foci
ω	half (semi) field angle
FNo.	F number
$\bar{y}'$	paraxial (ideal) image height
f'	effective focal length

Chapter 2

$\bar{y}'$	paraxial (ideal) chief ray height
y'	real chief ray height

Chapter 3

$\bar{y}'$	paraxial (ideal) image height
y'	real image height

$\Delta\, y'_{dist}$	third order distortion
$\Delta\, y'_{dist\_real}$	real distortion
S	distortion coefficient
f'	effective focal length
S'	distortion coefficient determined by visually measuring the distorted image
p_1, p_m	integer pixel in the distorted image
p_{n1}, p_{nm}	decimal pixel around p_1 and p_m in the distorted image
$p_{n'}$	integer pixel in the corrected image
x_1, y_1	coordinate index of pixel p_1
$x_\mathrm{m}, y_\mathrm{m}$	coordinate index s of pixel p_m
x_{n1}, y_{n1}	coordinate index s of pixel p_{n1}
x_{nm}, y_{nm}	coordinate index of pixel p_{nm}
$pv_1,\ pv_m$	pixel value of p_1 and p_m
$pv_{n1},\ pv_{nm}$	pixel value of p_{n1} and p_{nm}
$pv_{n'}$	pixel value of $p_{n'}$

Chapter 4

$\Delta s'_{FC}$	first order ACA between Fraunhofer F line and C line light beams
$\Delta s'_{Fd}$	first order ACA between Fraunhofer F line and d line light beams
β	magnification of the lens system
Δf_{FC}	displacement of focal lengths between F and C line light beams
Δf_{Fd}	displacement of focal lengths between F and d line light beams
$\Delta y'_{FC}$	first order LCA between F line and C line light beams
$\Delta y'_{Fd}$	first order LCA between F line and d line light beams
$\Delta y'_{FC\_real}$	real LCA between F line and C line light beams
$\Delta y'_{Fd\_real}$	real LCA between F line and d line light beams
$k_1,\ k_2$	first order chromatic aberration coefficients
f_d	focal length of the reference ray
h^*	distance from the intersection point of the chief ray and the first lens surface to optical axis
$Dev_{FC},\ Dev_{Fd}$	deviation between LCA calculated by first or third order equation and real LCA

Chapter 5

$[H]$	matrix of the point spread function
$[\phi_f]$	signal convariance
$[\phi_n]$	noise convariance
$*t$	conjugate transpose
γ	reciprocal Lagrangian multiplier
$[Q]$	linear operator
$[I]$	identity matrix
$gc_{i,j}$	Cartesian pixel of the blurred image, whose index is (i ,j)
$gp_{r,\theta}$	polar pixel of the blurred image, whose index is (r; θ)

i_c, j_c	index of Cartesian image center on image coordinate system
q	number of equal parts that the whole circle of polar coordinate system is divided
r', θ'	polar image index on PSF coordinate system
i', j'	Cartesian image index on PSF coordinate system
$r_{\mathrm{psfo}}, \theta_{\mathrm{psfo}}$	index of polar PSF origin on image coordinate system
$r'_{\mathrm{psfo}}, \theta'_{\mathrm{psfo}}$	index of polar PSF origin on PSF coordinate system
i_{psfc} , j_{psfc}	index of Cartesian PSF center on image coordinate system
i'_{psfc}, j'_{psfc}	index of Cartesian PSF center on PSF coordinate system
$r_{\mathrm{o}}, \theta_{\mathrm{o}}$	index of polar image origin on image coordinate system
β	bandwidth of the BTCB matrix
$\tilde{F}$	deblurred image column vector
T	PSF BTCB matrix
α	regularization parameter
L	BTCB matrix of regularization operator
$\tilde{F}_e$	extended deblurred image column vector
C_T	BCCB matrix padded from T
C_L	BCCB matrix padded from L
G_e	extended blurred image column vector
Ft	unitary discrete Fourier transform matrix
Λ_T, Λ_L	diagonal matrices including the eigenvalues of C_T, C_L
c_T	the first column of C_T
c_L	the first column of C_L
$./$	component-wise division
$.\bullet$	component-wise multiplication

Chapter 6

r	dimension of semi-diagonal
f	effective focal length
θ	maximum semi-field angle
i_c, j_c	index of Cartesian image center on image coordinate system
q	number of equal parts that the whole circle of polar coordinate system is divided
k	variable that determines radial resolution of the blurred polar image
r', θ'	polar image index on PSF coordinate system
i', j'	Cartesian image index on PSF coordinate system
$r_{\mathrm{psfo}}, \theta_{\mathrm{psfo}}$	index of polar PSF origin on image coordinate system
$r'_{\mathrm{psfo}}, \theta'_{\mathrm{psfo}}$	index of polar PSF origin on PSF coordinate system
i_{psfc} , j_{psfc}	index of Cartesian PSF center on image coordinate system
i'_{psfc}, j'_{psfc}	index of Cartesian PSF center on PSF coordinate system

Chapter 1 Introduction

Chapter 1 Introduction

1.1 History and future of cellular phone camera

The world first camera embedded cellular phone, named VP-210, was designed and manufactured by Kyocera, and was pushed to the cell phone market by Willcom in Sep.,1999. Although the integrated camera has very low specifications compared to present cell phone cameras such as a resolution of 110,000 pixels (0.1Megapixels) CMOS image sensor, it indeed marked the beginning of a new era of cellular phone. It then followed by J-SH04 designed and manufactured by SHARP, which is also a 0.1 Mega CMOS sensor camera phone. From then on, competitors proposed high spec integrated cameras successively and their performance are approaching the level of stand-alone digital cameras. Nowadays, most of the cell phones have at least one integrated camera with at least 3Megapixels image sensor and other features such as optical or digital zooming, wide view angle, auto exposure (AE), auto focus (AF), auto white balance (AWB) and the image stabilization functions, etc. It can be predicted that the future cell phone camera should have higher resolution, wider view angle, lower power consumption and more features that enable high quality photographing.

Although the performance of the current integrated cameras in cell phones is comparable with that of the stand-alone digital cameras, people neglect one important factor: thickness of the imaging system will increase correspondingly, which is undesirable in case of cell phone camera. Almost all current cell phone cameras adopt the compound lens structure which consists of fixed or movable single lens elements. The main reason to use compound lens is that the optical aberration can be effectively reduced or eliminated. For example, an achromatic doublet lens can minimize chromatic aberration because a pair of aberration complementary lenses is used: a double convex crown lens with low refractive index and low dispersion and a double-concave flint lens that have high refractive index and high dispersion. An anastigmatic optical system, which consists of several compound lenses between which there is always space, can effectively eliminate spherical aberrations, coma and astigmatism. The other purpose is to realize optical zooming. Like stand-alone digital cameras, this feature already becomes a standard requirement for cell phone camera. However, it needs an additional space for the movable lens that is driven by a motor, which further increases overall thickness. On the other hand, high power consumption cannot be avoided if the driving mechanisms are not miniaturized for cell phone camera. Therefore, the total compound lens imaging system cannot be made very thin.

Future cell phone cameras have to take the thickness and power consumption into consideration. To reduce the thickness of the camera lens system, many novel ideas have been proposed during the last decades. One idea is to use liquid lens instead of glass or plastic lens. French company Varioptic has designed a tunable-focal length liquid lens that incorporates zooming function without enlarging the overall size of the lens system [1-1]. The zoom function is based on “electrowetting” technology and realized by applying different voltages to electrodes beside which there are two immiscible liquids: water (conducting liquid) and oil (insulating liquid). The liquid lens shows divergent characteristic when 0V is applied while convergent characteristic when 40 V is applied. S. Kuiper and B.H. W. Hendriks in Philips proposed a similar liquid lens camera in which the voltage for modifying the focus length ranges from 0~50V [1-2]. Those liquid lens systems have the merit to reduce the camera thickness and power consumption because the zoom function is not realized by driving a moveable lens. However, some drawbacks also prevent them from mass production: 1) the difficulty of mass production, which leads to high manufacturing cost; 2) temperature dependency has to be taken into account. Weisong Wang has presented another focal length adjustable system that does not use a mechanical driving force but a flexible polymer microlens that can change its shape. The lens shape changes when a microheater heats up a thermal fluid under the microlens by applying voltage to the

heater [1-3]. The focal length is then changeable because the lens curvature changes. The other proposal is to use miniaturized camera module specifically designed for cell phone camera. This has been well studied and new technologies have been proposed to replace old ones: such as linear motor, voice coil motor and piezoelectric motor to replace DC motor and step motor. For instance, a small autofocus (AF) actuator for cell phone camera using conductive polyimide as a flexible diaphragm has been proposed, which shows an overall size of only 10×10×3.95mm and low power consumption [1-4]. Besides, another promising approach was born recently to reduce the thickness of cell phone camera: the use of aspherical lens. Since the non-spherical surface of the lens, spherical aberration is avoidable by a single aspheric lens. Correction of coma, astigmatism, field curvature, distortion and chromatic aberration, however, has to rely on stacking additional lenses to the lens system [1-5] [1-6]. The cost of manufacturing, which was a barrier that prevent aspherical lens from mass production previously, can be reduced now by using plastic lens rather than glass material. Moreover, the liquid lens, deformable lens and the miniaturized camera module mentioned above all can be combined with the aspherical lens to further reduce the overall thickness.

The above proposed future lens systems all provided possible ways to reduce thickness and power consumption of the camera system, though there are some drawbacks. Most of them successfully reduced the overall thickness and realized AF and zooming features, but the optical aberrations of those systems are not well addressed and evaluated. In this research, we propose another novel approach for future cell phone camera that uses only one element of spherical single lens. The proposed single lens system can reduce the system thickness and correct optical aberrations by digital image processing techniques. In the future, this aberration correction method could be realized by the cell phone ISP. And the AF feature is also feasible for this system by slightly moving the single lens element along the optical axis but the optical zooming feature is not possible, which poses a new topic for the future development of this system. However, we can use digital zooming to replace optical zooming at this stage.

1.2 Development of lens aberration correction technologies.

Lens aberrations (or optical aberrations) exist for almost all kinds of lens. It is a phenomenon that light from a point source on the object side of the imaging system fails to converge to single point on the image plane at the image side. Generally, there are two categories of aberrations: monochromatic aberration and chromatic aberration (or polychromatic aberration). The first category, which is produced from mono-wavelength light beams, consists of spherical aberration, coma, astigmatism, field curvature and geometrical distortion. The second category, including axial chromatic aberration (ACA) and lateral chromatic aberration (LCA), comes from light beams with wide range of wavelengths. The degree of aberrations for a lens depends on two main factors: 1) lens effective diameter (ED); 2) field angle [1-7]. The larger the value of ED or field angle, the stronger the aberrations appear on the image plane.

Conventional approaches of aberrations correction rely on careful optical design. The compound lens mentioned in section 1.1 can effectively minimize all sorts of aberrations if appropriate lens is selected. Spherical aberration can be minimized by using aspheric lens, gradient index (GRIN) lens, symmetric doublets and plano-convex lens which its convex surface faces the light source. Coma can be corrected by spaced doublet with central stop. Astigmatism, Petzval field curvature could also be minimized using spaced doublet. Besides, spherical aberration, coma and astigmatism can be eliminated simultaneously by using anastigmatic optical system. Distortion correction can be achieved by symmetric doublet such as orthoscopic doublet. As to chromatic aberrations, achromatic doublet could minimize them effectively. It should be emphasized that aberration correction by optical means is never limited to the approaches mentioned above. New types of lens, new materials and new combination of lenses are proposed continuously in this field. For instance, hybrid lens containing

fluorite is proved to be highly effective for chromatic aberration correction, the superachromat commonly use such a hybrid lens to achieve the best chromatic aberration correction effect for a wide range of wavelengths (between 365nm and 1014nm)[1-8]. Diffractive optical elements that are highly dispersive are also proved to be effective for chromatic aberration correction [1-9].

In recent years, another approach of aberration correction has seen rapid development: the digital image processing techniques. Correction software as a post processing method for computer or digital cameras has already been released nowadays. For example, PT Lens is a lens aberration correction software that can correct barrel and pincushion distortion, lateral chromatic aberration. It also incorporated features such as correction of vignetting and perspective, etc. The famous image processing software Photoshop also incorporated similar features. Blur can also be restored by software such as Focus Magic, which can correct not only defocused image but also motion blurred image. On the other hand, some compact digital camera has already incorporated automatic correction of lens aberrations such as Nikon's DSLR series.

In this research, we also propose digital image processing methods to correct lens aberration, but they are specifically designed for a spherical single lens imaging system, strictly adhere to the performance of the designed single lens. The final objective of our research, however, is to realize real time aberration correction using image signal processor (ISP) embedded in a cell phone camera, though it is not possible by using present technology (especially blur restoration for radially variant blurred image which will be introduced in detail in Chapter 5). The main reason lays in that the current ISP is not powerful enough to process vast data required for the corrections. Therefore, the proposed methods were evaluated by software simulation and experiment using PC at this stage.

1.3 Application of digital image processing techniques for cellular phone camera.

Digital image processing technology has seen great development since 1960s, in which period the photograph of Mars taken by NASA's Marinet 4 used this technology for the first time in human history. The application fields of digital image processing cover space exploration, satellite remote sensing (such as Earth Resources Technology Satellite or ERTS), Geographical Information System(GIS), medical imaging diagnostic system (such as CT, MRI, X-ray etc.), car navigation system, stand-alone digital camera, handheld device with embedded camera, Computer Graphics, Virtual Reality, Artificial Intelligence, and so on [1-10].

In digital cameras or portable devices with embedded camera such as cell phone cameras, digital image processing already becomes the indispensable technology. Digital image processing is achieved by image signal processor or ISP in digital cameras and cell phone cameras. As to the current ISP, the main features include color interpolation or RGB interpolation, color correction, gamma correction, color conversion, AE/AWB/AF control, lens shading correction, dynamic control, noise reduction, image stabilization, etc. Unlike traditional digital camera, cell phone camera needs CMOS sensor rather than CCD sensor to lower the power consumption and sensor size. Unfortunately, CMOS sensor has its inherent defect that results in poorer image quality than CCD sensors [1-11]. Therefore, those features of ISP mentioned above are more important to ensure good quality of image for CMOS sensors. Many novel ideas have been proposed regarding the design and manufacturing of ISP for CMOS sensors. A real-time image enhancement preprocessor for CMOS image sensor with 0.6μm technology was proposed ten years ago by Korean researchers. The proposed processor incorporates a spatially adaptive contrast enhancement block with other feature blocks such as color interpolation, color correction, gamma correction and automatic exposure control. The preprocessor built on FPGA chip operates at 30 frames/sec so that real time is achievable [1-12]. Kim Kimo and In-Cheol Park investigated a similar signal processor for CMOS sensor with 0.18μm technology, in which they combines white balancing, color correction and color conversion blocks into single block. This significantly reduced hardware area and power consumption by 23.8% and 31.1%, respectively,

without perceptible performance degradation [1-11].

On the other hand, the aberration correction features are seldom embedded in current ISP because aberrations are almost minimized by using compound lens. However, there are still some approaches proposed to further enhance image quality by digitally compensating for aberrations, but most of them incorporate only one correction block. The ISP designed exclusively for single lens imaging system of cell phone needs more than one image processing blocks for aberration correction because aberrations are extremely intensive compared to compound lens system. It should include distortion correction block, chromatic aberration block and the blur restoration block, together with the main image processing blocks mentioned in previous paragraph. We will describe the methodologies for these aberration correction features in the following chapters in detail.

1.4 Objectives of this research

One objective of this research is to design a spherical single lens imaging system to replace the compound lens system so that the thickness of the cell phone camera can be reduced. The other objective is to design aberration correction methodologies for geometrical distortion, chromatic aberration and radially variant blurring using digital image processing. The final destination: realizing a real-time correction ISP for single lens cell phone camera, is not possible at the time of writing because the limitation of ISP processing capability.

The design objective of single lens should meet the following requirements: 1)spherical lens with double convex or plano-convex surfaces; 2) glass material with high refractive index therefore short focal length is achievable; 3) high field angle; 4)central thickness should also be thin enough so as to reduce overall height of the cell phone camera module.

A cross section of the single lens used throughout this research is illustrated in Fig.1.1 and its specifications are shown in Tab.1.1

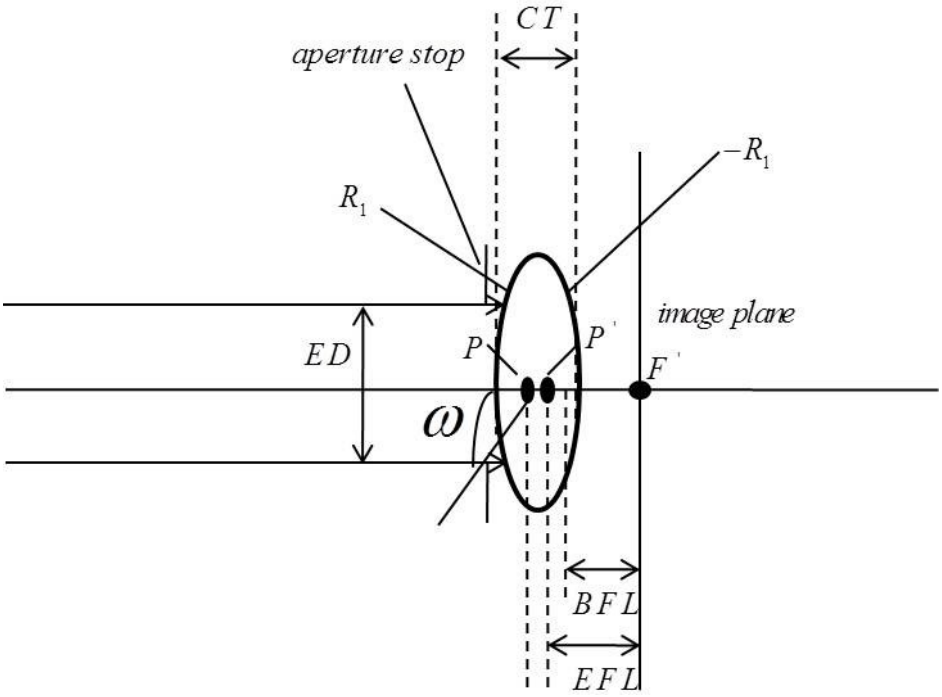

Fig.1.1 Spherical double convex single lens design

The corresponding lens specification is listed in Tab.1.1

Tab.1.1 Singlet lens specification

ED(mm)	0.94
CT (mm)	2.3
EFL (mm)	3.0
BFL (mm)	2.21
$R_1 = -R_1$ (mm)	3.5
Half Maximum Field Angle (degree)	48
FNo.	3.2
Glass	SF5

The meaning of each notation in Fig.1.1 and Tab.1.1 is as follows:
ED: Effective Diameter or entrance pupil
CT: Central Thickness
EFL: Effective Focal Length
BFL: Back Focal Length
R_1: Radius of curvature
P : Front principal point
P': Rear principal point
F': Rear foci
ω: Half field angle

On the position of image plane, a virtual image sensor is positioned, whose diagonal size and pixel size can be detected by CODE V after the above lens specifications are determined. For distortion correction, we assume a 8 Mega (3264×2448) image sensor (Fig.1.2) with pixel size $1.4\mu\text{m} \times 1.4\mu\text{m}$ in order to evaluate proposed method for high resolution image. For chromatic aberration correction, we attached a virtual square image sensor whose dimension is $4.1\text{mm} \times 4.1\text{mm}$ and each pixel has a $5.3\mu\text{m} \times 5.3\mu\text{m}$ dimension. The resolution of the virtual sensor reduced to 768×768 because of the processing time on the image simulation stage. It will take less than 2 minutes to correct an image with chromatic aberrations at this resolution, while it will take hours to process a high resolution image. For example, we have measured that about 1 hour and 40 minutes is needed to process a 8 Mega (3264×2448) image. The image sensor used in blur restoration also has a square area, (refer to Fig.1.4) and low resolution virtual image sensor (1024×1024) is used due to fast processing speed compared to high resolution image. The sensor size is smaller than previous two sensors. Note that the semi-diagonal corresponds to the half maximum field angle (HMFA) for all three cases. However, HMFA is only 21 degree in Fig.1.4 due to software limitation. This will be explained in Chapter 5.

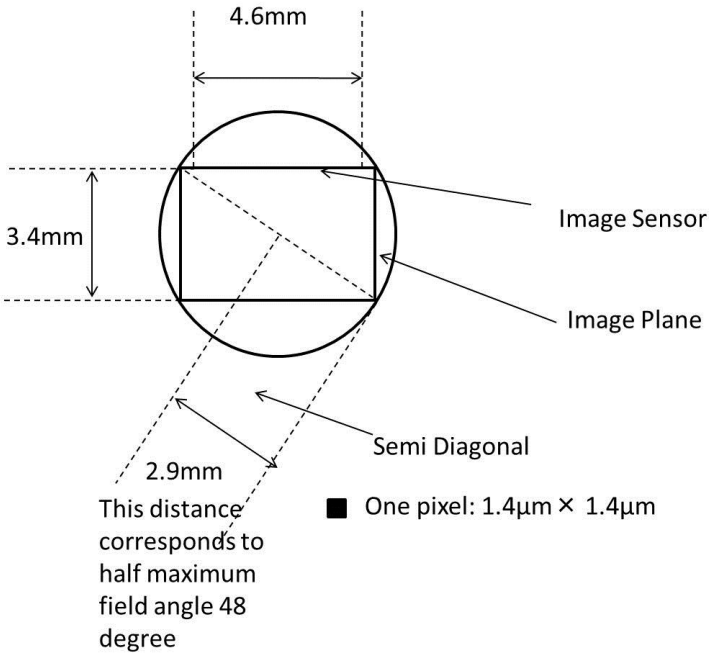

Fig.1.2 Image sensor used in distortion correction

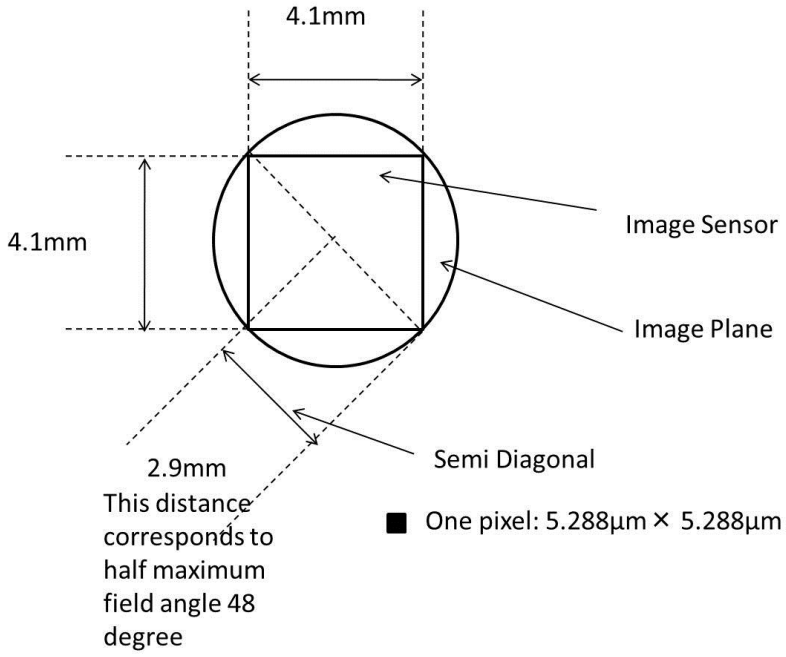

Fig.1.3 Image sensor used in chromatic aberration correction

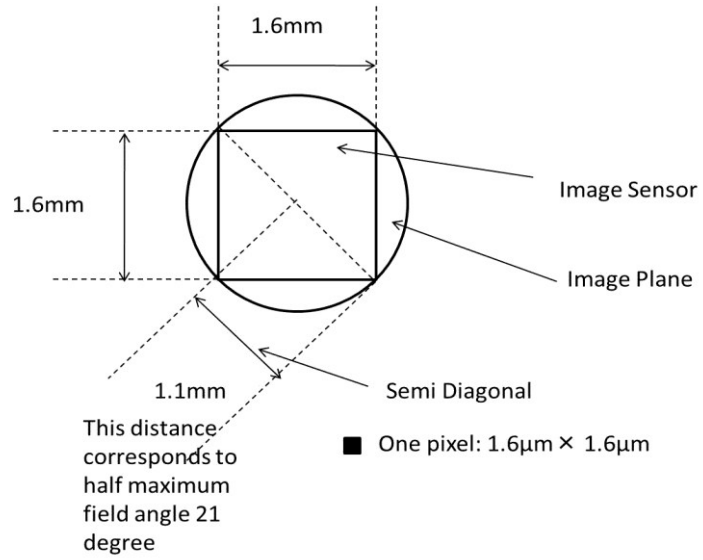

Fig.1.4 Image sensor used in radially variant blur restoration

It should be emphasized that EFL, BFL and *FNo.* in Tab.1.1 are measured and calculated in terms of d line of Fraunhofer Lines light beams, whose wavelength is 587.6nm. It is therefore the reference ray for further analysis of our single lens system throughout this research. Other wavelengths will slightly modify those values. Additionally, the object distance is regarded as infinite.

It is necessary to explain how the lens parameters in Tab.1.1 are determined. The ED, CT, EFL, BFL, R_1 and glass material in Tab.1.1 are determined by referring up to date commercial lens catalogue and selected the parameters that are most suitable for future cell phone camera size. The reason of choosing SF5 rather than BK7 is that the former possesses higher refractive index that is easier to bend light beams than the latter, which can shorten the distance between foci and lens, hence shorten the overall height of the imaging system. *FNo.*in Tab.1.1 is determined by the following equation

$$FNo. = \frac{EFL}{ED} \tag{1.1}$$

The determination of half maximum field angle can be divided into two steps:
Step 1. Calculate maximum field angle using paraxial equation for infinite object

$$\bar{y}' = f'\tan\omega \tag{1.2}$$

where $\bar{y}'$ indicates paraxial image height, f' is the effective focal length (EFL) and ω is the half field angle. The equation with respect to half maximum field angle can then be derived from (1.2)

$$\bar{y}'_{\max} = f'\tan\omega_{\max} \tag{1.3}$$

where in this case $\bar{y}'_{\max}$ equals half of the diagonal of the image plane.
In our case,

$$\omega_{\max} = \arctan\left(\frac{\bar{y}'_{\max}}{f'}\right) = \left(\frac{2.9}{3}\right) = 44.03 \text{ degree}$$

Step 2. Determine real maximum field angle by examining if the output image fit to the size of image sensor perfectly.

Although the maximum field angle for paraxial case has been calculated, the real maximum field angle should not equal to this because the accuracy of the paraxial equation (1.2) will fall dramatically as the field angle increases. As a result, the output image will not fit to the image sensor perfectly. (For example, the semi-diagonal is 2.58mm and the pixel size is 4.75μm× 4.75μm for the chromatic aberration correction if we use 44.03 degree as the maximum field angle.) Therefore, we increased the half field angle and found that when the angle increases to 48 degree, the output image size and the image sensor size will perfectly match.

On the other hand, these requirements of specification for future cell phone camera are actually contradictory because decreasing the thickness of the lens system will lead to larger maximum field angle, which consequently increases optical aberrations. This can be proved via equation (1.3) and the property of single lens. From equation (1.3) we could tell that increasing maximum field angle will lead to shorter EFL, which means the thickness of the lens system is reduced. However, this is where the problem begins. According to property of single lens, the optical aberrations will increase as the field angle increases. And most importantly, the paraxial aberrations and the famous third order Seidel aberrations are no longer applicable in terms of large field angle. In other words, we could not use paraxial aberration equations or third order Seidel aberration equations to correct optical aberrations any more. This is easy to understand because the paraxial aberrations and Seidel aberrations are all derived by approximating Snell's Law ($n\,sin\,\theta = n'\,sin\,\theta'$), the difference lays in that the former is a first order approximation ($n\,\theta = n'\theta'$) and the latter uses more accurate third order approximation $n(\theta - \theta^3/3!) = n'\left(\theta' - \theta'^3/3!\right)$.We can examine the deviations of the first order approximation and the third order approximation from the sinusoidal function for different angles in Tab.1.2. Obviously, larger angle results in greater deviations. The deviation of the third order approximation is smaller than that of the first order approximation.

Tab.1.2 Sinusoidal function and its first order and third order approximations

θ(degree)	$sin\,\theta$	θ(rad)	$\theta - \theta^3/3!$
1	0.0175	0.0175	0.0175
3	0.0523	0.0524	0.0523
5	0.0872	0.0873	0.0872
10	0.1736	0.1745	0.1736
15	0.2588	0.2618	0.2588
20	0.3420	0.3491	0.3420
30	0.5000	0.5236	0.4997
50	0.7660	0.8727	0.7619

Because of the above reason, the calculation results of paraxial aberration and third order aberration will deviate too much from the real aberration value of the lens system in case of large field angle, which increases the difficulty of aberration correction problem. To deal with the problem, we have to modify the first order and third order aberration equations to make them applicable to large field angle. In Chapter 3 and 4 we introduce an improved distortion term of the third order Seidel aberration equation using field-dependent coefficient for distortion correction and an improved first order equation for lateral chromatic aberration correction, respectively.

Therefore, the objectives of distortion correction and chromatic aberration correction are to find out higher order equations that can accurately represent real aberration values, which will be far more

accurate than values calculated by traditional paraxial and third order Seidel equations so as to obtain satisfactory results both visually and quantitatively. On the other hand, the objective of radially variant blur restoration is to investigate a polar domain locally invariant PSF restoration method that can simplify the matrix manipulation between image and PSF. In the following chapters, the proposed algorithms for the three aberration correction tasks will be introduced and evaluated in detail.

1.5 Originality of this research

As we already introduced in section 1.1, there are several approaches to realize future cell phone camera system that is not only in small dimension, requires low power consumption, but also incorporates optical zooming and AF features. However, there is no such literature that depicts a single lens imaging system in camera, not even in conventional digital camera, because it is well known that this system can introduce significant optical aberrations. Therefore, it is very meaningful to propose an optional approach for future cell phone camera, design such a system and investigate original methods exclusively for single lens system to solve the aberration correction problems.

Therefore, the originality of this research can be concluded as follows:

1) Single lens structure

   Current and most of the proposed future cell phone camera include more than one lens element to correct aberrations optically, even though they use liquid lens or aspheric lens etc. to reduce overall thickness. The proposed system, however, use one element of spherical double convex single lens and no additional lens are required.

2) Improvement of traditional third order Seidel aberration equation and paraxial chromatic aberration equation

   Unlike compound lens system, the single lens system will produce intensive aberrations, especially at high field angle. The difficulty of aberration correction for single lens requires improvement of current aberration equations. Since the maximum field angle of the lens system reaches 96 degree, Seidel third-order aberration equation is not able to accurately represent real distortion value. We found that the relationship between distortion coefficient and paraxial image height can be better represented by a third order polynomial equation. The paraxial image height is also a function of field angle. So the field angle dependent distortion coefficient method was devised. The other method proposed is the backward mapping method, which is directly influenced by the obtained field angle dependent coefficient polynomial.

   As to the chromatic aberration correction, the maximum field angle is also 96 degree, the traditional paraxial chromatic aberration equation (or first order equation) is not applicable in this case. It is found that the distance from the intersection point of chief ray and first lens surface to the optical axis can be considered as a function of real image height. Therefore, we improved the first order equation and found that the relationship between them can be better represented by third order polynomial.

3) Deconvolution between polar blurred image and polar PSF for the restoration of radially variant blurred image produced by the single lens system

   Researchers have already studied one kind of radial blur caused by moving the camera perpendicular to the object, but few have studied on the radial blur caused by inherent defect of a single lens system. Because of the special distribution of blur: a radially variant blur produced by spherical single lens, we considered a new method of blur restoration. Compared to traditional

method that deconvolves blurred image and PSF in Cartesian coordinate, the proposed method carries out deconvolution using polar blurred image and polar PSF. The proposed method can simplify matrix manipulation between image and PSF due to the use of locally invariant PSFs.

Finally, it should be emphasized that the current system requires further development such as incorporating optical zooming feature. In addition, the current research has already proved to be successful at the simulation stage, which will be introduced in the following chapters. It is expected that the proposed methods can be implemented on a real-time ISP of cell phone in the future.

1.6 References

[1-1] K. Tatsuno, "Current trends in digital cameras and camera-phones", Sci. Tech. Trends - Q. Rev.18 (1) 35–44 (2006) Original Japanese version published in July 2005.

[1-2] Kuiper, S. & Hendriks, B. H. W. "Variable-focus liquid lens for miniature cameras", Appl. Phys.Lett. 85, 1128–1130 (2004)

[1-3] W.S. Wang, J. Fang, K. Varahramyan, "Compact variable-focusing microlens with integrated thermal actuator and sensor", IEEE Photon. Technol.Lett. 17, 2643–2645 (2005)

[1-4] B.Y.Song, D.S. Nam, " Auto-focusing actuator and camera module including flexible diaphragm for mobile phone camera and wireless capsule endoscope", Special Issue on 18th ASME Annual Conference on Information Storage and Processing Systems, Santa Clara, CA, USA, 16–17 June (2008)

[1-5] S. Ozawa, T. Yuasa, R. Yoshida, K. Matsusasa, "Development of an ultra-compact zoom lens unit for camera phones", KONICA MINOLTA TECHNOLOGY REPORT, VOL.478–81(2007) (In Japanese)

[1-6] S. Ooshima, T. Tanaka, "Hikyumen renzu Gijutsu", television gakaishi vol.42, No.9, 937-944 (1988) (In Japanese)

[1-7] Kishikawa T. "Kougaku Nyumon", Optronics Press; (1990) (in Japanese)

[1-8] M. Zając, J. Nowak, "Correction of chromatic aberration in hybrid objectives, Optik", vol. 113 299-203 (2002)

[1-9] A. Pe'er, D. Wang, A. W. Lohmann, and A. A. Firesem, "Apochromatic optical correlation," Opt. Lett. 25, 776–778 (2000).

[1-10] M. Takagi, H. Shimoda, "Handbook of Image Analysis", University of Tokyo Press, Tokyo, (1991)(in Japanese)

[1-11] K. Kim, In-Cheol Park, "Combined image signal processing for CMOS image sensor", IEEE International Symposium on Circuits and Systems, 2006. ISCAS 2006. Proceedings(2006)

[1-12] Y. Ho Jung, J. Seok Kim, B. Soo Hur, A. Moon Gi Kang, "Design of real-time image enhancement preprocessor for CMOS image sensor", IEEE Transactions on Consumer Electronics 46 (1), 68–75(2000)

Chapter 2 Comparison of conventional and new optical imaging systems

Chapter2 Comparison between conventional and new optical imaging systems

2.1 Introduction

In Chapter 2, the merit and demerit of the newly proposed single lens imaging system will be depicted and compared with the conventional compound lens imaging system. Firstly, we illustrate some patent lens systems that use compound lens structure and specify their overall thickness and maximum field angle. In comparison, we also give some single lens system with double convex or plano-convex single lens element that is selected from up-to-date commercial lens catalogue in order to show theoretically how slim the proposed single lens system could be made. Secondly, in order to show how strong the aberration of single lens systems compared to compound lens systems, the aberration of both systems will be illustrated and compared quantitatively by using aberration curves and visually by PSF distribution image and 2D image simulations. Finally, we give some simulation results using our proposed aberration correction methods by digital image processing to indicate the feasibility to compensate for single lens aberrations, even if the conventional optical method is not used.

2.2 Structure comparison between conventional and newly proposed optical imaging system

This section compares structures of many types of patent compound lens systems used in digital cameras with the newly proposed single lens systems.

First of all, three compound lens systems are selected. The lens structures 2D plot using CODE V are illustrated in Fig.2.1 to Fig.2.3 and their specifications are shown from Tab.2.1. to Tab.2.3. The object distance is considered infinite for each of the three systems. The red, green, blue (and also brown for Fig.2.3) lines in Fig.2.1 to Fig.2.3 indicate light beams coming from point light sources on the object with increased field angles. For example, the red lines indicate light beams coming from a point light source on the optical axis (field angle is 0 degree). In Tab.2.1 to Tab.2.3, we observe 3 parameters: 1) the number of optical elements, 2) overall thickness from center of the first lens front surface to the image plane and 3) the maximum field angle.

Compound lens system 1: USA patent 2559875 HERZBERGE

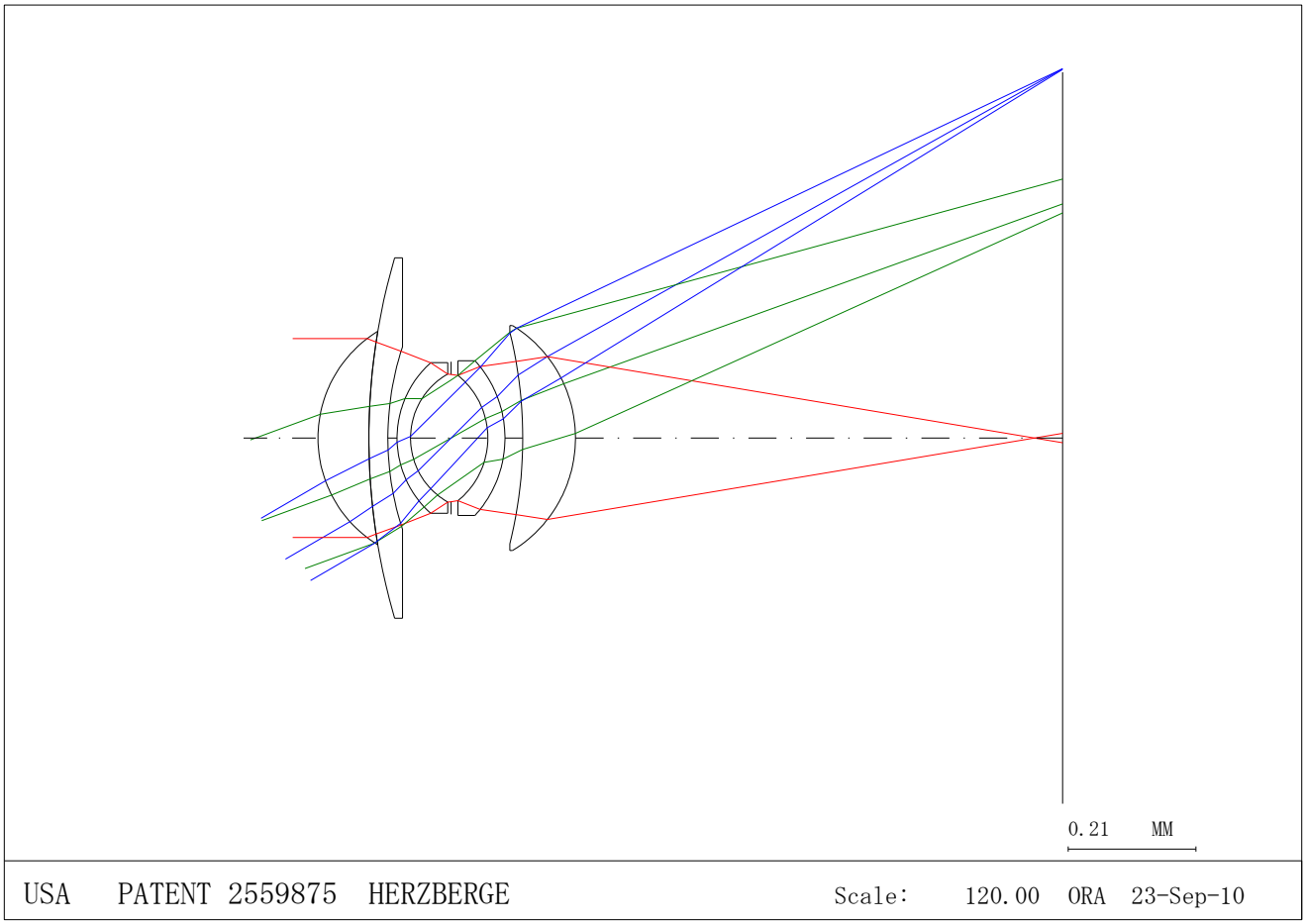

Fig.2.1 Structure of compound lens system (USA patent 2559875 HERZBERGE)

Tab.2.1 Specifications of compound lens system(USA patent 2559875 HERZBERGE)

No.of lens elements	5
Overall thickness (mm) (from center of the first lens front surface to image plane)	117
Maximum field angle (degree)	60

Compound lens system 2: USA Patent 2518719 M.REISS

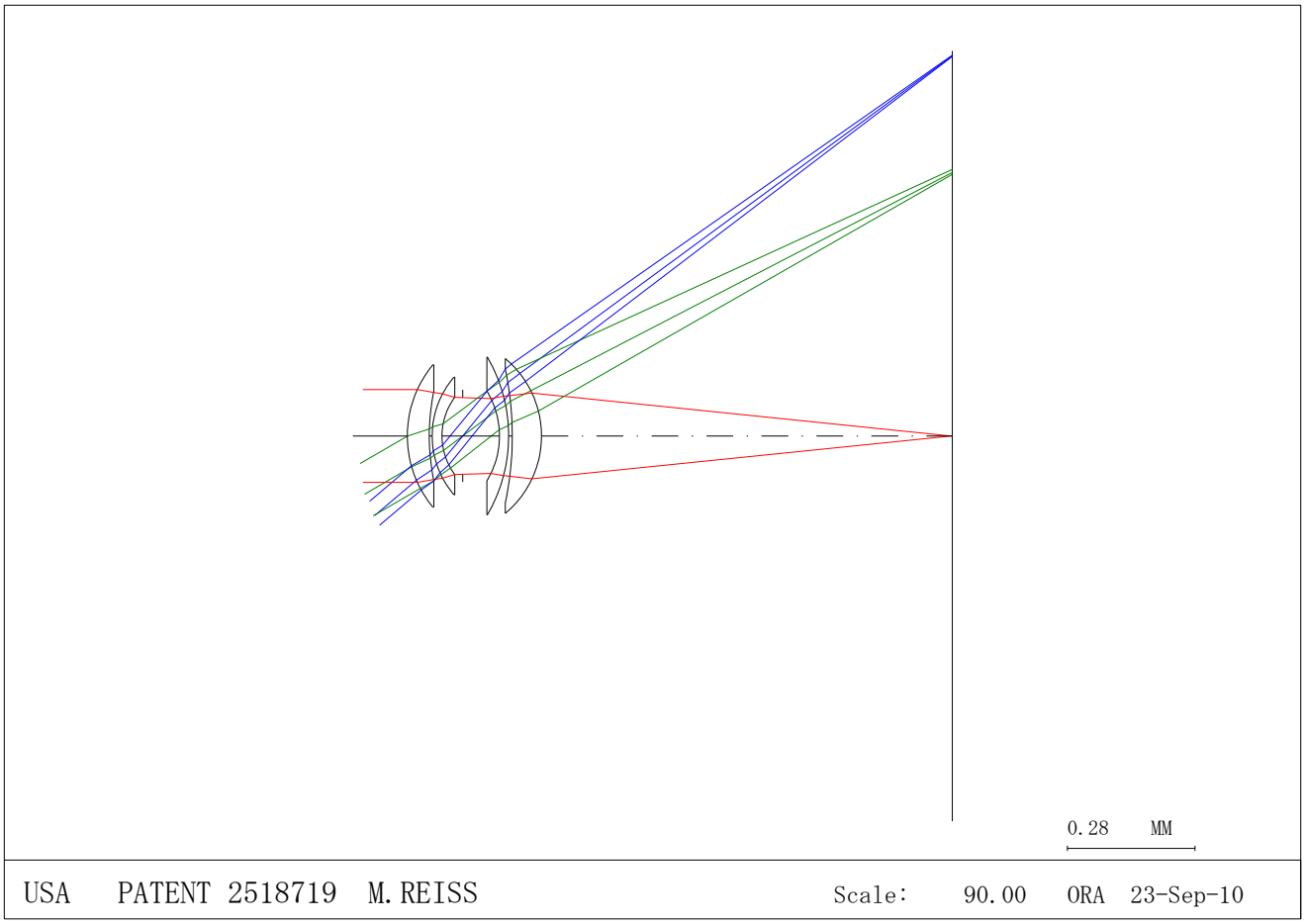

Fig.2.2 Structure of compound lens system (USA patent 2518719 M.REISS)

Tab.2.2 Specifications of compound lens system (USA patent 2518719 M.REISS)

No.of lens elements	4
Overall thickness (mm) (from center of the first lens front surface to image plane)	119
Maximum field angle (degree)	80

Compound lens system 3: USA Patent 4892398 90690 KUDO

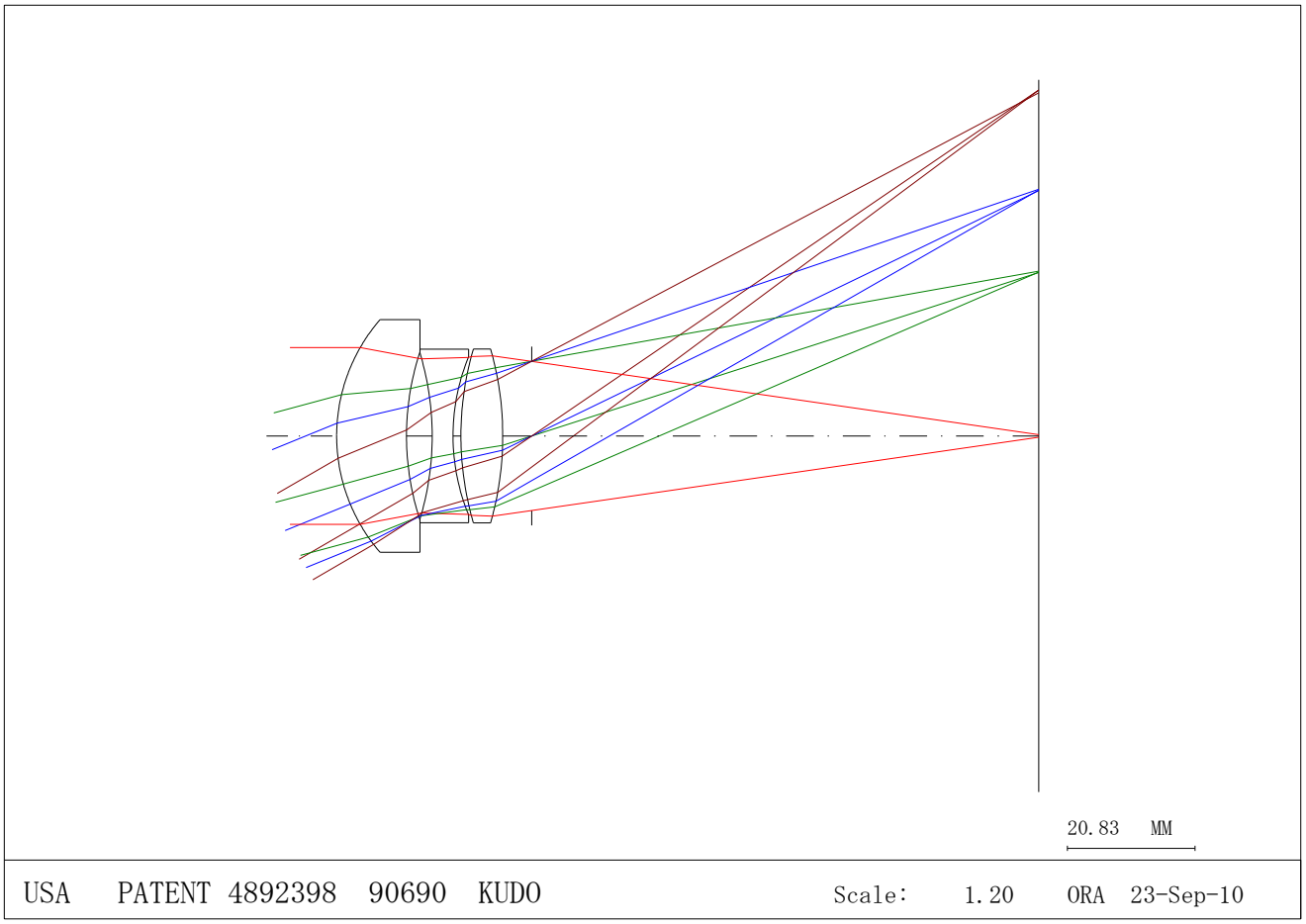

Fig.2.3 Structure of compound lens system (USA patent 4892398 90690 KUDO)

Tab.2.3 Specifications of compound lens system (USA patent 4892398 90690 KUDO)

No.of lens elements	3
Overall thickness (mm) (from center of the first lens front surface to image plane)	115
Maximum field angle (degree)	60

Then, we give some single lens structures that are double-convex or plano-convex in Fig.2.4 to 2.6, in order to compare with the compound lens system structures. The selection criterion for single lens is: low central thickness (CT), low effective focal length (EFL) and should be available on the newest commercial lens catalogue. The purpose of the single lens system design is to realize competitively low overall thickness and high field angle. The object distance is also considered infinite. In Tab.2.4 to Tab.2.6, we list 9 parameters: 1) overall thickness from center of the single lens front surface to the image plane; 2) the maximum field angle; 3) glass material with its refractive index in terms of 587.6nm light beams (The reason to show the glass material is that it greatly affects the EFL of single lens, hence the overall thickness of the imaging system.);4) Effective focal length or EFL; 5) Back focal length or BFL; 6) Lens diameter;7) Central Thickness (CT); 8) Entrance pupil diameter and 9) F No. .

Single lens system 1:

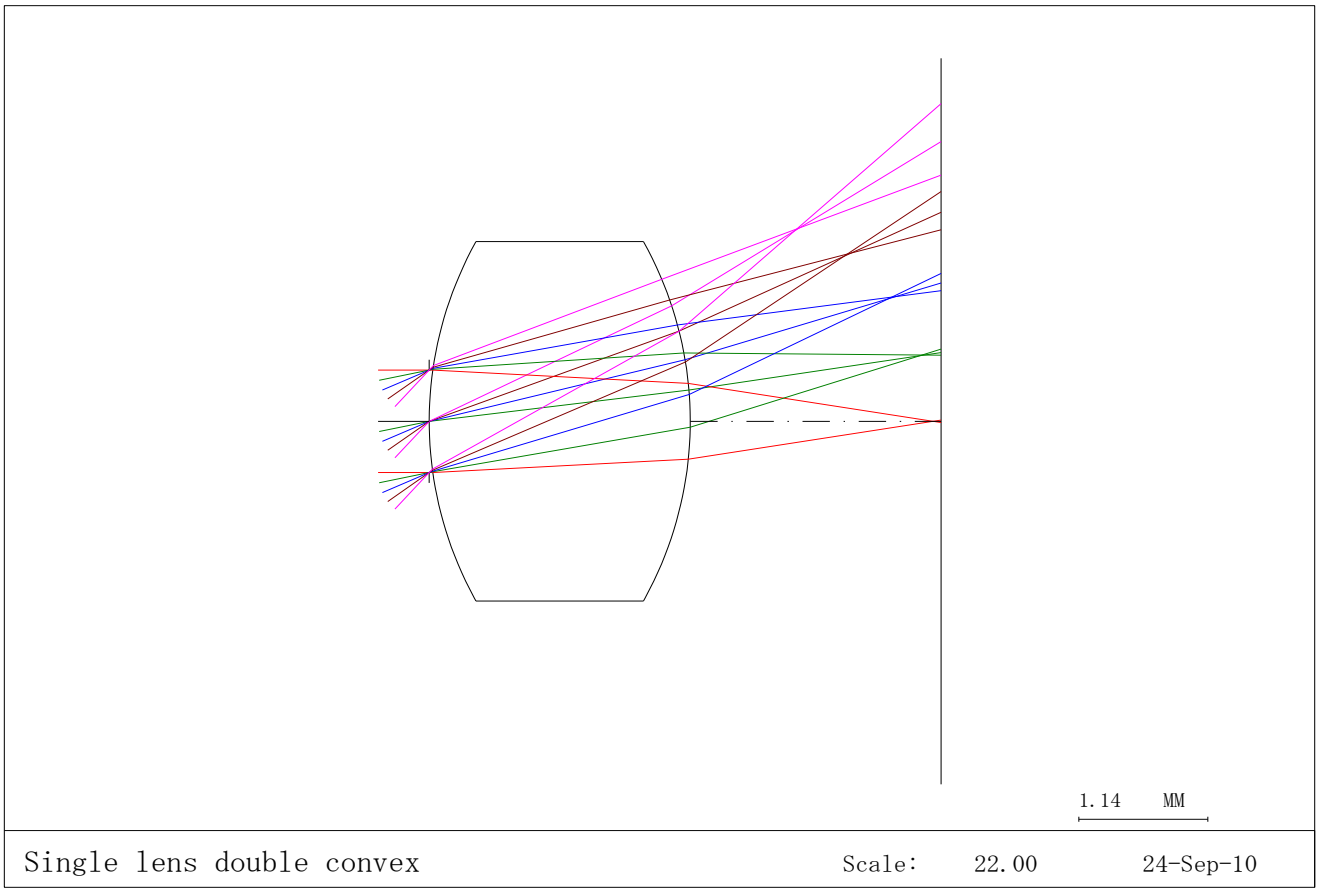

Fig.2.4 Structure of the single lens system with double convex surfaces

Tab.2.4 Specifications of the single lens system

Overall thickness (mm) (from center of the single lens front surface to image plane)	4.5
Maximum field angle (degree)	96
Glass material (Refractive index)	SF5(1.673)
Effective focal length or EFL(mm)	3.00
Back focal length or BFL(mm)	2.21
Lens diameter(mm)	3.0
Central Thickness (CT)	2.3
Entrance pupil diameter (mm)	0.94
F No.	3.2

Single lens system 2:

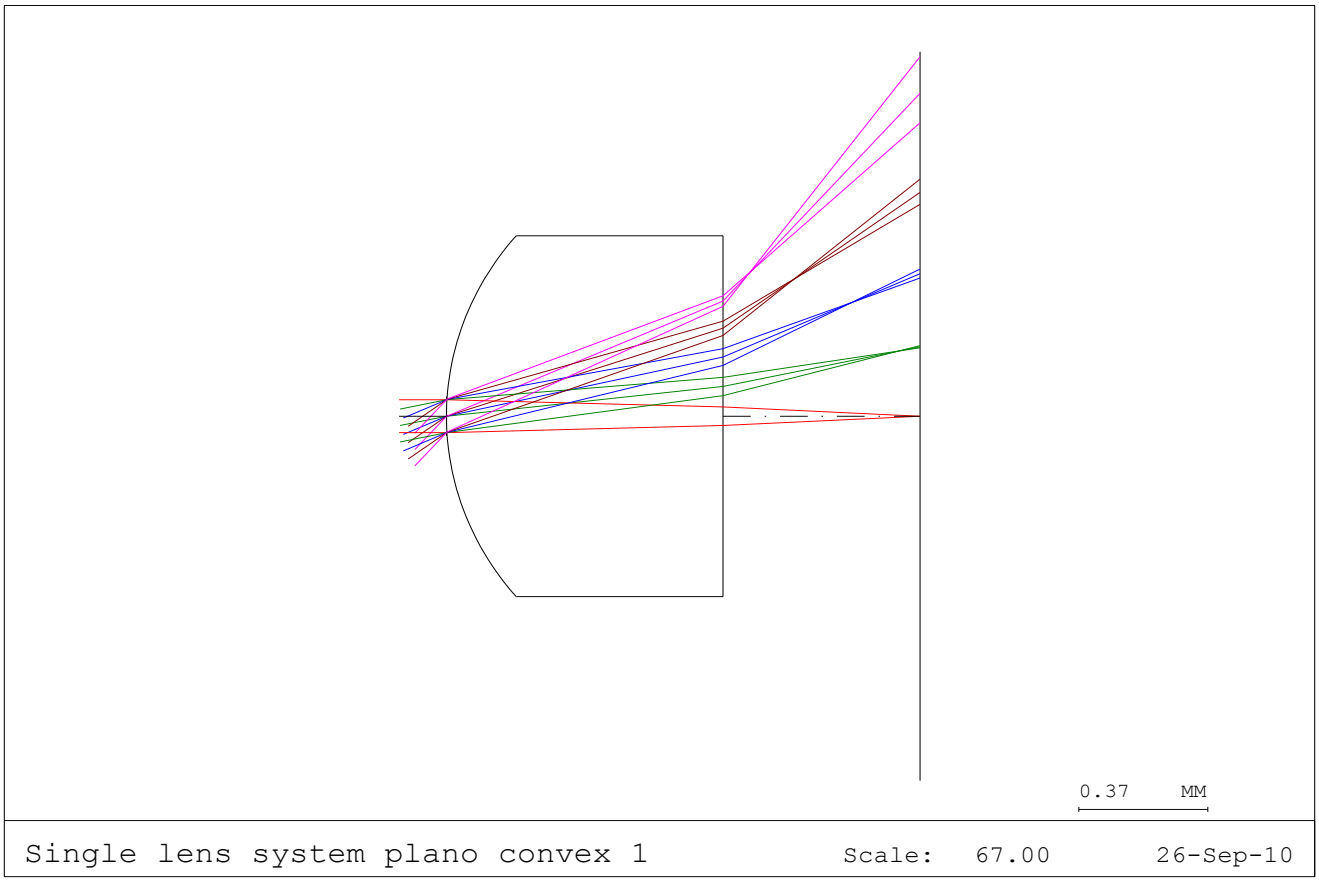

Fig.2.5 Structure of the single lens system with plano convex surfaces

Tab.2.5 Specifications of the single lens system

Overall thickness (mm) (from center of the single lens front surface to image plane)	1.4
Maximum field angle (degree)	96
Glass material(Refractive index)	LaSF9(1.850)
Effective focal length or EFL(mm)	1.0
Back focal length or BFL (mm)	0.57
Lens diameter(mm)	1.5
Central Thickness (CT)	0.8
Entrance pupil diameter (mm)	0.1
F No.	10.0

Single lens system 3:

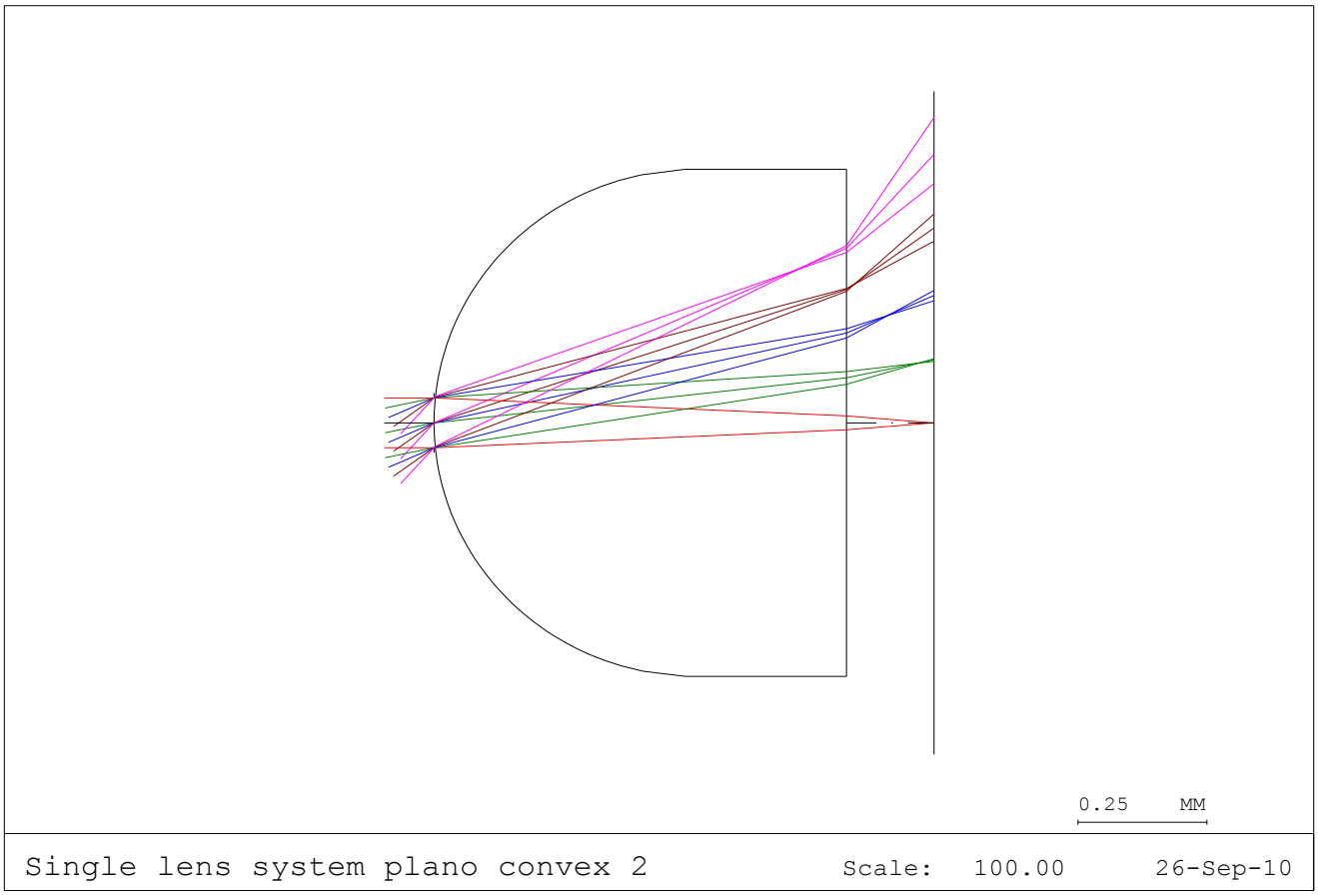

Fig.2.6 Structure of the single lens system with plano convex surfaces

Tab.2.6 Specifications of the single lens system

Overall thickness (mm) (from center of the single lens front surface to image plane)	1.0
Maximum field angle (degree)	96
Glass material(Refractive index)	LaSF9(1.850)
Effective focal length or EFL(mm)	0.6
Back focal length or BFL(mm)	0.17
Lens diameter(mm)	1.0
Central Thickness (CT)	0.8
Entrance pupil (mm)	0.1
F No.	6.0

It is evident by observing Fig.2.1 to Fig.2.3 and Tab.2.1 to Tab.2.3 that the patent lenses all showed satisfactory aberration correction capability by using compound lens, which can be observed from the foci of the low and high field angle light beams on the image plane (They are not positioned in front of or in the back of the image plane). The maximum number of optical elements is 5 and the minimum is 3. Additionally, they all showed high field angle capability: the largest reaches 80° for the USA patent lens 2518719 M.REISS shown in Fig.2.2 and the smallest value 60° are obtained by US patent lens shown in Fig.2.1 and Fig.2.3. However, the overall thickness from center of the first lens front surface to image plane is extremely long: the maximum distance reaches 119mm for the USA patent lens 2518719 M.REISS. In comparison to these compound lens systems, our newly proposed single lens systems showed competitive overall thickness and maximum field angle. In Fig.2.4, the overall thickness of the double convex system is 4.5mm, which is achieved by using glass

material with relatively high refractive index: SF5 and low CT (2.3mm). The EFL and BFL for this system are 3.00mm and 2.21mm, respectively. According to Fig.2.5 and Fig.2.6, the overall thickness could be further shortened by using plano-convex surfaces and higher refractive index glass LaSF9. The overall thickness is obtained by adding BFL and CT of the lens. Ultra-thin thickness of the lens system is achieved for plano-convex lens 1 (1.4mm) and plano-convex lens 2(1.0mm). The high field angle range (0~96 degree) is still obtainable by sacrificing the diameter of entrance pupil. The central area around the optical axis showed no spherical aberrations because the entrance pupil is relatively very small compared to lens diameter. Therefore sharp image could be formed around image center. However, the other aberrations such as distortion, field curvature and lateral chromatic aberration (LCA) are very strong compared to compound lens aberrations and become extremely strong when the field angle reaches highest value. For example, the field curvature can be observed by the foci of low and high field angle light beams: the light beams coming from the off axis point source failed to focus on the image plane but in front of it and the higher the field angle the longer the distance between foci and image plane. This phenomenon results in an image with increased blur pattern from image center. In the next section, comparison of aberrations between the compound lens systems and the single lens systems will be illustrated quantitatively in aberration curves and visually in PSF distribution image and 2D image simulation.

2.3 Comparison of optical aberrations between conventional and newly proposed optical imaging system

Firstly, we give the following curves showing distortion and lateral chromatic aberration (LCA) for the three compound lens systems and the three single lens systems. Distortion will lead to geometrical deformation from the normal image and LCA results in displacement between different colors on the image plane. These two aberrations are not related to image blur. Other optical aberrations: spherical aberration, coma, astigmatism, field curvature and axial chromatic aberration (ACA) all result in blur on the image plane, so that they can be represented by PSF distribution images shown in Fig.2.10. The values are calculated by real ray tracing, so that it is neither first order values nor third order Seidel aberration values. In order to unify the maximum field angle for comparison, we only measure distortion and LCA that belongs to half field angle lower than 30 degree for all the six imaging systems.

The distortion values are measured in terms of the reference light beams whose wavelength is 587.6nm. In Fig.2.7, the horizontal axis shows semi field angle (or half field angle) and the vertical axis shows the distortion in percentage. The distortion is calculated by obtaining the difference between real chief ray height and paraxial chief ray height on the image plane and then divided by the paraxial chief ray height. Suppose the paraxial chief ray height is $\overline{y'}$ and the real chief ray height is y', then we have

$$dist = \frac{y' - \overline{y'}}{\overline{y'}} \times 100\% \tag{2.1}$$

It can be observed from Fig.2.7 that distortion values of the compound lens systems are much smaller than that of the single lens systems. The maximum distortion among compound lens systems is approximately -1.9%, while the minimum distortion among single lens system already surpasses this value, reaching up to approximately -4.3%. The maximum distortion -8.2% for single lens systems is obtained by single lens 1 at field angle 30 degree. As the field angle increases, the distortion will further increase as well. We have measured that the distortion value rises up to -23.0% at the maximum semi field angle 48 degree for the double convex single lens system, which is very large for an imaging system.

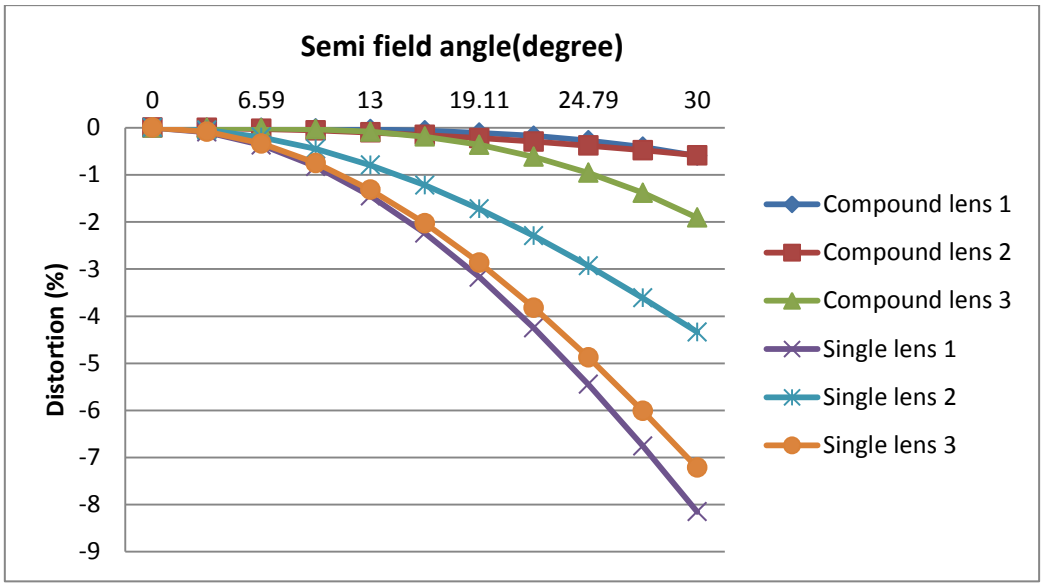

Fig.2.7 Comparison of distortion among compound lens systems and single lens systems

Similarly, the graphs showing LCA for the three compound lens systems and the three single lens systems are illustrated in Fig.2.8 and Fig.2.9. The LCA values are measured between chief rays of Fraunhofer F line (486.1nm) and C line (656.3nm) light beams, and between chief rays of F line and d line (587.6nm) light beams. Therefore, two graphs are drawn separately. The horizontal axis is the semi field angle and the vertical axis indicates LCA values in millimeters. The LCA between F line and C line light beams are larger than that between F line and d line light beams for all the six systems because the wavelength difference of the former is relatively larger than the latter. Except the compound lens 3, the other two compound lens systems all showed smaller LCA values than the single lens systems. The curves depicting compound lens 1 and compound lens 2 almost overlapped with each other, showing LCA values very close to zero. The maximum LCA: -0.2μm and -0.1μm is obtained at semi field angle 30 degree for compound lens 2. As an exception, the LCA values of compound lens 3 show very unstable variation: being positive when the field angle is lower than 22.5 degree and negative when it is above 22.5 degree, and the maximum LCA even exceeded that of single lens 1, which is possible for certain kind of lens system. Besides compound lens 3, the LCA of single lens 1 surpasses all the others, showing maximum LCA -0.017mm and -0.012mm at semi field angle 30 degree. The LCA of single lens 2 and 3 overlapped with each other, showing near equivalent values.

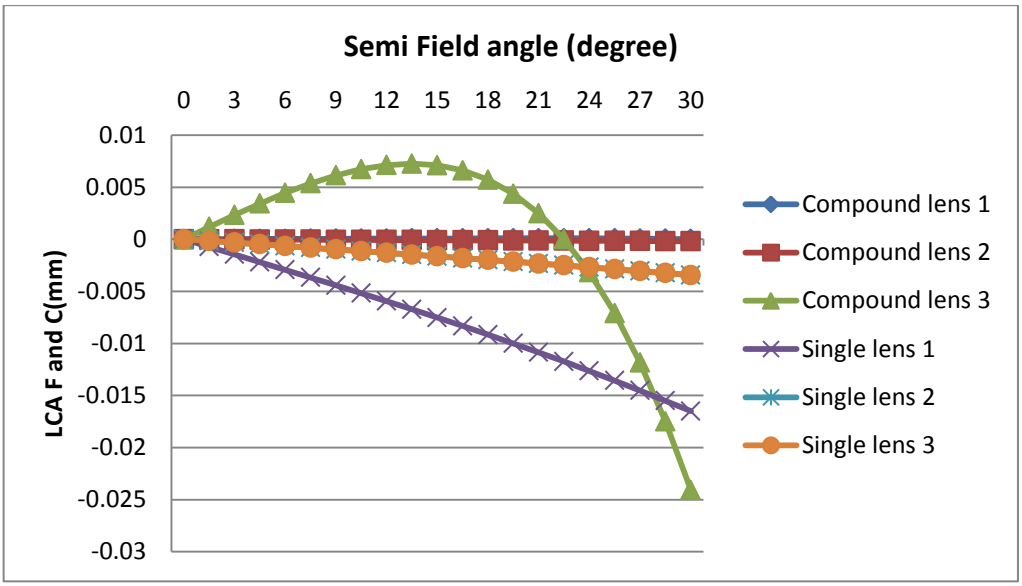

Fig.2.8 LCA comparison between F line and C line light beams among compound lens systems and single lens systems

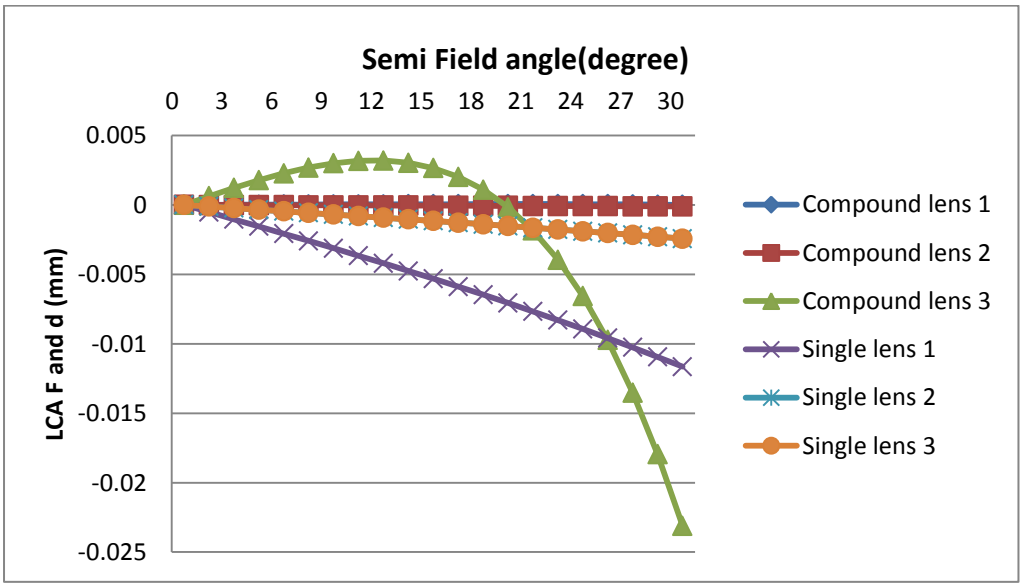

Fig.2.9 LCA comparison between F line and d line light beams among compound lens systems and single lens systems

Finally, the Point Spread Function (PSF) distribution images that are result of all blur-forming aberrations (coma, astigmatism, field curvature and the axial chromatic aberration) are shown in Fig.2.10. In addition, we give the 2D image simulation results in Fig.2.11, in which a photograph of a visually normal two dimensional image is “taken” by these lens systems. The resulting image includes all optical aberrations mentioned above. Two test images are simulated: one with rectangular frames in order to show distortion and LCA, the other includes small English characters in order to show radially variant blurring effect.

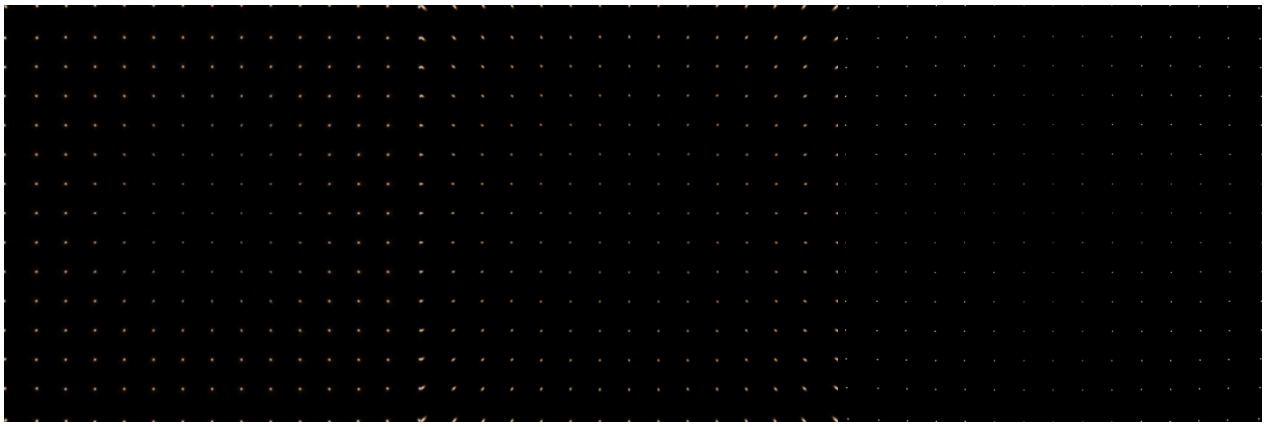

(a) Compound lens 1 (b) Compound lens 2 (c) Compound lens 3

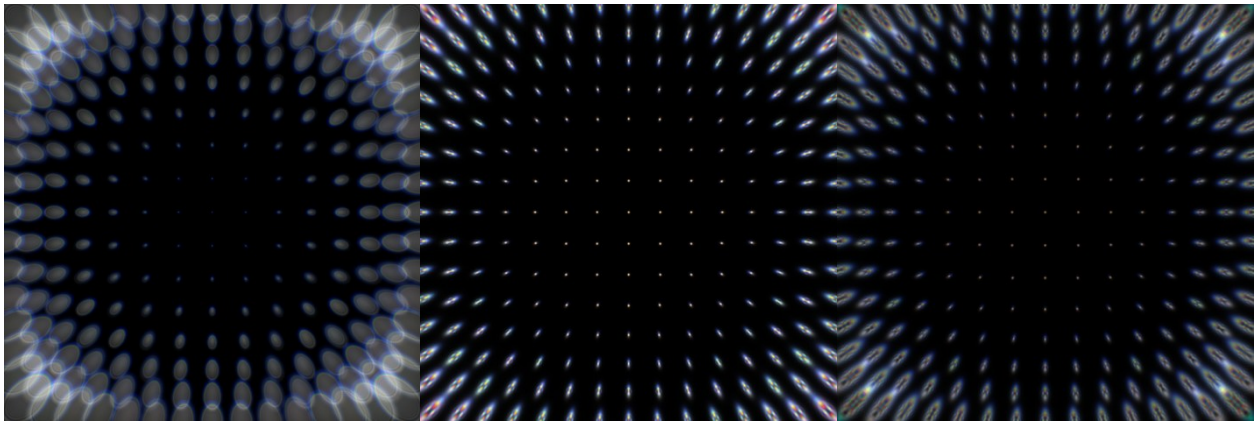

(d) Single lens 1 (e) Single lens 2 (f) Single lens 3

Fig. 2.10 PSF distribution of the compound lens systems and the single lens systems

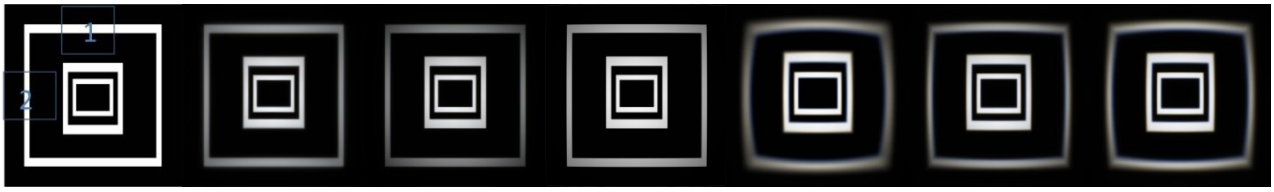

(a) (b) (c) (d) (e) (f) (g)

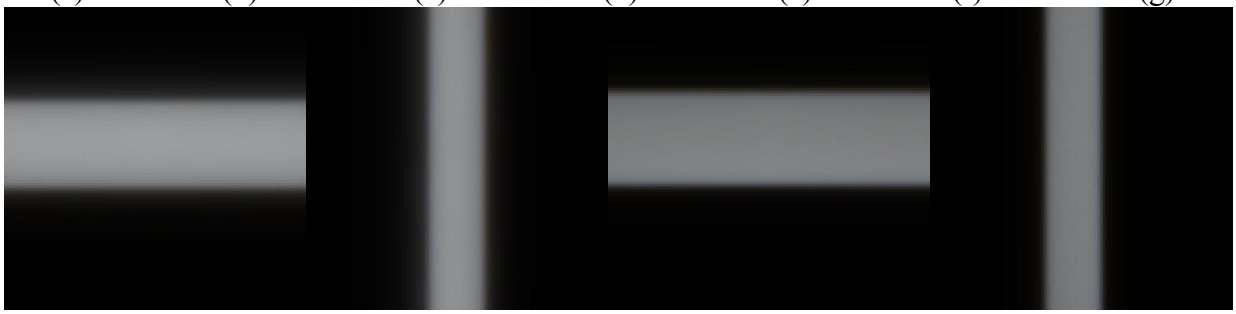

(h) (i) (j) (k)

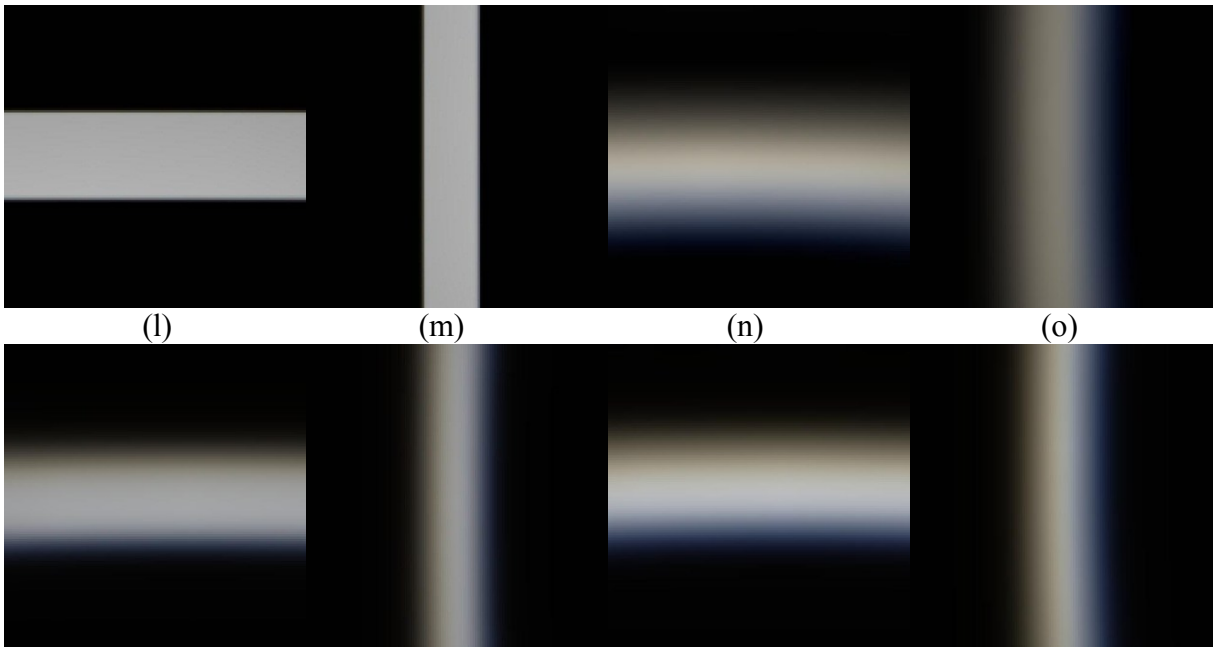

(l) (m) (n) (o)

(p) (q) (r) (s)

Fig.2.11 2D image simulation results of test image 1 for the compound lens systems and the single lens systems: (a) original image; (b) (c) (d) (e) (f) (g) image produced by compound lens system 1, 2, 3 and single lens system 1,2,3, respectively; (h) (i) zoom in of area 1 and 2 for compound lens system 1; (j) (k) zoom in of area 1 and 2 for compound lens system 2; (l) (m) zoom in of area 1 and 2 for compound lens system 3; (n) (o) zoom in of area 1 and 2 for single lens system 1; (p) (q) zoom in of area 1 and 2 for single lens system 2; (r) (s) zoom in of area 1 and 2 for single lens system 3.

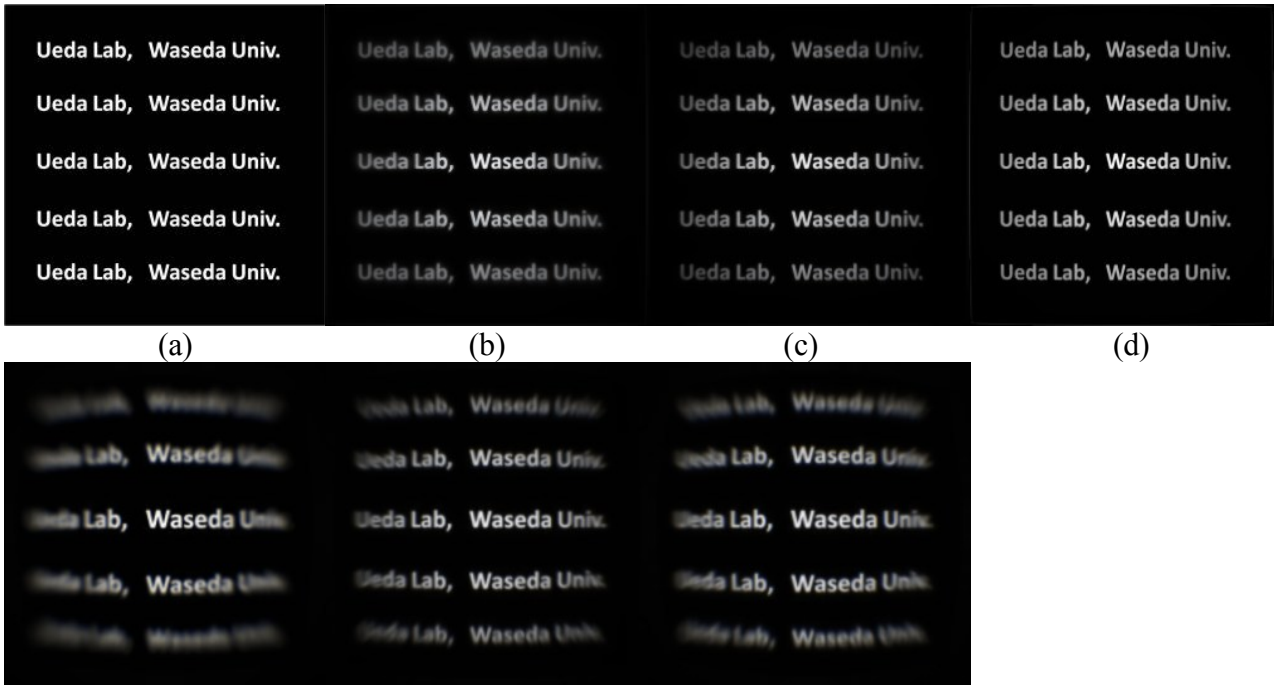

(a) (b) (c) (d)

(e) (f) (g)

Fig.2.12 2D image simulation results of test image 2 for the compound lens systems and the single lens systems: (a) original image; (b) (c) (d) (e) (f) (g) image produced by compound lens system 1,2,3 and single lens system 1,2,3, respectively.

The PSF distribution images shown in Fig.2.10 demonstrate that all compound lens systems produce sharp point images for low and high field angle regions. Nevertheless, the PSFs of single lens systems indicate radially increasing blur effect from image center to image borders, which is a result of field curvature phenomenon that is already explained in Section 2.2. The PSFs at high field angles are more intensive for the spherical double convex system shown in Fig.2.10 (d) than the two plano-convex systems shown in Fig.2.10 (e) and (f), indicating that fewer aberrations can be obtained by using plano-convex system. This can also be confirmed in the 2D image simulation results in Fig. 2.12.

2D simulation on test image 1 shown in Fig.2.11 is to visually examine distortion and LCA of the compound lens systems and single lens systems. According to Fig.2.11 (b) to (g), strong distortion can be easily observed on high field regions of single lens systems, whereas distortion of compound lens systems can barely be observed. Among the single lens systems, the strongest distortion was obtained by (e): the double convex system. This is consistent with the result of distortion curves shown in Fig.2.7. In order to show LCA, we enlarged areas where the LCA is relatively strong for the six optical systems. The areas to be enlarged are marked with number "1" and "2" in Fig.2.11 (a). The corresponding enlarged images are given from Fig.2.11 (h) to (s). As is expected, single lens systems obtained stronger LCA than compound lens systems, which can be perceived by blue color on the inner fringe of the rectangular frames. The strongest LCA among single lens systems belongs to the double convex lens, which can also be observed from LCA curves shown in Fig.2.8 and Fig.2.9.

2D simulation on test image 2 shown in Fig.2.12 is to visually examine radially variant blur effect of the single lens systems. Obviously, the resulting images of the compound lens systems showed little blur effect compared with those of the single lens systems. Among all the single lens systems, although the low field regions are visually normal, the high field regions are strongly blurred and distorted, which is understandable with the help of PSF distribution images in Fig.2.10.

2.4 The feasibility to compensate for single lens aberrations using digital image processing techniques

This section demonstrates the feasibility of correcting aberrations for single lens system using the proposed image digital processing methods rather than using the compound lens. As the detailed description of results will be given on the following chapters, we only show briefly the resulting images. The simulation of aberration correction is carried out based on the aberration values of the double convex single lens, the plano-convex systems will not be addressed here.

The resulting images of distortion correction and LCA correction for test image 1 are shown in Fig.2.13 to Fig.2.15.

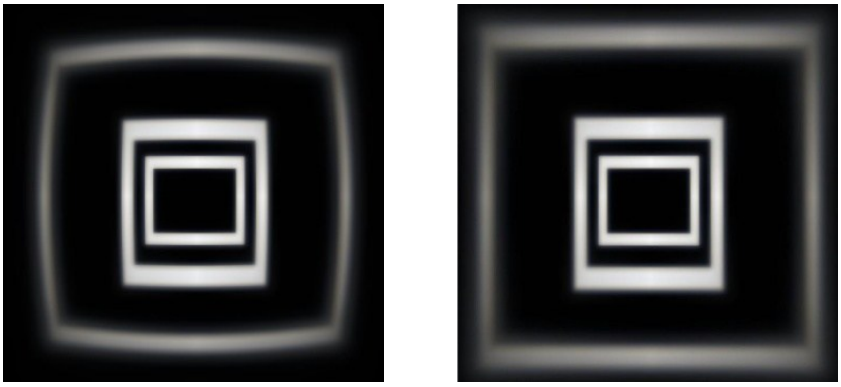

(a)distorted (b) distortion corrected

Fig.2.13 Comparison between distorted image and corrected image

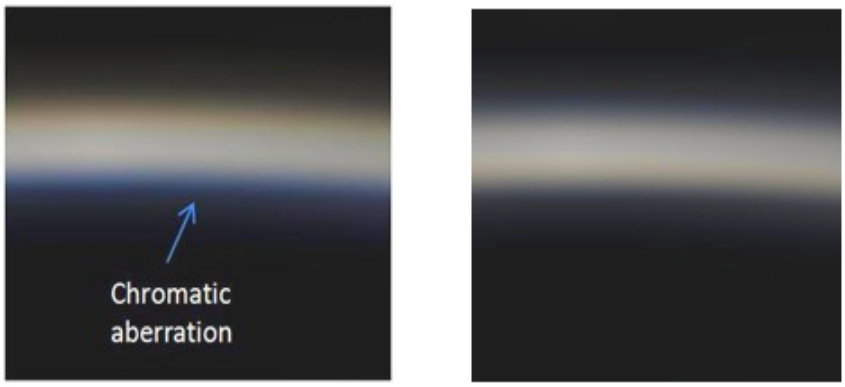

(a) before LCA correction (b) LCA corrected

Fig.2.14 Image comparison before and after LCA correction for region 1

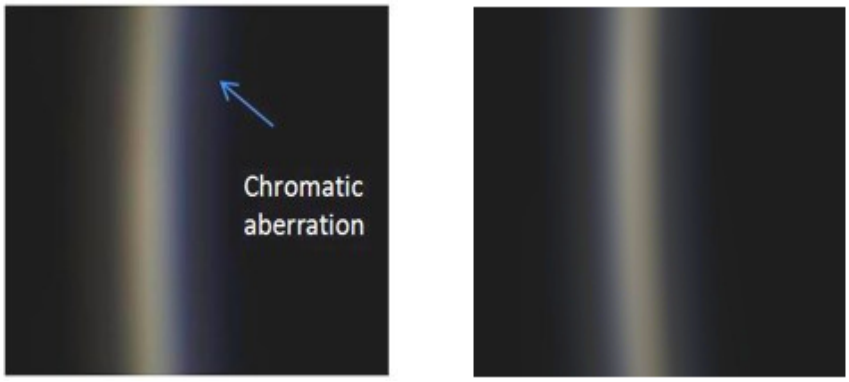

(c) before LCA correction (d) LCA corrected

Fig.2.15 Image comparison before and after LCA correction for region 2

As to the restoration of radially blurred image, we set the maximum field angle to 21 degree because of the software limitation, which says the PSF will become inaccurate when the field angle is larger than 21 degree. This will be further discussed in Chapter 5.

Image restorations of two monochromatic images are shown in Fig.2.16.

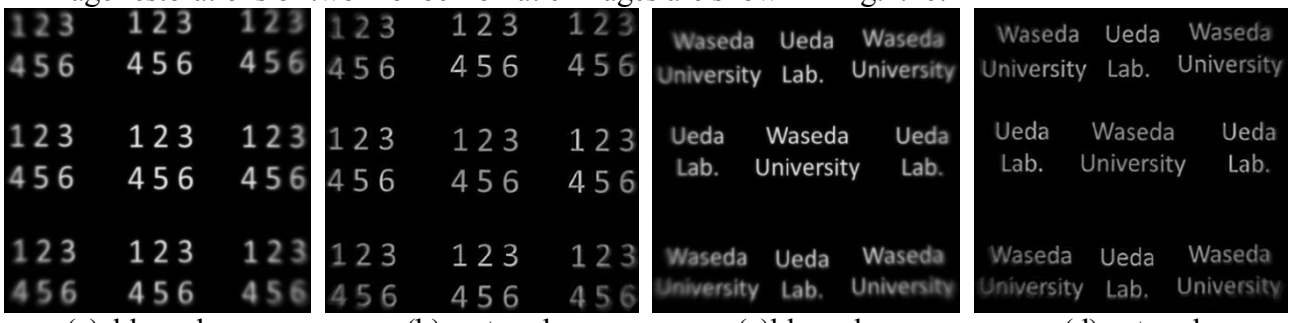

(a) blurred (b) restored (c)blurred (d)restored

Fig.2.16 Radially blurred image restoration for two monochromatic images

2.5 Conclusion

In conclusion, this chapter compared the structure of three compound lens systems and three single lens systems and showed that the overall thickness from center of the first lens front surface to image plane can be reduced to approximately 1.0mm by using plano-convex single lens whereas this distance of the current cell phone cameras are 7~10mm. The maximum field angle (MFA) can be increased to 96 degree if the entrance pupil diameter is relatively small compared to lens diameter. In spite of a special case such as compound lens system 3, distortion and LCA curves indicated that the distortion and LCA values of single lens systems all exceeded that of the compound lens systems. PSF

distribution images and 2D image simulation results showed more intensive radial blur effect at high field angle regions for single lens systems than compound lens systems. The resulting images for distortion, LCA correction and image restoration demonstrated that optical aberrations produced by single lens systems can be minimized by digital image processing techniques, even if optical means is not used.

Finally, a table showing merit and demerit of compound lens systems and single lens systems is as follows:

Tab.2.7 Merit and demerit of two lens systems

	Conventional compound lens system	Proposed single lens system
Merit	Few optical aberrations by optical correction	Thinner and slimmer
Demerit	Overall thickness is very long	Significant optical aberrations (But can be minimized by digital image processing techniques)

Chapter 3 Correction of distortion

Chapter 3 Correction of distortion

3.1 Introduction

This chapter introduces distortion correction methods for single lens systems. Before introducing our methods, it is necessary to briefly present the research background of this field of study. In the literatures of geometrical distortion correction, researchers have proposed many algorithms aiming at compensating for lens distortion digitally. For example, polynomial warping correction method is known as the most widely used distortion correction method, in which a polynomial equation of degree N is determined by a set of control points in the first step. Then the polynomial equation coefficients were calculated from the control points by least-squares minimization. Finally, use the polynomial equation to transfer the points from the distorted image to a corrected image [3-1]. Another simple mathematical model for lens distortion correction was introduced by H. Ojanen [3-2], which is applicable to three types of lens distortion: barrel distortion, pincushion distortion and the combination of the two basic types. The correction was done by building up a composite mapping function between the object plane and the film plane, taking consideration not only the undistortion function but also other functions that are needed to compensate for inaccuracies in the test setup and using least-squares method to choose the undistortion parameters. On the other hand, some algorithms are dedicated to applying to specific imaging systems. For instance, field mapping and point spread function (PSF) mapping were proposed and compared to correct intensity distortion and geometrical distortion in Echo-planar imaging (EPI) system [3-3] and a geometrical distortion correction method based on image normalization was introduced by M.Alghoniemy, which can be applied to image watermarking systems that are vulnerable to geometric attacks [3-4]. Methodologies for barrel distortion correction in electronic endoscope images suggest that the non-linear inhomogeneous distorted images due to wide-angle configuration of the camera lens can be corrected by building up a correction model and estimating the correction parameters [3-5],[3-6].

Additionally, as an indispensable process after our integer mapping method that will be introduced in the following sections, interpolation plays a crucial role in determination of the values of pixel vacancies and restoring the pixel continuity of the distortion-corrected image. Therefore, a brief review on the development of interpolation methods is very helpful to understand our texture dependent interpolation method proposed in [3-17]. Many interpolation techniques have been proposed by predecessors in this field of research. The well-known and most commonly used should be the polynomial interpolation, in which case the basic idea is to represent an unknown pixel value by a polynomial, solving polynomial equation set to obtain the coefficients of polynomial. Then compute the unknown pixel value by substituting the vertical and horizontal coordinates into the polynomial equation. The number of coefficients should be equal to that of the polynomial equations, in other words, to the number of neighboring pixels that are used to calculate coefficients. Application of polynomial interpolation other than image processing was also introduced to estimate heights of a continuous surface for the DEM (Digital Elevation Model) [3-7]. In the literature of linear and space-invariant interpolation, the commonest interpolation methods are nearest neighbor interpolation, bilinear interpolation and bicubic interpolation, whose mathematical expressions can be derived by adding or reducing the number of coefficients of the polynomial equation. In the Video and Image Processing Blockset of Matlab, nearest neighbor interpolation is implemented by obtaining nearby translated pixel values, bilinear interpolation is implemented by obtaining weighted average of the two translated pixel values on either side of the input pixel. Bicubic interpolation is implemented similarly by obtaining weighted average of the four translated pixel values on either side of the input pixel. Another algorithm depicted that the bilinear interpolation creates new pixels based on color averages from both the horizontal and vertical neighbors of the area to be resized, and the bicubic interpolation creates new pixels based upon weighted average from horizontal, vertical and diagonal directions. Much smoother images can be obtained by Cubic Splines or B-splines, which was first

introduced by H.C.Andrews and C.L.Patterson in 1976[3-8] and a detailed mathematical analysis was proposed by H.S.Hou and H.C. Andrews in 1978[3-9]. There are other superior interpolation schemes such as isophote-oriented methods, which usually employ a PDE (Partial Differential Equation) iterative interpolation, mainly proposed to avoid zigzagging artifacts around edge introduced by traditional linear interpolation methods[3-10] to [3-13]. Comparison among different interpolation methods [3-14] and [3-15] were documented to provide a comprehensive reference by which we are able to pick up an optimal method for a specific application.

In this chapter, the original method "Field angle dependent distortion coefficient" will be described firstly. This method was proposed because the distortion component of the traditional third order Seidel aberration is not accurate to represent real distortion values in case of high field angles. For example, the double convex single lens system depicted in Chapter 2 results in 0.3710mm deviation from the real distortion value at half field angle 48 degree if third order distortion component is utilized. Therefore, improvement should be made to the third order distortion component in order to correct distortion precisely. Secondly, forward mapping and backward mapping methods will be introduced and compared. The former obtains the distortion-corrected image from the distorted image while the latter maps image pixels from a virtual distortion-free, ideal image to a distorted image. The latter is superior to the former because of two reasons: 1) no pixel vacancies will be created after distortion, thus the additional interpolation process is unnecessary; 2) higher precision of pixel values is obtainable because bilinear interpolation is employed rather than nearest neighbor interpolation used in forward mapping method. Finally, simulation results of the proposed techniques of distortion correction will be discussed.

3.2 Methods

3.2.1 Distortion coefficient depending on field angles

The algorithm to correct distortion is based on the famous third order Seidel aberration theory but with some improvement because the maximum field angle in our lens design is very high. The Seidel third order aberration approximates the Snell's Law $n\sin\theta = n'\sin\theta'$ to $n(\theta - \theta^3/3!) = n'(\theta' - \theta'^3/3!)$, therefore higher precision can be obtained when we calculate optical aberrations than the paraxial approximation $n\theta = n'\theta'$.

The distortion component of the third order Seidel aberration equation can be expressed as follows [3-16]

$$\Delta y'_{dist} = S\overline{y'}^3 \tag{3.1}$$

The real distortion occurring on the image plane can be expressed as

$$\Delta y'_{dist\_real} = y' - \overline{y'} \tag{3.2}$$

The third order distortion approximately equals to the real distortion when the field angle is not too high, which can be written as follows

$$S\overline{y'}^3 = y' - \overline{y'} \tag{3.3}$$

In equations (3.1) to (3.3), $\Delta y'_{dist}$ and $\Delta y'_{dist\_real}$ mean third order distortion and real distortion, respectively. $\overline{y'}$means the ideal image height and $y'$is real image height, which is distorted from the ideal image height $\bar{y}'$. S indicates distortion coefficient. When the field angle is very high, equation (3.3) has to be modified, otherwise the accuracy of the third order distortion will decline dramatically and no longer equals to right side of the equation. To precisely represent the distortion value at every field angle, we regard distortion coefficient S as a continuously changing value rather than a constant. In other words, S should be considered as a function of $\overline{y'}$, or $S = f(\overline{y'})$. We found that the relation between S and $\bar{y}'$ can be better represented by polynomial approximation than other curve approximation. Therefore, we calculated S by rewriting equation (3.3) for different field angles as

different sample points using the real distortion $\Delta y'_{dist\_real}$ and ideal image height $\overline{y'}$.

$$S = \frac{\Delta y'_{dist\_real}}{\overline{y'}^3} \tag{3.4}$$

In this equation, the values of real distortion $\Delta y'_{dist\_real}$ can be directly read out by optical design software CODE V when the single lens system is built up. And the ideal image height $\overline{y'}$ can be calculated by equation (3.5).

$$\overline{y'} = f' \tan\omega \tag{3.5}$$

This equation is known as the paraxial equation that calculates the image height when the object distance is infinite. ω is the half field angle, f' indicates Effective Focal Length(EFL) and $\overline{y'}$ means paraxial image height (also ideal image height).

Take the double convex single lens for example, when the half field angle reaches maximum (48 degree), $\overline{y'}$ is 3.332mm. The value of real distortion $\Delta y'_{dist\_real}$ is -0.7682mm. Therefore S is -0.0208($1/\mathrm{mm}^2$). Then we made a third order polynomial approximation between S and $\overline{y'}$. By doing this we can calculate S for all field angles, not only the sample points. The sample data, relationship curve and the corresponding third order polynomial equation will be given in Section 3.3.

3.2.2 Comparison between forward and backward mapping methods.

1) Forward mapping method:

The forward mapping method, as its name suggests, maps image pixels from a distorted image to an ideal distortion-free image. It can be further divided into integer pixel mapping and decimal pixel mapping methods. Fig.3.1 illustrates the schema of the two forward mapping methods:

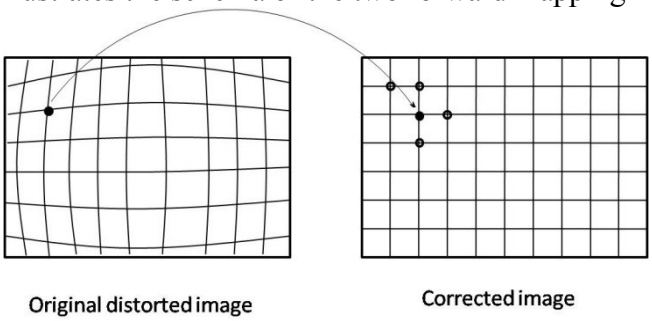

(a) Integer pixel mapping

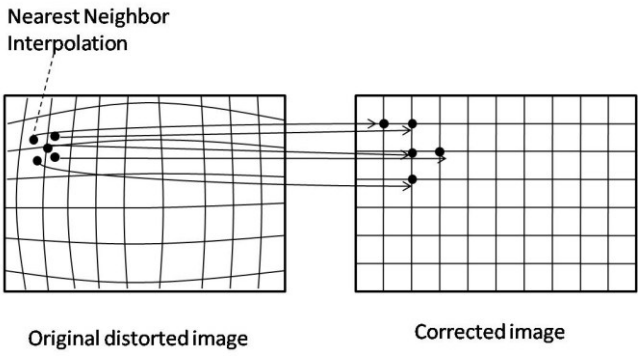

(b) Decimal pixel mapping

Fig.3.1 Schema of the forward mapping method

The solid dot in Fig.3.1 means pixel of the original distorted image and the mapped pixel in the corrected image. The hollow dot means pixel vacancy that is created by using forward mapping method. Fig.3.1(a) shows that an integer pixel in the original distorted image is mapped to the corresponding position in a corrected image. However, pixel vacancies appear around the mapped

pixel. Therefore data interpolation has to be employed to fill up those vacancies. We proposed a texture dependent interpolation method [3-17] that determines the value of a pixel vacancy by texture around the pixel. This interpolation can be classified into 16 cases and the pixel value is obtained by nearest neighbor, linear interpolation or bilinear interpolation according to specific cases. The decimal pixel mapping method shown in Fig.3.1 (b), however, does not create vacancies if sufficient decimal pixels are defined around the integer pixel in the original distorted image. In other words, the hollow dots shown in Fig.3.1 (a) have their corresponding positions that are provided by decimal pixels. In the following paragraphs, we will introduce the two methods in details.

The equation that determines the pixel position on a distortion-free ideal image for both integer mapping and decimal mapping can be expressed as follows:

$$\overline{y'} = \frac{y'}{1 + S' y'^3} \tag{3.6}$$

This equation is a modified version of equation (3.3). The reason to modify (3.3) is that usually we only have a geometrically distorted image in hand and hope to know the value of ideal image height $\overline{y'}$ from the distorted image height y', that is, $\overline{y'} = f(y')$. However, according to equation (3.3) we know that obtaining $\overline{y'}$ from y' is not an easy task as we have to deal with the cubic root. Therefore, we rewrote (3.3) to $S' y'^3 \overline{y'} = y' - \overline{y'}$ and further to $S' y'^3 = (y' - \overline{y'})/\overline{y'}$ to avoid dealing with cubic root so that simplified the forward mapping equation to $\overline{y'} = y'/(1 + S' y'^3)$. Here $S' y'^3 = (y' - \overline{y'})/\overline{y'}$ also represents third order distortion value in percentage. Note that S' does not mean the third order distortion coefficient of Seidel aberration anymore. In our previous study [3-17] to [3-20], we did not consider the lens design process, only showed how the geometrically distorted image can be corrected by correction algorithm, where S' in the modified equation can be easily determined by visually measuring the distorted image. If we take account of the lens design process, the equation $S' y'^3 = (y' - \overline{y'})/\overline{y'}$ is not useful anymore because the third order distortion coefficient S has to be calculated from lens design data.

The interpolation after the integer pixel mapping process is called the texture dependent interpolation method. This interpolation is actually a case dependent (or case analysis) method that can be categorized into 16 cases based on the following fundamental methods:

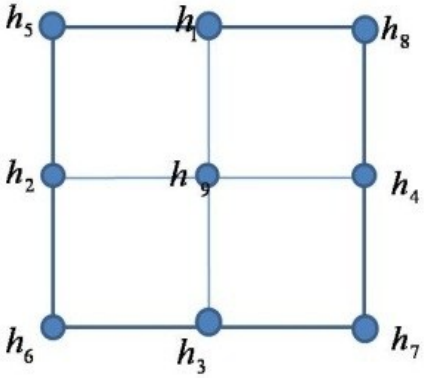

Fig.3.2 Interpolation grid: the central pixel h_9 is determined by the nearest pixels: h_1 to h_4. All pixels in this grid are equally spaced.

(1) Nearest Neighbor

$$h_9 = h_1 \text{ or } h_9 = h_2 \text{ or } h_9 = h_3 \text{ or } h_9 = h_4 \tag{3.7}$$

(2) Linear interpolation

$$h_9 = \frac{h_1 + h_3}{2} \text{ or } h_9 = \frac{h_2 + h_4}{2} \text{ or } h_9 = \frac{h_1 + h_2}{2} \text{ or}$$

$$h_9 = \frac{h_2 + h_3}{2} \quad \text{or} \quad h_9 = \frac{h_3 + h_4}{2} \quad \text{or} \quad h_9 = \frac{h_4 + h_1}{2} \tag{3.8}$$

(3) Bilinear Interpolation

$$h_9 = \frac{h_1 + h_2 + h_3 + h_4}{4} \tag{3.9}$$

The 16 cases of texture dependent interpolation can be further divided into 5 groups:

① Four pixels located on the vertical and horizontal neighbors are all non-zeros, in which case we carry out bilinear interpolation using values of the four pixels (one case in all). For example, $h_1 h_2 h_3$ and h_4 in Fig.3.2 are all non-zero pixels, therefore we obtain the value of h_9 by (3.9).

②Three pixels located on the vertical and horizontal neighbors are non-zeros and one zero pixel, in which case we carry out linear interpolation using values of the two non-zero pixels that align with the central pixel (4 cases in all). For example, only h_1 in Fig.3.2 is zero pixel, therefore we obtain the value of $h_9$by $h_9 = (h_2 + h_4)/2$ of (3.8).

③ Two pixels located on the vertical and horizontal neighbors are non-zeros and two zero pixels. Whether the two non-zero pixels are opposite to each other, or they are next to each other, we carry out linear interpolation using their values (6 cases in all). For example, h_1 and h_3 in Fig.3.2 are non-zero pixels, then h_9 can be obtained by $h_9 = (h_1 + h_3)/2$ of (3.8) or $h_1$and h_2 are non-zero pixels, then $h_9$can be obtained by $h_9 = (h_1 + h_2)/2$ of (3.8).

④One pixel located on the vertical or horizontal neighbors is non-zero and three zero pixels, in which case we carry out nearest neighbor using value of the non-zero pixel (4 cases in all). For example, h_1 in Fig.3.2 is the non-zero pixel, therefore h_9 can be obtained by $h_9 = h_1$ of (3.7).

⑤There is no non-zero pixel at all (one case in all) on the vertical or horizontal neighbors, in which case the interpolation will not be carried out. For example, h_9 in Fig.3.2 will be zero if h_1 to h_4 are all zero pixels.

It should be emphasized that the texture dependent interpolation only takes use of the nearest four pixels so that the pixels on the diagonal directions will not be taken into account.

To assure the proposed algorithm can interpolate any kinds of image, including those with almost all zero valued pixels (but have few dots being non-zeros), we add 1 to all pixels before the correction process, and subtract 1 from all pixels after the interpolation process. Doing so will avoid misunderstanding about two kinds of zero valued pixels. The first kind of zeros belong to the original image (before correction process), and the second kind are vacancies brought out by the correction process, in which the original image is enlarged.

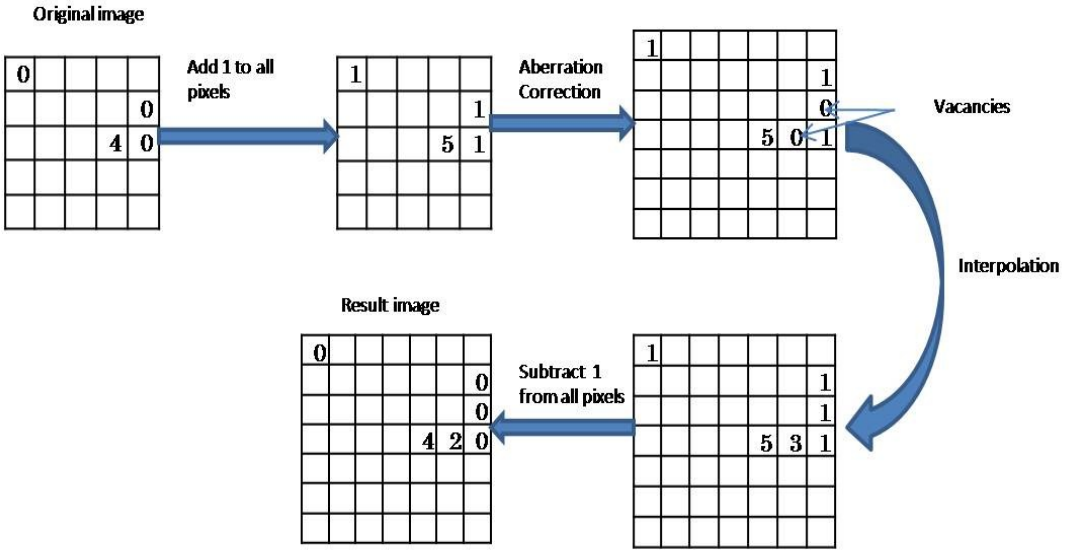

Fig.3.3 A sequence of process of the proposed algorithm, two kinds of zero valued pixels are shown in the above figure, only vacancies will be interpolated.

Compared with overall application of the fundamental algorithms such as nearest neighbor and bilinear interpolation, our algorithm employs a local analysis scheme that can identify to what extent the lost pixels should be interpolated, and then locally apply the three fundamental interpolation methods mentioned above.

The decimal pixel mapping method shown in Fig.3.1 (b) is superior to integer pixel mapping because it can obtain smooth distortion-corrected image without the help of interpolation. Figure 3.4 and 3.5 illustrates the essence of integer and decimal pixel mapping techniques. The pixel grids shown in Fig.3.4 and Fig.3.5 belong to the distorted image and the corresponding corrected image which contains 9 neighboring pixels each. (Not all pixels in Fig.3.4 and Fig.3.5 are numbered)

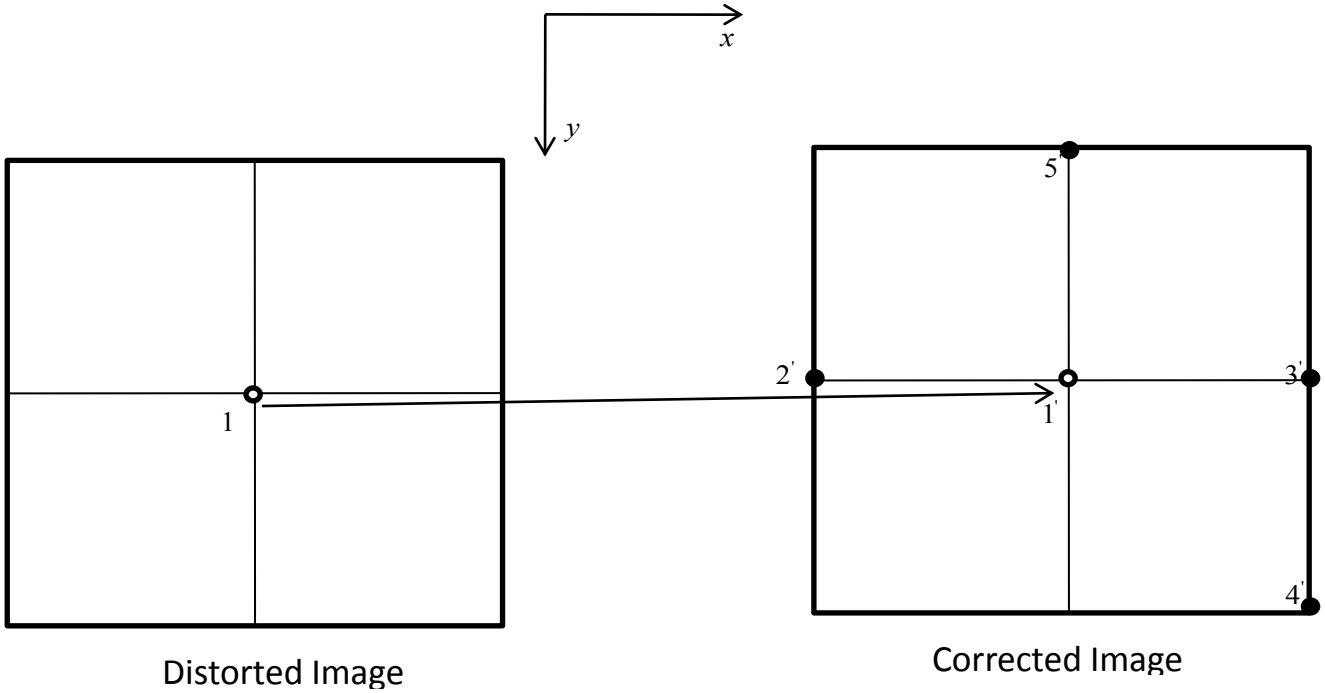

Fig. 3.4 Integer number mapping

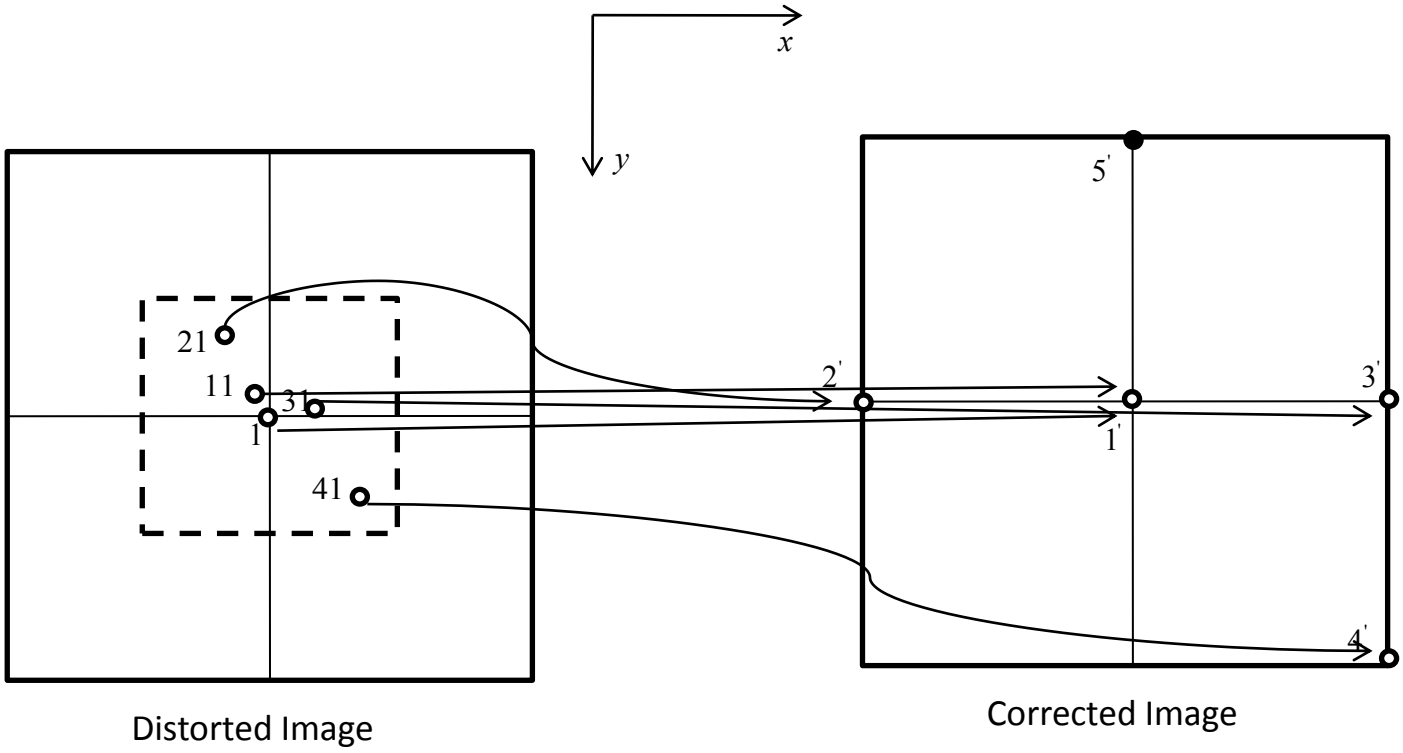

Fig. 3.5 Decimal number mapping

The solid dots in Fig.3.4 and Fig.3.5 represent pixel vacancies with zero value, that is, pixel discontinuity caused by the expansion of the original image, while the hollow dots indicate pixels with non-zero value. In Fig. 3.4, pixel 1(p_1 in short) in a distorted image is transferred to $p_{1'}$ in a corrected image using the integer pixel mapping method. The neighboring pixels around $p_{1'}$: $p_{2'}$ $p_{3'}$ $p_{4'}$and $p_{5'}$, however, have no corresponding pixels in the distorted image. In other words, they cannot be transferred from anywhere of the distorted image but are newly created pixels with zero value. In Fig.3.5, we define some decimal number pixels p_{11} p_{21} $p_{31}$and p_{41} around p_1 in the distorted image within a range (the distance from a decimal pixel to p_1 should not exceed half of the length between two integer pixels), and they are transferred to $p_{2'}$ $p_{3'}$ and $p_{4'}$ in the corrected image by decimal number mapping method. Note that the same positions around $p_{1'}$: $p_{2'}$ $p_{3'}$ and $p_{4'}$, which cannot be mapped by integer pixel mapping are successfully mapped from the decimal pixels. Therefore, we could tell that the number of vacancies in the corrected image is reduced by virtue of the decimal pixel mapping approach.

To describe pixels in Fig.3.4 and Fig.3.5 quantitatively, we define the following mathematical symbols:
In Fig.3.4
Distorted Image:

$$p_1: (x_1, y_1) \tag{3.10}$$

Corrected Image:

$$\left.\begin{aligned} &p_{1'}: (x_1', y_1');\ pv_{1'} = pv_1 \\ &p_{2'}: (x_2', y_2') = (x_1' - 1, y_1');\ pv_{2'} = 0 \\ &p_{3'}: (x_3', y_3') = (x_1' + 1, y_1');\ pv_{3'} = 0 \\ &p_{4'}: (x_4', y_4') = (x_1' + 1, y_1' + 1);\ pv_{4'} = 0 \\ &p_{5'}: (x_5', y_5') = (x_1', y_1' - 1);\ pv_{5'} = 0 \end{aligned}\right\} \tag{3.11}$$

In Fig.3.5
Distorted Image

$$\left.\begin{aligned} &p_1: (x_1, y_1) \\ &p_{11}: (x_{11}, y_{11}) = (x_1 + a_1, y_1 + b_1) \quad -0.5 \le a_1, b_1 \le 0.5 \\ &p_{21}: (x_{21}, y_{21}) = (x_1 + a_2, y_1 + b_2) \quad -0.5 \le a_2, b_2 \le 0.5 \\ &p_{31}: (x_{31}, y_{31}) = (x_1 + a_3, y_1 + b_3) \quad -0.5 \le a_3, b_3 \le 0.5 \\ &p_{41}: (x_{41}, y_{41}) = (x_1 + a_4, y_1 + b_4) \quad -0.5 \le a_4, b_4 \le 0.5 \end{aligned}\right\} \tag{3.12}$$

Corrected Image

$$\left.\begin{aligned} &p_{1'}: (x_1', y_1');\quad pv_{1'} = pv_{11} = pv_1 \\ &p_{2'}: (x_2', y_2') = (x_1' - 1, y_1');\quad pv_{2'} = pv_{21} = pv_1 \\ &p_{3'}: (x_3', y_3') = (x_1' + 1, y_1');\quad pv_{3'} = pv_{31} = pv_1 \\ &p_{4'}: (x_4', y_4') = (x_1' + 1, y_1' + 1);\quad pv_{4'} = pv_{41} = pv_1 \\ &p_{5'}: (x_5', y_5') = (x_1', y_1' - 1);\quad pv_{5'} = 0 \end{aligned}\right\} \tag{3.13}$$

where x_1, y_1 and x_{n1}, y_{n1} denote coordinate index of pixel p_1 and p_{n1} in the distorted image, respectively. x_n', y_n' is coordinate index of pixel $p_{n'}$ in the corrected image. pv_1, pv_{n1} and $pv_{n'}$ indicate pixel value of p_1, p_{n1} and $p_{n'}$, respectively.

According to (3.12), the decimal pixels p_{11} p_{21} $p_{31}$and p_{41} in Fig.3.5 are randomly generated within the range of

$$\left.\begin{aligned} x_1 - 0.5 \le x_{n1} < x_1 + 0.5 \\ y_1 - 0.5 \le y_{n1} < y_1 + 0.5 \end{aligned}\right\} \quad n = 1,2,3,4 \tag{3.14}$$

In general, the coordinate range of the decimal pixels $p_{nm}(x_{nm}, y_{nm})$around an integer pixel $p_m(x_m, y_m)$ in a distorted image can be defined as

$$\left.\begin{aligned} x_m - 0.5 \le x_{nm} < x_m + 0.5 \\ y_m - 0.5 \le y_{nm} < y_m + 0.5 \end{aligned}\right\} \tag{3.15}$$

where *m* indicates the index of an integer pixel in a distorted image, whose maximum value is determined by the resolution of the image. *n* is the index of a decimal pixel around $p_m$within the range defined by (3.15). The pixel value of all the decimal pixels pv_{nm} should be equivalent to the pixel value of the integer pixel pv_m.

In order to avoid minus coordinates of the decimal pixels, the coordinate of the origin should not be positioned to (0,0), (1,0) or (0,1), but to some coordinates that are greater than (1,1). Actually, we

positioned the origin to (101,101) by adding four black borders to the original image that are 100 pixels in width each, which will not only avoid minus coordinates but also the pixel overflow due to the expansion of the original image in the correction process.

Another fact that should not be neglected is that not all decimal pixels can find a corresponding mapping position in the corrected image, and some decimal pixels may overlap with other pixels as well. Actually, there exist three kinds of mapping results by decimal pixel mapping method:

(1) Mapping positions exist in the corrected image and no overlap
This mapping frequently occurs and helps reduce the number of vacancies while the integer pixel mapping fails to do so. For example, $p_{21}$to $p_{2'}$, $p_{31}$to $p_{3'}$and $p_{41}$to $p_{4'}$in Fig.3.5.

(2) Mapping positions exist in the corrected image with position overlap
This mapping also frequently occurs but do not reduce the pixel vacancies. For example, $p_{11}$and p_1 all mapped to $p_{1'}$ in Fig.3.5.

(3) Mapping positions do not exist in the corrected image
This mapping rarely occurs compared with the other two cases. For example, $p_{5'}$in Fig. 3.5 cannot find a mapping position from the distorted image.

In conclusion, the algorithm of two forward mapping methods (integer pixel and decimal pixel mapping) all share the common property that obtains coordinates of distortion-corrected image from the distorted image. The superiority of decimal pixel to integer pixel mapping has also been proved. In the following paragraphs, we will introduce another distortion correction method that is superior to both integer pixel and decimal pixel mapping methods.

2) Backward mapping method:

In contrast to the forward mapping method, the backward mapping method maps pixels from a virtual distortion-free, ideal image to a distorted image. The equation that defines this process is derived from expression (3.3). Rewriting (3.3), the image height in the distorted image can be calculated by

$$y' = \overline{y'} + S\overline{y'}^3 \tag{3.16}$$

The flow chart and a schema of the backward mapping method are illustrated in Fig.3.6 and Fig.3.7, respectively.

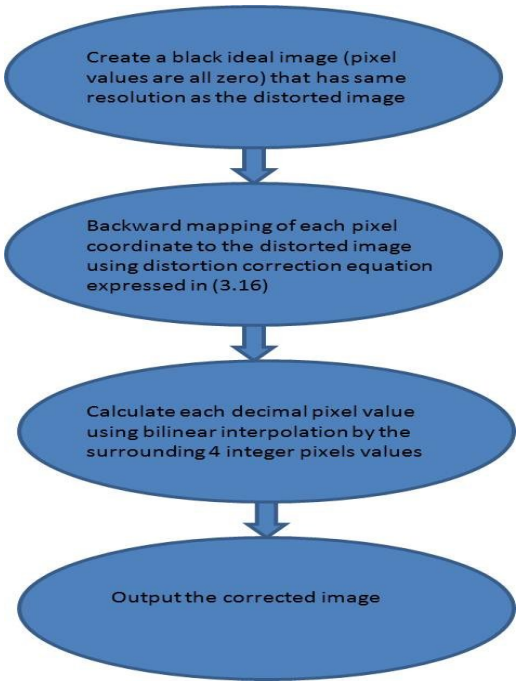

Fig.3.6 Flow chart of the backward mapping method

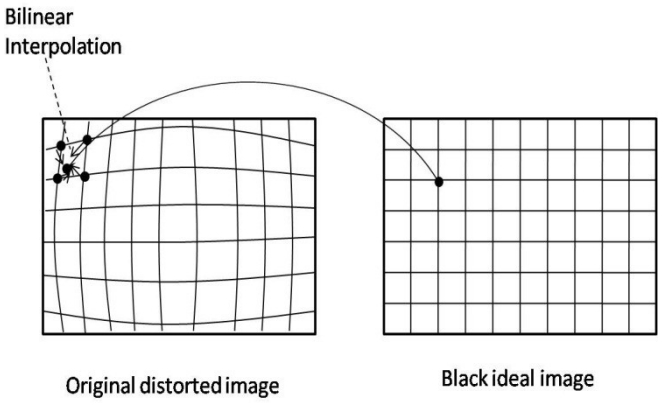

Fig.3.7 Schema of the backward mapping method

According to Fig.3.6, the first step is to create a black ideal image that has the same resolution as the original distorted image. All pixel values are zeros at this step. Then each pixel coordinate from the black ideal image is mapped to the original distorted image by equation (3.16), resulting in decimal pixels (refer to Fig.3.7). The coordinates of the mapped pixels are marked in both the original distorted image and the created black ideal image so that the corresponding positions can be easily found. The next step is to determine pixel value of each decimal pixel by bilinear interpolation from the surrounding four integer pixels in the original distorted image, as illustrated in Fig.3.7. The last procedure is to locate the pixel coordinates in the black ideal image by the corresponding marked positions and fill the black pixels with the interpolated pixel values, then output the corrected image.

3) Comparison between forward mapping and backward mapping methods:

Compared to integer pixel mapping, the backward mapping method proposed in this research will not create any pixel vacancy after correcting distorted image, thus the extra interpolation process is no longer needed. Compared with decimal pixel mapping, in which the interpolation is also unnecessary if the decimal pixels defined are sufficient, the backward mapping also has advantages on the determination of the pixel value. The decimal pixel mapping method, which is also a forward

mapping method, does not create black image, but directly determines pixel value of each randomly created decimal pixel by its nearby integer pixel from the distorted image, In other words, it used a nearest neighbor interpolation to determine each pixel value. In backward mapping method, however, each pixel value of the black ideal image is calculated by bilinear interpolation using four integer pixels around the mapped decimal pixel in the original distorted image. Additionally, the decimal pixel mapping will possibly result in pixel overlapping if too many decimal pixels are defined around an integer pixel as well as pixel loss, whereas the backward mapping will not because its one-to-one pixel mapping mechanism.

3.3 Results and discussions.

3.3.1 Simulation environment and preparation

2D image simulation was carried out on test images and natural color image. The 2D image simulation evaluates the resulting image of a two dimensional object (no optical aberration) using the designed lens system. The resulting image definitely includes all the real optical aberrations, including distortion. Then correction of distortion was carried out to evaluate the distortion correction techniques for the designed single lens system. Before the process of distortion correction, the unit has to be converted from millimeter to pixel because the image being corrected is measured by pixels rather than millimeter. In our lens design, the number of pixels per millimeter can be calculated by using single pixel size 1.4μm ×1.4μm, that is, $1/1.4\mu m = 714.2857$ pixels. Correspondingly, the uint of each variable in equation (3.16) will have to be converted to pixel too.

3.3.2 Simulation results and discussions

The simulation results on distortion correction using third order distortion equation, the field angle dependent coefficient and the three mapping techniques: integer mapping, decimal mapping and backward mapping will be presented and compared in this sub section. We adopt the double convex single lens system introduced in Chapter 2 for this simulation. In the backward mapping method simulation, we set three conditions as follows:

1) Use the third order distortion value at the half maximum field angle to calculate the third order coefficient *S*, then apply this *S* to other field angles to obtain distortion values
2) Use real distortion value at a specific field angle to obtain distortion coefficient *S*, then suppose *S* is a constant to calculate distortions at other field angles. Three different field angles were selected to calculate the constant *S*
3) Use real distortion values of 11 sample points to obtain field-angle dependent coefficient *S*, then use this *S* to calculate distortions at all field angles. It should be emphasized that the maximum number of sample points is determined by the optical design software. Although more samples will give a more precise result for a curve approximation problem, the maximum number of sample points cannot be modified after the lens system is built. 11 is the maximum number of real distortion value allowed by the optical software.

Fig.3.8 –Fig.3.12 show deviations of the distortion values under the above three conditions from the real distortion values $\Delta y'_{dist\_real}$ for 11 sample field angles, respectively.

Under the first simulation condition:

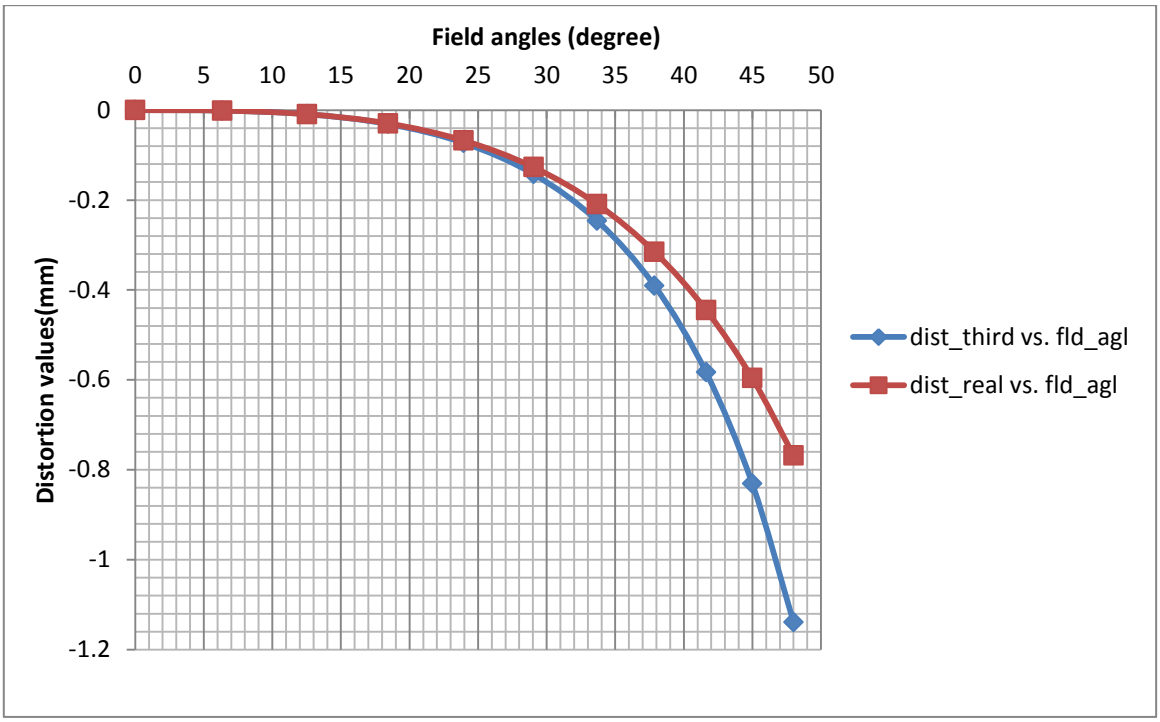

Fig.3.8 Deviations of the third order distortion values from the real distortion values. The square and triangle dots indicate third order distortion and real distortion, respectively. Horizontal axis represents field angles and the vertical axis represents distortion values.

The third order distortion value at the maximum field angle can be read out directly by optical design software after the lens system is built. Then S can be obtained via equation (3.1). As EFL for the double convex single lens is 3.0 mm, the ideal image height $\overline{y}'$at the maximum field angle is obtained from equation (3.5) , that is, $\overline{y}' = f'\tan\omega = 3.0 * \tan 48 = 3.332\text{mm}$. Therefore

$$S = \frac{\Delta y'_{dist}}{\overline{y}'^3} = \frac{-1.140956}{3.332^3} = -0.0308(1/\text{mm}^2)$$

Under the 2nd simulation condition:

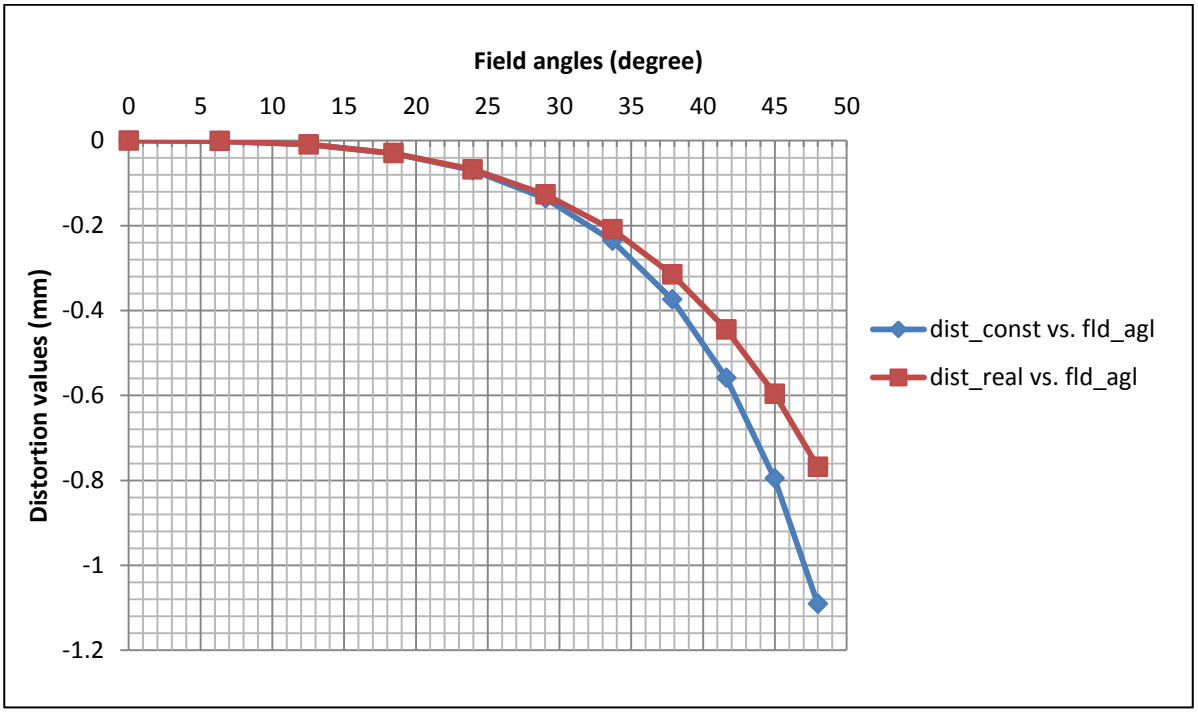

Fig.3.9 Deviations of distortion values calculated by constant coefficient *S* (obtained from real distortion value at 18.43 degree) from the real distortion values. The square and triangle dots indicate distortion calculated by constant coefficient *S* and real distortion, respectively. Horizontal axis represents field angles and the vertical axis represents distortion values.

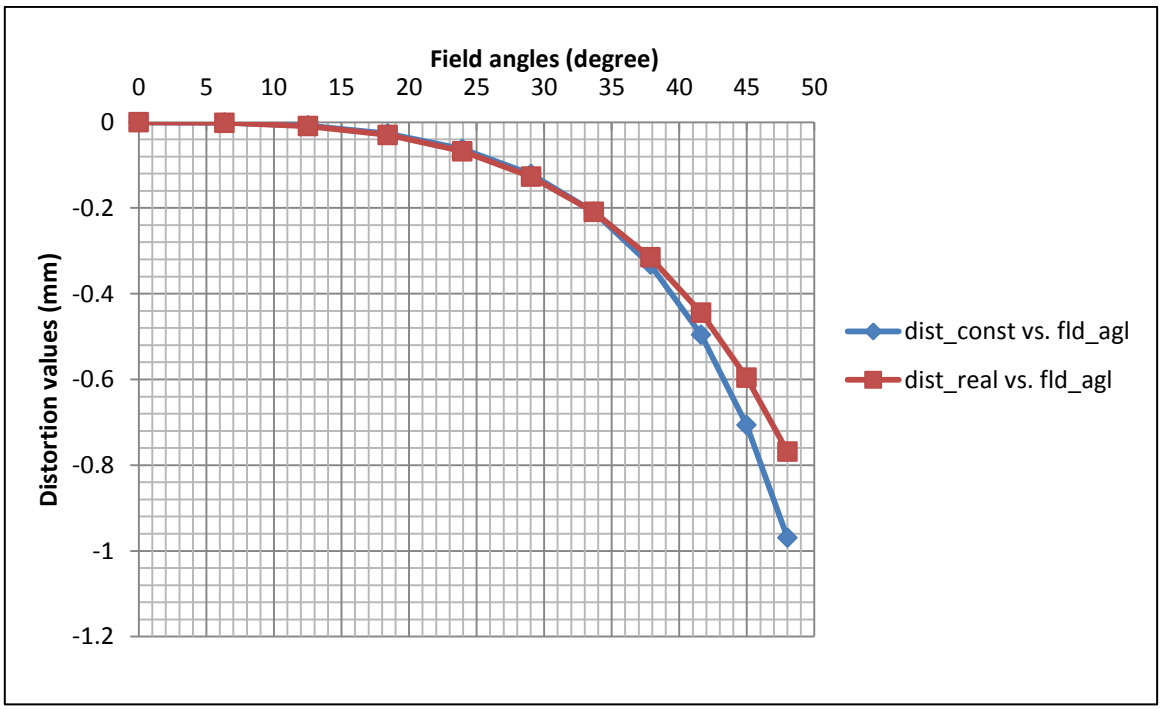

Fig.3.10 Deviations of distortion values calculated by constant coefficient *S* (obtained from real distortion value at 33.68 degree) from the real distortion values. The square and triangle dots indicate distortion calculated by constant coefficient *S* and real distortion, respectively. Horizontal axis represents field angles and the vertical axis represents distortion values.

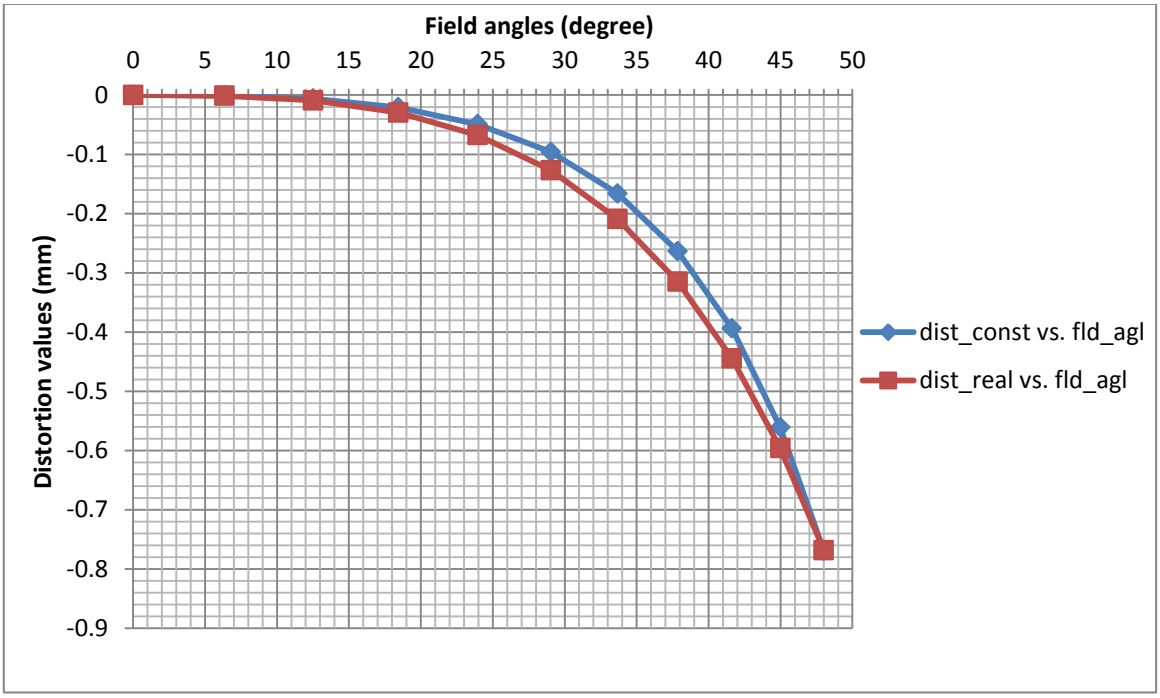

Fig.3.11 Deviations of distortion values calculated by constant coefficient S (obtained from real distortion value at 48 degree) from the real distortion values. The square and triangle dots indicate distortion calculated by constant coefficient S and real distortion, respectively. Horizontal axis represents field angles and the vertical axis represents distortion values.

The constant distortion coefficient S in Fig.3.9 to Fig.3.11 can be computed via equation (3.4)
For Fig.3.9,

$$S = \frac{\Delta y'_{dist\_real}}{\overline{y'}^3} = \frac{-0.0295}{0.9997^3} = -0.0295(1/\mathrm{mm}^2)$$

For Fig.3.10,

$$S = \frac{\Delta y'_{dist\_real}}{\overline{y'}^3} = \frac{-0.2092}{1.9992^3} = -0.0262(1/\mathrm{mm}^2)$$

And for Fig.3.11

$$S = \frac{\Delta y'_{dist\_real}}{\overline{y'}^3} = \frac{-0.7682}{3.3318^3} = -0.0208(1/\mathrm{mm}^2)$$

Under the third simulation condition:

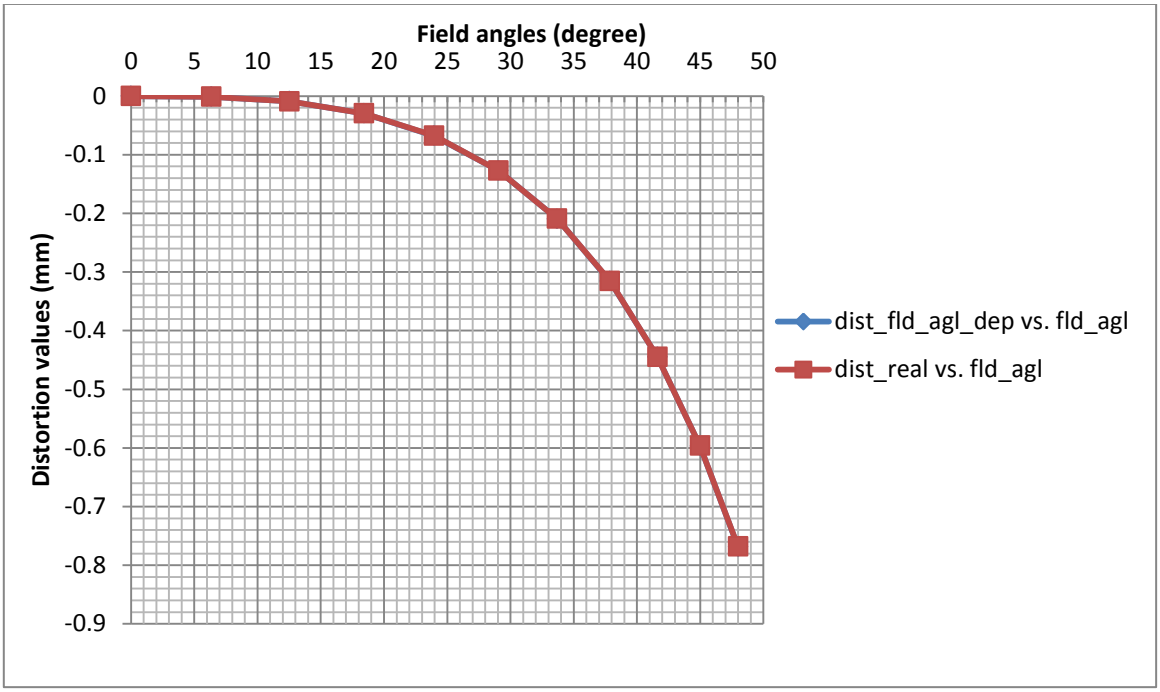

Fig.3.12 Deviations of distortion values calculated by field dependent coefficient *S* from the real distortion values. The square and triangle dots indicate distortion calculated by field dependent coefficient *S* and real distortion, respectively. Horizontal axis represents field angles and the vertical axis represents distortion values.

The third order polynomial relationship curve and equation between field dependent coefficient *S* and ideal image height are showed as well in Fig.3.13 and equation (3.17)

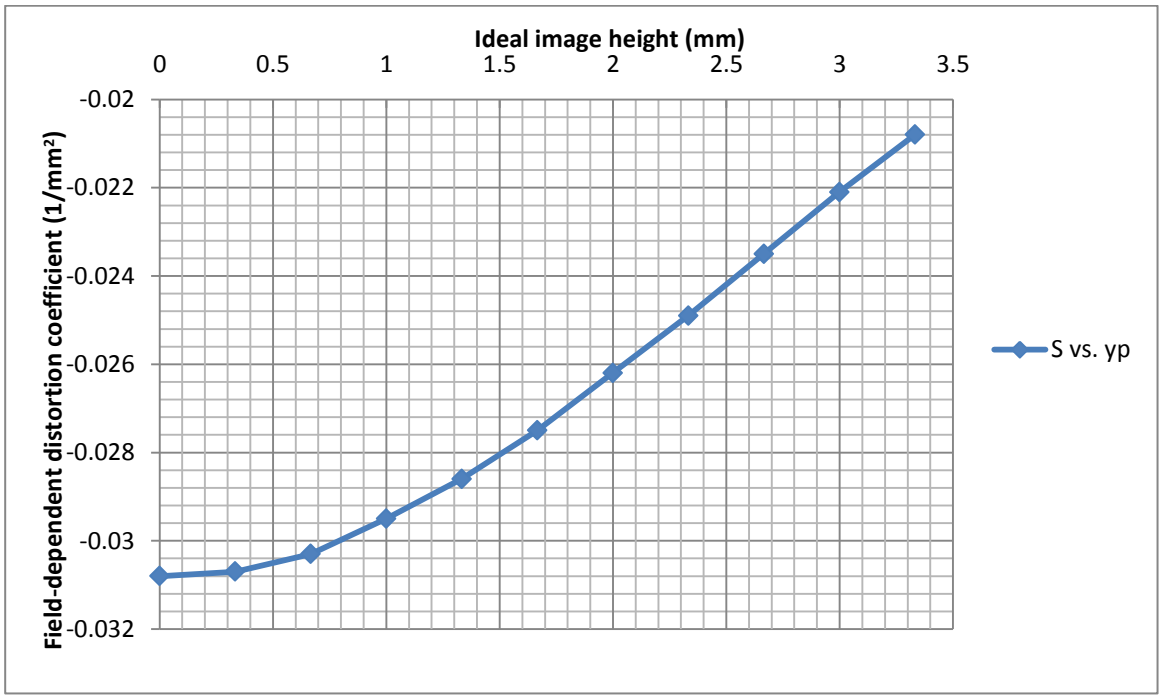

Fig.3.13 The relationship between field angle dependent distortion coefficient and ideal image height. Horizontal axis: ideal image height; Vertical axis: field angle dependent distortion coefficient

$$S = -0.0002063\overline{y}'^{3} + 0.001629\,\overline{y}'^{2} - 0.0001194\overline{y}' - 0.03084 \tag{3.17}$$

Visual comparisons are given from Fig.3.14 to Fig.3.16

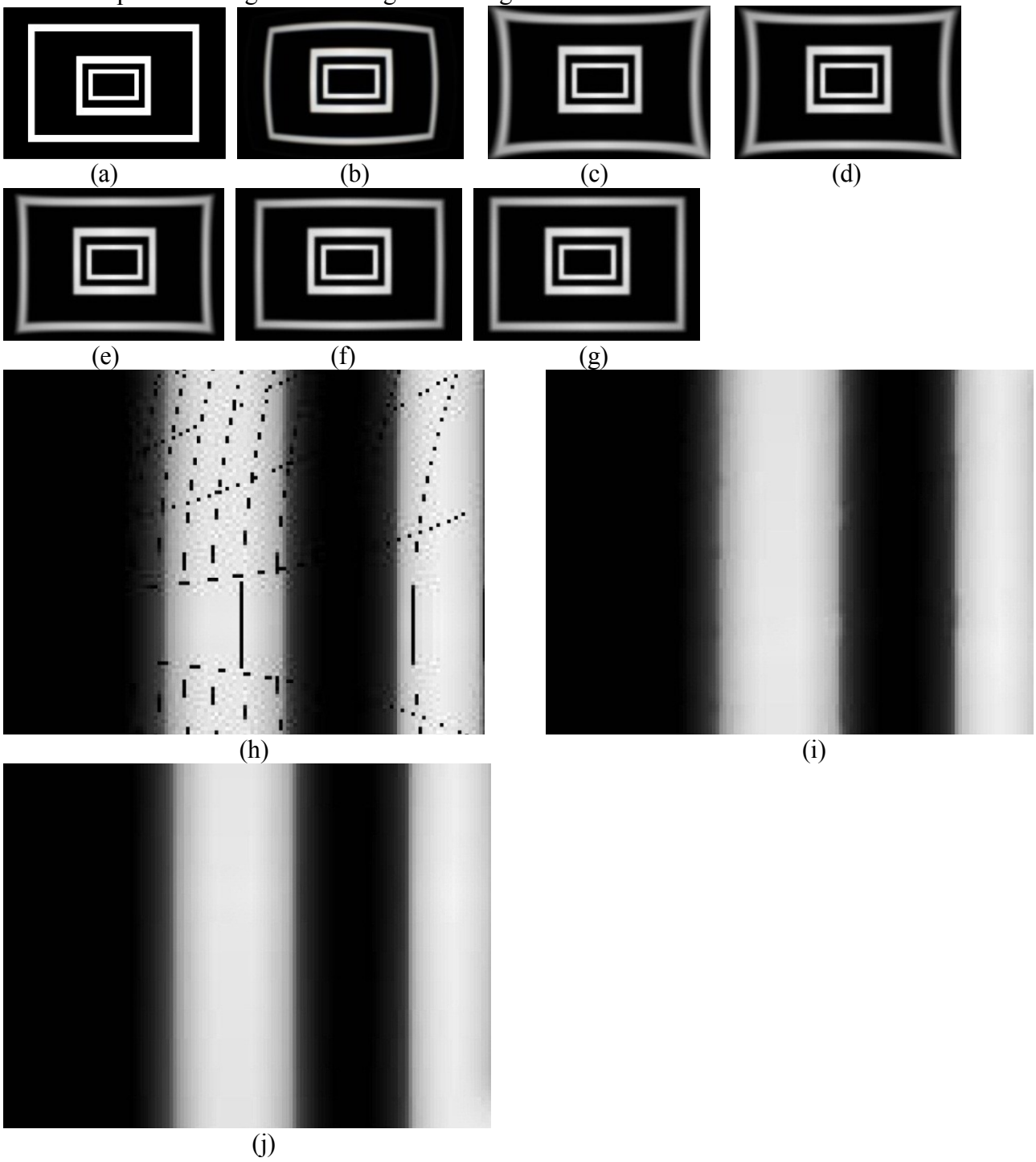

Fig.3.14 Test image 1 simulation: (a) original image without any optical aberration (b) image produced by the double convex single lens system (including all optical aberrations) (c) distortion corrected image using third order coefficient (d) distortion corrected image using constant coefficient (obtained from real distortion value at 18.43 degree) (e) distortion corrected image using constant coefficient (obtained from real distortion value at 33.68 degree) (f) distortion corrected image using constant coefficient (obtained from real distortion value at 48 degree) (g) distortion corrected image using field-angle dependent coefficients (h) zoom in of the distortion corrected image using integer pixel mapping (i) zoom in of the distortion corrected image using decimal pixel mapping (j) zoom in

of the distortion corrected image using field-angle dependent coefficient

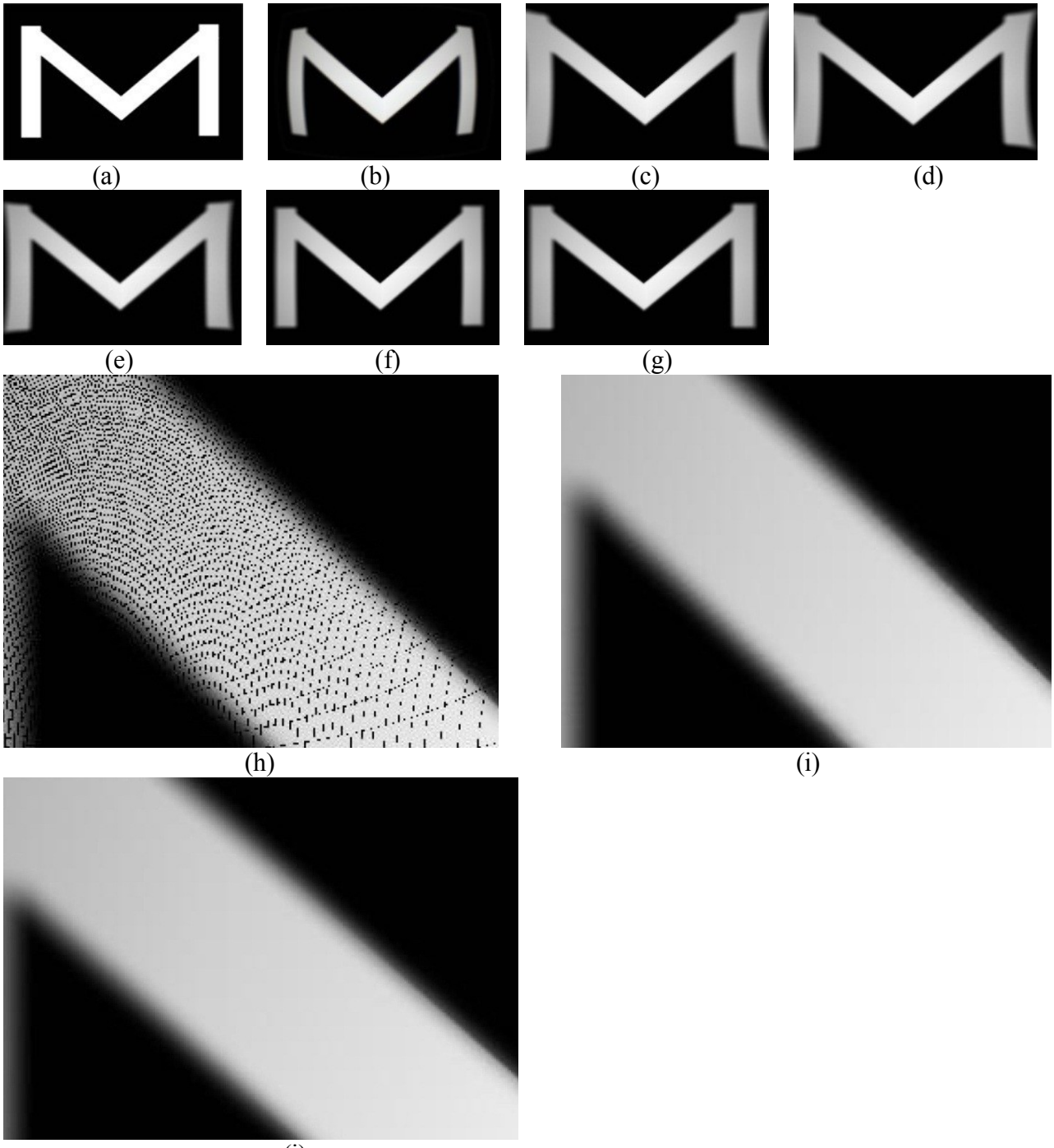

Fig.3.15 Test image 2 simulation: (a) original image without any optical aberration (b) image created by the double convex single lens system (including all optical aberrations) (c) distortion corrected image using third order coefficient (d) distortion corrected image using constant coefficient (obtained from real distortion value at 18.43 degree) (e) distortion corrected image using constant coefficient (obtained from real distortion value at 33.68 degree) (f) distortion corrected image using constant coefficient (obtained from real distortion value at 48 degree) (g) distortion corrected image using field-angle dependent coefficients (h) zoom in of the distortion corrected image using integer pixel mapping (i) zoom in of the distortion corrected image using decimal pixel mapping (j) zoom in of the distortion corrected image using field-angle dependent coefficient

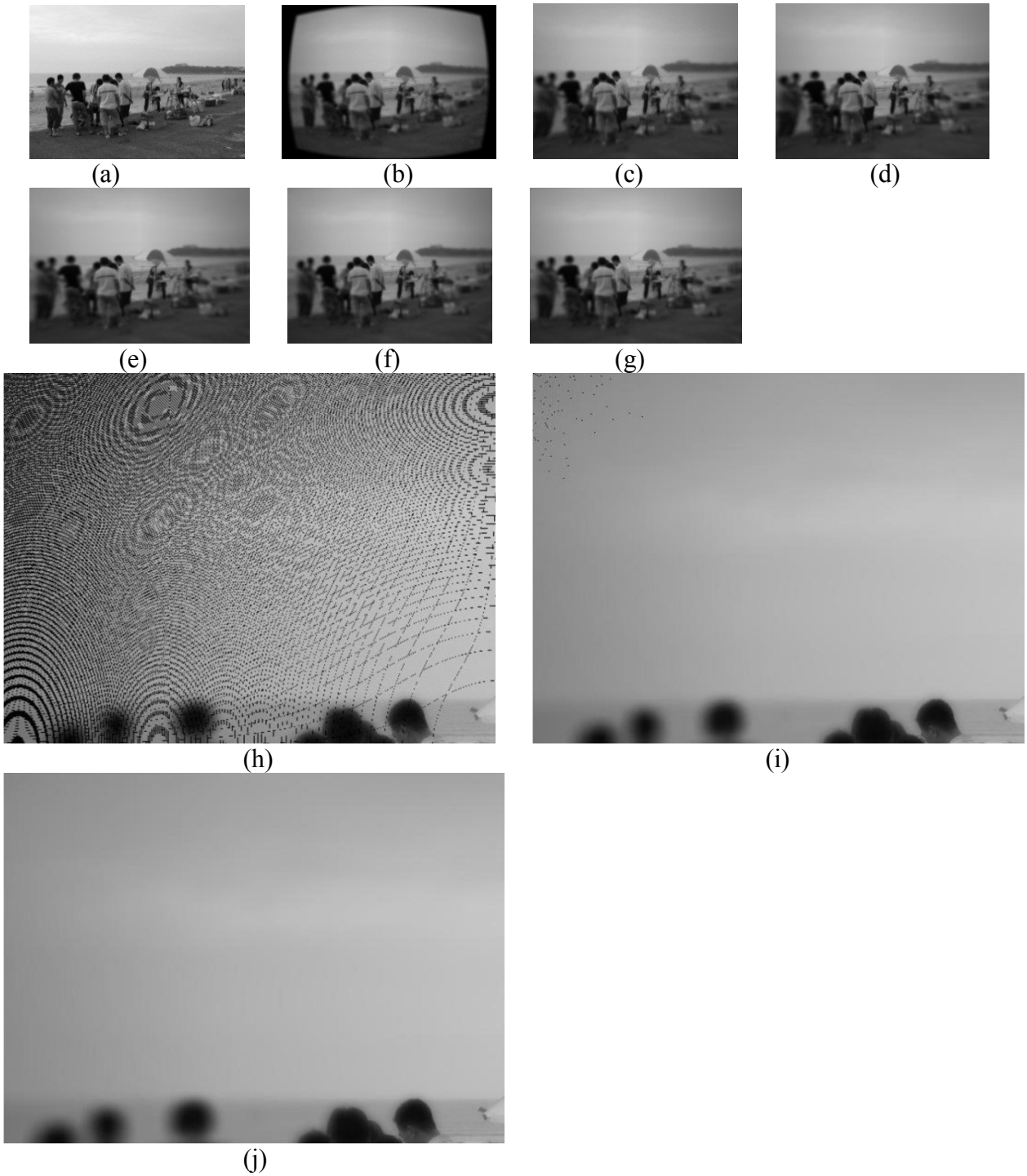

Fig.3.16 Natural color photograph simulation: (a) original image without any optical aberration (b) image created by the double convex single lens system (including all optical aberrations) (c) distortion corrected image using third order coefficient (d) distortion corrected image using constant coefficient (obtained from real distortion value at 18.43 degree) (e) distortion corrected image using constant coefficient (obtained from real distortion value at 33.68 degree) (f) distortion corrected image using constant coefficient (obtained from real distortion value at 48 degree) (g) distortion corrected image using field-angle dependent coefficients (h) zoom in of the distortion corrected image using integer pixel mapping (i) zoom in of the distortion corrected image using decimal pixel mapping (j) zoom in of the distortion corrected image using field-angle dependent coefficient

The simulation results from Fig.3.14 to Fig.3.16 demonstrated that the field angle dependent

coefficient and the backward mapping methods outperform others. We have examined that the maximum deviation occurs at highest field angle (48 degree) of Fig.3.8, Fig.3.9, Fig.3.10 and Fig.3.12, in which the deviation values are 0.3710mm, 0.3229mm, 0.2009mm and 5×10^{-4} mm, respectively. As to Fig.3.11, the maximum deviation 0.0514mm occurs at 37.86 degree. Therefore, the correction results from Fig. 3.14 to Fig.3.16 indicate that visually the most satisfactory corrected image is the one corrected by using field dependent coefficient. Other corrected images, such as the one using the third order coefficient and those using constant coefficients computed at field angle 18.43 and 33.68 degree all appeared over-correction. Although the one using constant coefficient computed at field angle 48 degree is visually satisfactory too, the deviation values from Fig.3.11 indicate that it suffered a little from under-correction problem. On the other hand, the resulting images by using integer pixel mapping method shown in Fig.3.14 (h), Fig.3.15 (h) and Fig.3.16 (h) suggest that the corrected images are visually discontinuous because of too many pixel vacancies. Fig.3.14 (i), (j), Fig.3.15 (i), (j) and Fig.3.16 (i), (j) indicate worse image smoothness for the decimal pixel mapping method than field dependent coefficient method because of the former uses nearest neighbor interpolation to calculate pixel values while the latter uses bilinear interpolation.

So far we have compared results of distortion correction using third order equation and field angle dependent coefficient, as well as the three mapping techniques. However there still are some issues to be discussed. Equation (3.16) introduced in Section 3.2 is actually a sixth order equation because we made a third order polynomial approximation between *S* and $\bar{y}'$. Theoretically, the higher the order of the polynomial approximation between *S* and $\bar{y}'$, the more precise equation (3.1) will represent real distortion values and hence the more accurate resulting image can be obtained. For small maximum field angle case, the order of the approximation could be 0, which means *S* is a constant for all field angles, in which case equation (3.1) will become the distortion term of the traditional third order Seidel aberration. However, large maximum field angle requires higher order approximation in order to precisely represent the distortion value.

In addition, we should emphasize that the field angle dependent coefficient and backward mapping described in this chapter were implemented to barrel distortion case. Actually, these correction techniques are also applicable to pincushion distortion case, in which $\Delta y'_{dist\_real}$ and distortion coefficient *S* will be positive values. As the pincushion image cannot be output by the single lens system designed in this research, we will deal with this case in the future.

Finally, by comparing with the original images, the blurring effect caused by coma, astigmatism and field curvature is clearly visible on the resulting images shown in Fig.3.14 to Fig.3.16, especially at high field angles, though geometrical distortion was corrected. Blurring will not affect distortion correction result that much, while it will greatly affect correction of other aberrations, especially the correction of lateral chromatic aberration. For example, the displacement between R-plane and B-plane of RGB color images can be minimized by real lateral chromatic aberration values. However, there still exists color aberration because the blurring of B-plane is stronger than R-plane and G-plane. We will discuss restoration of the special blur type produced by the spherical double convex single lens: the radially variant blur in Chapter 5.

3.4 Conclusion

In this Chapter, we introduced and compared distortion correction techniques by digital image processing for single lens systems. Field angle dependent coefficient can effectively increase accuracy of real distortion representation by increasing the order of distortion component of the traditional third order Seidel aberration equation. The forward mapping method, which can be further categorized into two methods: integer pixel mapping and decimal pixel mapping, is inferior to the backward mapping

method because the latter is capable of eliminating distortion without producing any pixel vacancy so that the additional interpolation process is not necessary and higher accuracy of pixel value is obtainable because it incorporates the bilinear interpolation algorithm. Simulation results on the double convex single lens system whose specification was already given in Chapter 2 showed that distortion-corrected image using field angle dependent coefficient and backward mapping method obtained the best results both quantitatively and visually. However, radially variant blurring caused by coma, astigmatism and field curvature made the resulting image visually unpleasing, especially at high field regions, though distortion has been eliminated. We will discuss restoration of radially variant blur caused by the double convex single lens in Chapter 5.

3.5 References

[3-1] M.Rebiai, S.Mansouri, F.Pinson, B.Tichit, "Image distortion from zoom lenses: modeling and digital correction", Broadcasting convention, Amsterdam, Netherlands, 438-441(1992)

[3-2] H.Ojanen, "Automatic correction of lens distortion by using digital image processing, Technical Report", Rutgers University, Dept. of Mathematics (Jul. 1999)

[3-3] H. Zeng, R.T. Constable, "Image distortion correction in EPI: comparison of field mapping with point spread function mapping", Magn. Reson. Med., 137–146,(2002)

[3-4] M.Alghoniemy, A.H.Tewfik, "Geometric distortion correction through image normalization", Proc. Int. Conf. Multimedia Expo, vol.3, 1291-1294 (2000)

[3-5] H. Hideaki, Y.Yagihashi & Y.Miyake, "A new method for distortion correction of electronic endoscope images", IEEE Trans. Med. Imaging, 14, 548-555, (Sept.1995)

[3-6] K.V.Asari, S. kumar & D.Radhakrishnan, "A new approach for nonlinear distortion correction in endoscopic images based on least squares estimation", IEEE Trans. Med. Imaging, 18, 345-354 (Apr. 1999)

[3-7] D.Kinder, M.Dorey and D.Smith, "What's the Point? Interpolation and Extrapolation with a Regular Grid DEM", Proceedings of GeoComputation'99, Virginia (Jul.1999)

[3-8] H.C.Andrews and C.L.Patterson, "Digital interpolation of discrete images", IEEE Trans.Comput., vol. C-25, pp.196-202 (Feb.1976)

[3-9] H.S.Hou and H.C. Andrews, "Cubic splines for image interpolation and digital filtering", IEEE Trans.Acoust., Speech, Signal Processing, vol. ASSP-26,pp.856-873 (Sep.1977)

[3-10] B.S. Morse and D.Schwartzwald, "Image magnification using level-set reconstruction", in Proc.Computer Vision and Pattern Recognition, vol.1, pp.I-333-I-340 (2001)

[3-11] H.Aly and E.Dubois, "Regularized image up-sampling using a new observation model and the level set method", in Proc.Int.Conf.Image Processing, vol.3, pp.665-668(Sep.2002)

[3-12] H.Jiang and C.Moloney, "A new direction adaptive scheme for image interpolation", in Proc.Int.Conf.Image Processing, vol.3,pp.369-372 (Jun.2002)

[3-13] Q.Wang, R.K.Ward, "A new orientation-adaptive interpolation method", IEEE Trans.Imag., vol.16,no.4 (Apr. 2007)

[3-14] T.M.Lehmann, C.Gonner, and K.Spitzer, "Survey: Interpolation methods in medical image processing", IEEE Trans. Med.Imag., vol.18,no.11,pp.31-39 (Mar.1982)

[3-15] E.Meijering, "A chronology of interpolation: From ancient astronomy to modern signal and image resampling", Proc.IEEE,vol.90,no.3,pp.319-342 (Mar.2002)

[3-16] H. Nakajima, "Excel de dekiru kougaku sekei", Sin gijiutsu communications (2004) (in Japanese)

[3-17] Y. Zhang, I. Minema, T. Ueda. "A texture dependent interpolation for barrel distorted and longitudinal chromatic aberrated image", IEEJ, Trans. Sensors and Micromachines, 128(11) :423-430(2008)

[3-18] Y. Zhang, I. Minema, T. Ueda. "Geometrically distorted image correction for single lens using

decimal number mapping", Proceedings of the 10th IASTED International Conference on Signal and Image Processing (SIP 2008), 26-31(2008)

[3-19] Y.Zhang, I.Minema, T.Ueda. "Case analysis oriented interpolation and a two-step interpolation after correction of barrel distortion and lateral chromatic aberration", IEEJ Proc.The 24th sensor symposium on sensors, micromachines and applied systems,Tokyo, Japan, 236-239(2007)

[3-20] Y. Zhang, I. Minema, T. Ueda. "Correction of barrel distortion for simple digital camera systems", Joint Conference of Electrical and Electronics Engineers in Kyushu, 470(2006)

Chapter 4 Correction of chromatic aberration

Chapter 4 Correction of chromatic aberration

4.1 Introduction

This chapter demonstrates correction techniques for single lens chromatic aberration. As is mentioned in Chapter 1, chromatic aberration includes axial (or longitudinal) chromatic aberration and lateral (or transverse) chromatic aberration. The former results in different color blurring on the image plane so that the correction approach falls into the image deblurring area. This chapter only deals with the latter: lateral chromatic aberration (LCA will be used for simplicity), which results in displacement between different color planes. The correction can be realized by calibrating from any two color planes to the reference color plane.

A great number of methods have been documented on correction of chromatic aberrations by image processing. A novel method to measure both ACA and LCA in fluorescence microscopy using sub-resolution bead imaging and computer image analysis was proposed by M.Kozubek and P. Matula, in which chromatic aberrations can be reduced to 10-20nm laterally and 10-60 nm axially at a half-an-hour speed[4-1]. Image warping techniques to correct chromatic aberrations was studied by T.E. Boult and G.Wolberg. The warp is determined by edge displacements using cubic spline fitting. Experiments results showed that image warping can reduce Mean Square Error more than active optics approach in the CCTV case and larger reduction of maximum error for other cases [4-2]. There are, however, few literatures discussing single lens design with high field angle and the corresponding approaches to correct LCA by digital image processing. The main reason lays in the difficulty to cope with intensive aberrations at high field angle. Traditional paraxial (first order) aberration equation and the famous third order Seidel aberration equation are only applicable to small field angle. Applying them to large field angle will unavoidably reduce the accuracy of real aberration representation. Due to this fact, the traditional equations should be modified.

In this chapter, we will introduce lateral chromatic aberration (LCA) correction approach using an improved first order lateral chromatic aberration equation. This method suggests that the distance from intersection point of the chief ray and the first lens surface to the optical axis should be a function of real image height of the reference color beams so that the traditional paraxial chromatic aberration equation becomes a higher order polynomial equation. Therefore the accuracy of real chromatic aberration representation increases compared to traditional first-order equation, especially at high field regions. To evaluate this method, simulation on the LCA correction for an aberrated test image generated by optical design software will be introduced and results will be discussed. However, blur-forming aberrations such as axial chromatic aberration (ACA) and field curvature affected the chromatic aberration correction results, making it impossible to eliminate chromatic aberration thoroughly if the blur were not restored prior to chromatic aberration correction.

4.2 Methods

The improved chromatic aberration equation for Lateral chromatic aberration (LCA)

It is well known that chromatic aberration consists of two types: axial chromatic aberration and lateral chromatic aberration. The definition of axial chromatic aberration gives that the refracted light beams propagate from an on-axis object are unable to focus on the same foci because of different wavelengths, which results in color blur on the image plane. Whereas the LCA is defined in terms of light beams propagate from off-axis object, whose magnifications are slightly different, resulting in displacement between different colors on the image plane. The drawings for the two types of chromatic aberration are illustrated in Fig.4.1 and Fig.4.2.

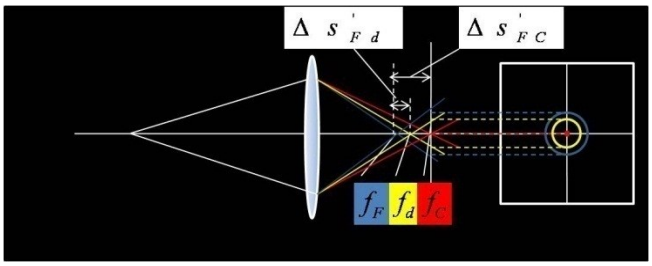

Fig.4.1 Axial chromatic aberration (ACA)

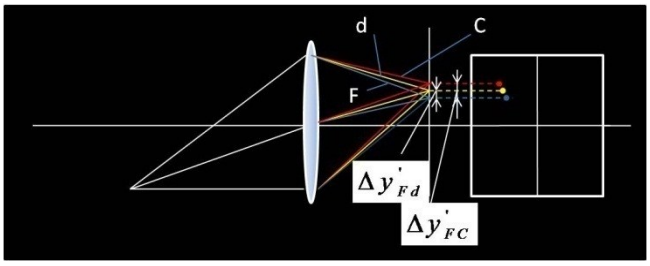

Fig.4.2 LCA in the absence of ACA

The traditional first order chromatic aberration equation takes the following form [4-3]:

For ACA:

$$\Delta s'_{FC} = (1-\beta)^2 \Delta f_{FC} \tag{4.1}$$

$$\Delta s'_{Fd} = (1-\beta)^2 \Delta f_{Fd} \tag{4.2}$$

For LCA:

$$\Delta y'_{FC} = k_1 h^* (k_1 = \frac{\Delta s'_{FC}}{f_d}) \tag{4.3}$$

$$\Delta y'_{Fd} = k_2 h^* (k_2 = \frac{\Delta s'_{Fd}}{f_d}) \tag{4.4}$$

$\Delta s'_{FC}, \Delta s'_{Fd}$: first order ACA between F line (486.1nm)and C line (656.2nm) light beams, F line and d line (587.6nm) light beams, respectively

β: Magnification of the lens system

Δf_{FC} , Δf_{Fd} : Displacement of focal lengths between F and C line light beams, F and d line light beams, respectively. ($\Delta f_{FC} = f_F - f_C; \Delta f_{Fd} = f_F - f_d$)

$\Delta y'_{FC}$, $\Delta y'_{Fd}$: first order LCA between F line and C line light beams, F line and d line light beams, respectively

k_1, k_2: first order chromatic aberration coefficients

f_d: Focal length of the reference ray

h^*: Distance from the intersection point of chief ray and the first lens surface (refer to Fig.4.3) to the optical axis

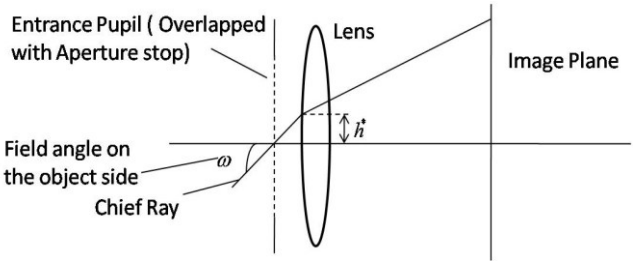

Fig.4.3 Distance from the intersection point of chief ray and the first lens surface to the optical axis

It is obvious that h^* is a field-dependent variable by observing relation between h^* and field angle ω in Fig.4.3 and therefore is also related to the image height on the image plane.

In the case of infinite object, equation (4.1) and (4.2) could be simplified to

$$\Delta s'_{FC} = \Delta f_{FC} \tag{4.5}$$

$$\Delta s'_{Fd} = \Delta f_{Fd} \tag{4.6}$$

Correspondingly, equation (4.3) and (4.4) can be rewritten as

$$\Delta y'_{FC} = k_1 h^* (k_1 = \frac{\Delta f_{FC}}{f_d}) \tag{4.7}$$

$$\Delta y'_{Fd} = k_2 h^* (k_2 = \frac{\Delta f_{Fd}}{f_d}) \tag{4.8}$$

Based on the first order LCA equations (4.7) and (4.8) that show the first order relations between $\Delta y'_{FC}$ and h^*, $\Delta y'_{Fd}$ and h^*, respectively, an improved equation can be derived to deal with LCA correction problem for large field angle. The improved equation considers h^* as a function of real image height y'_F (y'_C or y'_d is also possible, it depends on which color plane is the standard color plane so that other two color planes will be corrected with respect to it. In this study, B-plane of the RGB image is regarded as the standard color plane, therefore, real image height y'_F will be measured), forming a polynomial expression as follows:

$$h^* = a_1 y'^{n}_F + a_2 y'^{n-1}_F + a_3 y'^{n-1}_F + ... + a_n y'_F (n = 1,2,3,...) \tag{4.9}$$

Then substitute (4.9) into equation (4.7) and (4.8), which yields

$$\Delta y'_{FC\_real} = k_1 (a_1 y'^{n}_F + a_2 y'^{n-1}_F + a_3 y'^{n-1}_F + ... + a_n y'_F)(n = 1,2,3,...) \tag{4.10}$$

$$\Delta y'_{Fd\_real} = k_2 (a_1 y'^{n}_F + a_2 y'^{n-1}_F + a_3 y'^{n-1}_F + ... + a_n y'_F)(n = 1,2,3,...) \tag{4.11}$$

Note that the LCA notation $\Delta y'_{FC}$ and $\Delta y'_{Fd}$ have been replaced by $\Delta y'_{FC\_real}$ and $\Delta y'_{Fd\_real}$, which indicates real aberration values rather than first order values. When the field angle is not too high, the real aberration values are almost equal to the first order values and using first order polynomial relation between h^* and y'_F is accurate enough to represent these aberration values. In this case equation (4.10) and (4.11) become the traditional first order LCA equation

$$\Delta y'_{FC\_real} = \Delta y'_{FC} = k_1 a y'_F \tag{4.12}$$

$$\Delta y'_{Fd\_real} = \Delta y'_{Fd} = k_2 a y'_F \tag{4.13}$$

However, when the field angle is too large, real aberration values are no longer equal to the first order values and higher polynomial relation between h^* and y'_F has to be used to accurately represent LCA values. Simulations have been carried out to verify it in Section 3.

One last thing that needs to be emphasized is that the constant term of the polynomial expression is neglected because h^* will equal to zero if the real image height y'_F equals zero.

4.3 Results and discussions

4.3.1 Description of simulations

In this section, image simulations are carried out to evaluate the proposed lateral chromatic aberration correction approach for high maximum field angle single lens. The simulations use two-dimensional image object whose resolution is 768×768 to examine the resulting image after the single lens. The resulting image will include all kinds of optical aberrations, both mono-chromatic and chromatic. A test image is used in this simulation.

4.3.2 Simulation results and discussions

In this simulation, deviation graphs and resulting images for first and third order polynomial approximations between h^* and y'_F are illustrated and compared. It is important to emphasize that theoretically higher order of the polynomial approximation equations is more precise to represent real LCA values. The highest order of polynomial approximation in our simulation is three because we proved by the following deviation graphs (Fig.4.4) and visual comparisons (Fig.4.6 to Fig.4.13) that third order is satisfactory enough to represent real aberration values, it is not necessary to use higher order.

The deviation graphs are as follows:

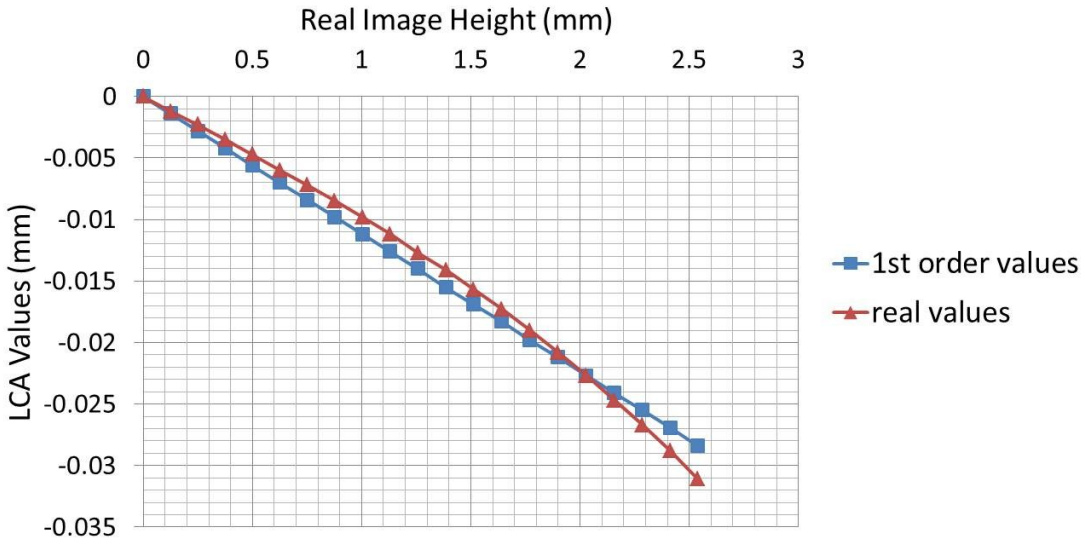

(a) LCA between F line and C line light beams for first order approximation

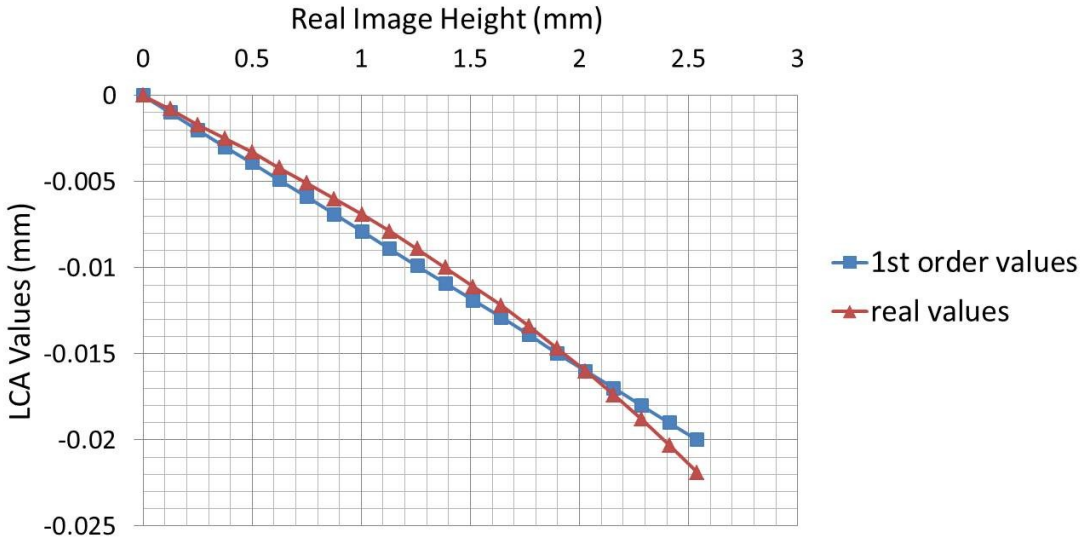

(b) LCA between F line and d line light beams for first order approximation

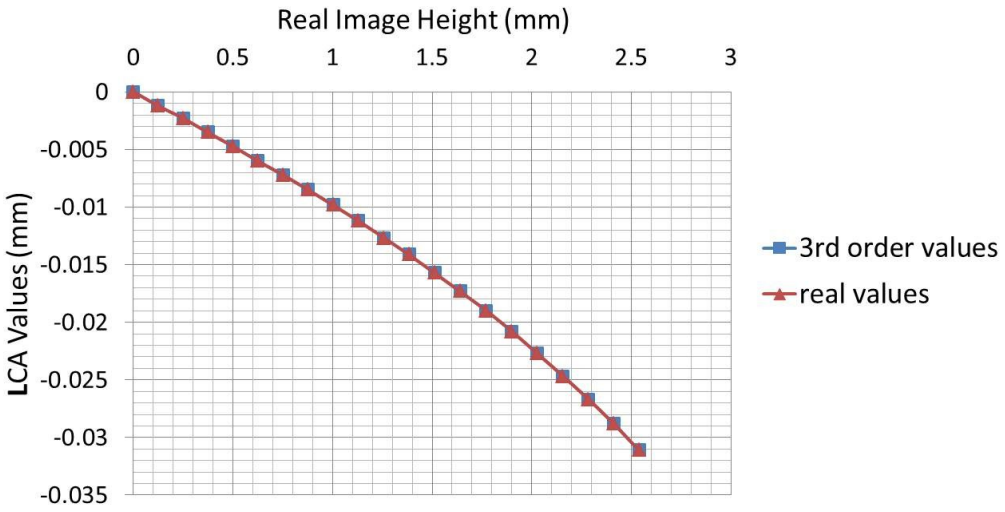

(c) LCA between F line and C line light beams for third order approximation

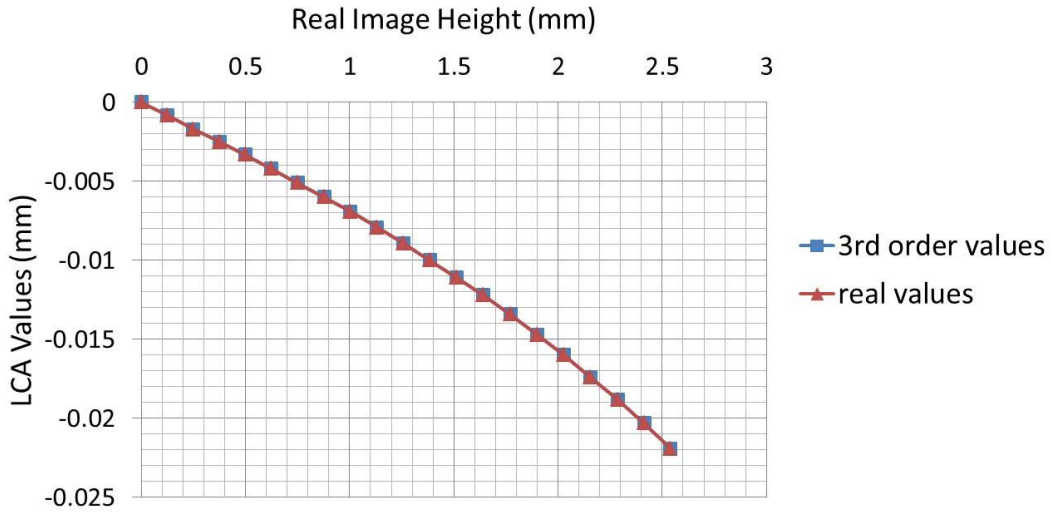

(d) LCA between F line and d line light beams for third order approximation

Fig.4.4 Deviation graphs of LCA values versus real image height

The deviation graphs in Fig.4.4 show how the LCA values calculated from first and third order approximations between h^* and y'_F deviate from real LCA values. Fig.4.4 (a),(b) show the graphs for first order case and Fig.4.4 (c),(d) show the third order case. Meanwhile,(a) and (c) show the LCA values between F line and C line light beams while (b) and (d) show the LCA values between F line and d line light beams. The horizontal axis is the real image height y'_F, which is obtained by real ray tracing of F line light beams' chief ray, while the vertical axis represents LCA values. In each graph, the curve with square dots indicates LCA values calculated from first or third order approximations between $h^*$and y'_F while the curve with triangle dots indicates real LCA values.

The deviation graphs were obtained by the following procedures:

Firstly, obtain the polynomial approximation equations:

The polynomial approximation is obtained by curve fitting of h^*, y'_F pairs for several field angles, with h^* at each angle calculated by

$$h^* = \frac{\Delta y'_{FC\_real}}{k_1} \tag{4.14}$$

$$h^* = \frac{\Delta y'_{Fd\_real}}{k_2} \tag{4.15}$$

The number of h^*, y'_F pairs was 21, which was determined by the number of real LCA values output of the optical simulation tool. Although curve fitting on more sample data will definitely increase accuracy, the number of output cannot be modified.

Here real LCA value $\Delta y'_{FC\_real}$ and $\Delta y'_{Fd\_real}$ is obtained by real ray tracing of F, d and C line light beams' chief rays and then measuring their displacements on the image plane. The k_1 and k_2 can be calculated using equation (4.7) and (4.8).

For example, $\Delta y'_{FC\_real}$ and $\Delta y'_{Fd\_real}$ at the maximum field angle 48 degree are -0.03106mm and -0.021898mm, respectively. And

$$k_1 = \frac{\Delta f_{FC}}{f_d} = \frac{2.938875 - 3.022435}{2.997563} = -0.027876$$

$$k_2 = \frac{\Delta f_{Fd}}{f_d} = \frac{2.938875\text{-}2.997563}{2.997563} = -0.019579$$

Therefore h^* at this field angle can be calculated by

$$h^* = \frac{\Delta y'_{FC\_real}}{k_1} = \frac{-0.03106}{-0.027876} = 1.1142mm$$

$$h^* = \frac{\Delta y'_{Fd\_real}}{k_2} = \frac{-0.021898}{-0.019579} = 1.1184mm$$

Note that theoretically h^* should be an invariant at a specific field angle no matter it is calculated from real LCA between F and C line light beams or LCA between F and d line light beams. The different values of h^* shown here, however, indicates there exist small errors for the realistic situation.

Then the first and third order polynomial equations between h^* and y'_F can be obtained by curve fitting:

For first order case between F line and C line light beams

$$h^* = 0.4006 y'_F \tag{4.16}$$

For first order case between F line and d line light beams

$$h^* = 0.4023 y'_F \tag{4.17}$$

For third order case between F line and C line light beams

$$h^* = 0.01587 y'^3_F + 0.000464 y'^2_F + 0.3352 y'_F \tag{4.18}$$

For third order case between F line and d line light beams

$$h^* = 0.01584 y'^3_F + 0.000547 y'^2_F + 0.3368 y'_F \tag{4.19}$$

Secondly, substitute the polynomial approximation equations (4.16) to (4.19) into (4.7) and (4.8) to obtain equations (4.20) to (4.23), which represent LCA for first and third order cases, hence the blue curves can be obtained:

For the first order case:

$$\Delta y'_{FC} = k_1 h^* = -0.0112 y'_F \tag{4.20}$$

$$\Delta y'_{Fd} = k_2 h^* = -0.0079 y'_F \tag{4.21}$$

For the third order case:

$$\Delta y'_{FC} = k_1 h^* = -4.4239\times10^{-4} y'^3_F - 1.2934\times10^{-5} y'^2_F - 0.0093 y'_F \tag{4.22}$$

$$\Delta y'_{Fd} = k_2 h^* = -3.1013\times10^{-4} y'^3_F - 1.071\times10^{-5} y'^2_F - 0.0066 y'_F \tag{4.23}$$

Finally, read the real LCA values of the 21 sample points from the output of the optical simulation tool and then connect them together to obtain the red curve. By doing this, the deviations between first order, third order values and real LCA values at all field angles can be compared visually.

Quantitatively, the deviations can then be calculated by

$$Dev_{FC} = \Delta y'_{FC} - \Delta y'_{FC\_real} \tag{4.24}$$

$$Dev_{Fd} = \Delta y'_{Fd} - \Delta y'_{Fd\_real} \tag{4.25}$$

Note that the optical simulation tool can only output 21 sample data. Therefore we could only obtain 21 sets of deviation values by the above equations.

By examining the deviation graphs shown in Fig.4.4, we know that visually the third order curve is much closer to real LCA curve compared with first order curve. It overlapped with the real LCA curve. The first order curve, however, shows that the calculated LCA values are greater (in absolute value) than real LCA values when the real image height is less than 2.03mm (field angle 38.4 degree), which indicates over-correction. When the real image height becomes greater than 2.03mm, the calculated LCA values are smaller (in absolute value) than real LCA values, which results in under-correction. Quantitatively, we calculated and compared the maximum deviations for each graph: The maximum deviations of the first order case (Fig.4.4 (a) and (b)) are 0.0027mm and 0.0019mm, which occurred at the position where y'_F is 2.540mm (field angle 48 degree). The maximum deviation of the third order case (Fig.4.4 (c) and (d)) are 2.511×10^{-6}mm and 2.99×10^{-6} mm, which occurred at the position where y'_F is 1.385mm and 2.157mm (field angle 26.4 and 40.8 degree), respectively. This indicates that the maximum deviation of the third order case is far smaller than that of the first order case, which means the LCA values calculated by third order approximation is far more accurate than first order approximation. It is also not necessary to use higher order polynomial approximations because the deviation of the third order case is already small enough.

Then the corresponding LCA corrected resulting images for first and third order cases and also the original image and the image before LCA correction are given below from Fig.4.5 to Fig.4.13 for comparison:

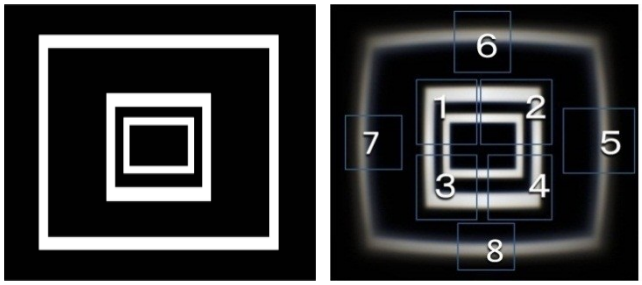

(a) Original (b) before LCA correction

Fig.4.5 Image comparison for test image

In Fig.4.5 (b), the image before LCA correction is obtained by 2D imaging of the original image through the designed single lens. It includes all optical aberrations.

As the effect of color aberration in the overall view of the image cannot be seen clearly, we zoomed

in several regions of Fig.4.5 (b), which are marked with region numbers. 8 regions are selected for the test image, where 4 of them are low field regions and the other 4 are high field regions. The comparison of zoom-in images are shown in Fig.4.6 to Fig.4.13.

Image before LCA correction Corrected by first order Corrected by third order

Fig.4.6 Image comparison before and after LCA correction for region 1

Image before LCA correction Corrected by first order Corrected by third order

Fig.4.7 Image comparison before and after LCA correction for region 2

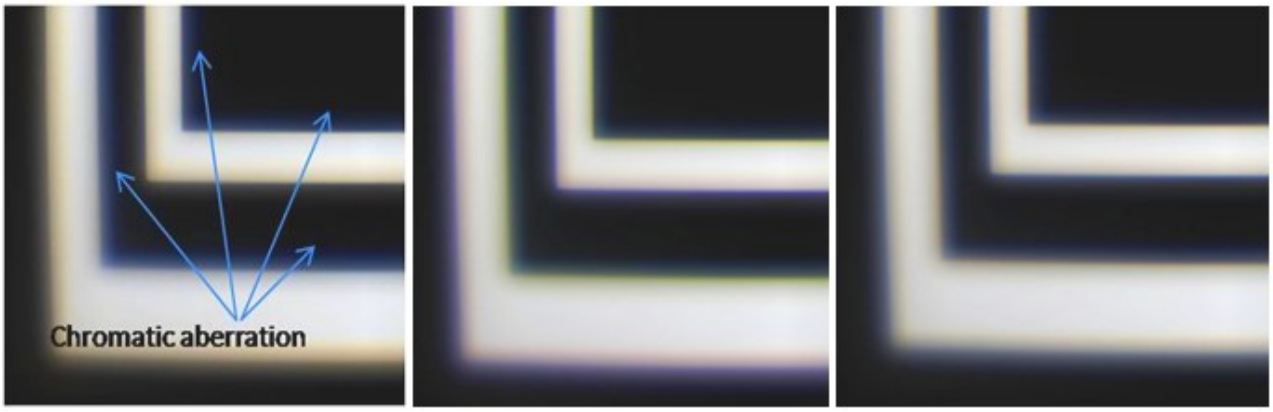

Image before LCA correction Corrected by first order Corrected by third order

Fig.4.8 Image comparison before and after LCA correction for region 3

Image before LCA correction Corrected by first order Corrected by third order

Fig.4.9 Image comparison before and after LCA correction for region 4

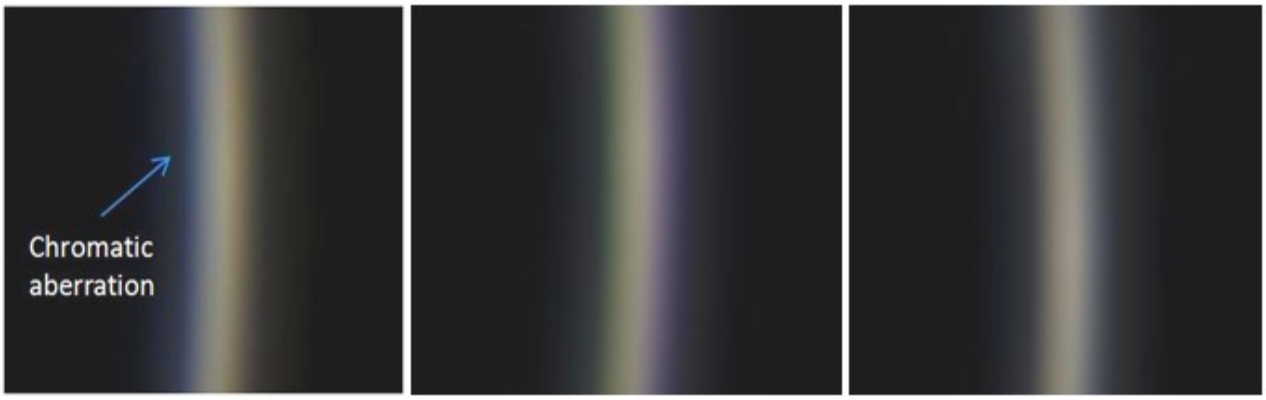

Image before LCA correction Corrected by first order Corrected by third order

Fig.4.10 Image comparison before and after LCA correction for region 5

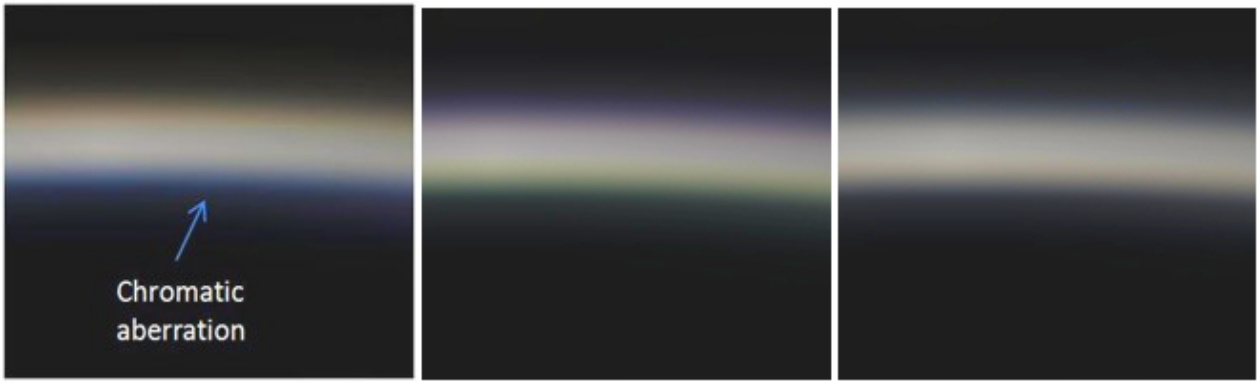

Image before LCA correction Corrected by first order Corrected by third order

Fig.4.11 Image comparison before and after LCA correction for region 6

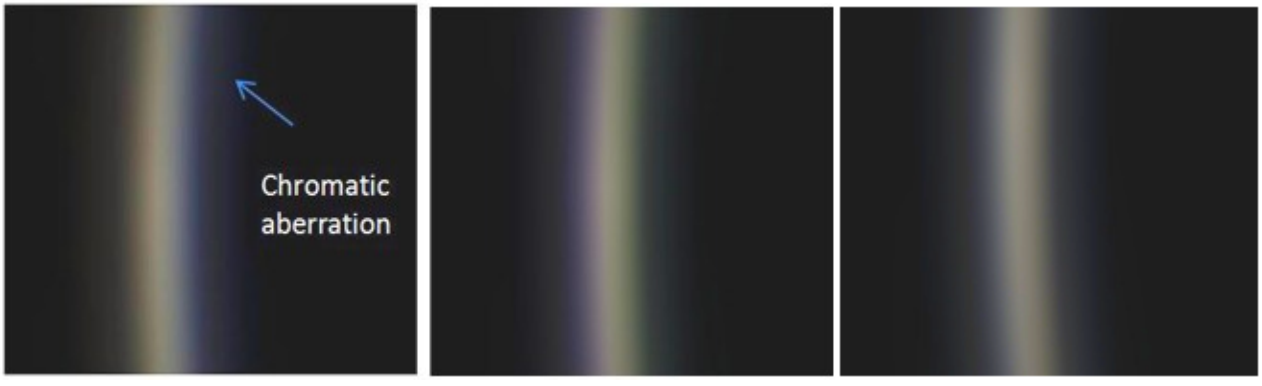

Image before LCA correction Corrected by first order Corrected by third order

Fig.4.12 Image comparison before and after LCA correction for region 7

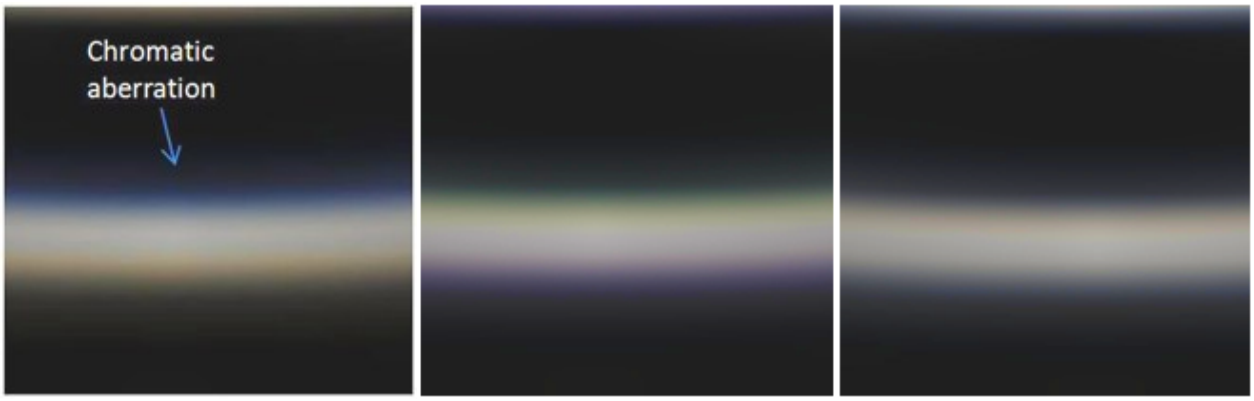

Image before LCA correction Corrected by first order Corrected by third order

Fig.4.13 Image comparison before and after LCA correction for region 8

In Fig.4.6 to Fig.4.13, the chromatic aberration is visible around the borders of the white and black area (We marked it by arrows in the image before LCA correction. The corrected images are not marked). For images before LCA correction, blue color blur can be seen on the inner borders but cannot be seen on the outer borders. For the corrected image of the first order case, the resulting images all appear to be over-correction: the inner border is dark green and the outer border is light purple. For the corrected image of the third order case, the chromatic aberration of blue is minimized to some extent: blue blur is dimmed on the inner borders and also appeared dimmed on the outer borders (low field regions are more obvious than high field regions), the reason why it cannot be eliminated thoroughly is that the differences of blur between different colors on the image plane caused by axial chromatic aberration (ACA) and other monochromatic aberrations such as field curvature affected the chromatic aberration correction results even if LCA is eliminated. This will be verified by the following real ray tracing shown in Fig.4.15 and Fig.4.16, and the quantitative RGB blur charts (in our case, we regard C,d and F line light beams as R,G,B light beams, respectively) shown in Fig.4.17 and quantitative blur size listed in Tab.4.1.

Before giving the real ray tracing result and the RGB blur charts, a simple case that the LCA is only affected by ACA should be briefly described to help understand more complicated case. Theoretically, LCA that affected only by ACA (without other monochromatic optical aberrations) can be illustrated in Fig.4.14.

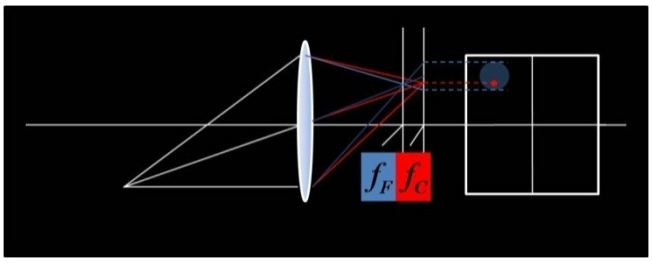

Fig.4.14 LCA affected only by ACA (Only R and B light beams are drawn)

It can be observed that when image plane is placed on foci of red (R) beams, the image plane will show sharp red image but blurred blue image. As the LCA correction only modify the spatial displacement between R,G and B plane, the blue blur will certainly visible even if the LCA is corrected.

Nevertheless, the realist situation is not that simple. Fig.4.15 gives the real ray tracing for our single lens system for four different field angles: 0, 19.2, 33.6 and 48 degree. The rays being traced are chief

rays, upper meridional rays and the lower meridional rays of RGB light beams at the four angles. Fig.4.16 shows the zoom-in image of Fig.4.15 at the maximum field angle 48 degree to illustrate the differences of blur between different colors on image plane.

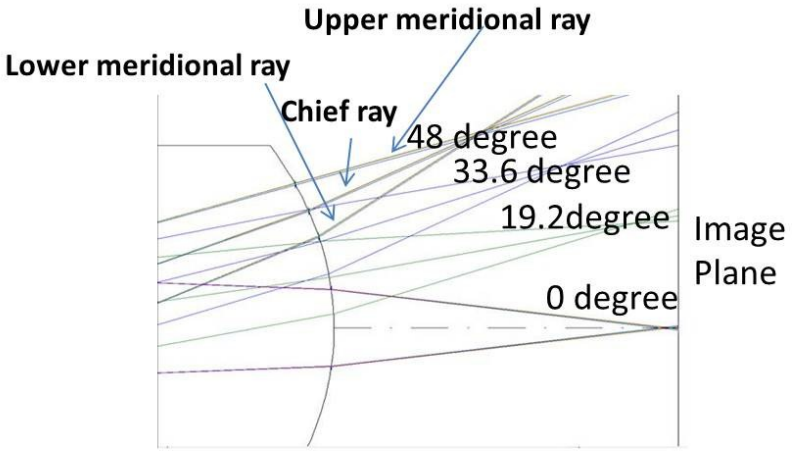

Fig.4.15 Real ray tracing at different field angles

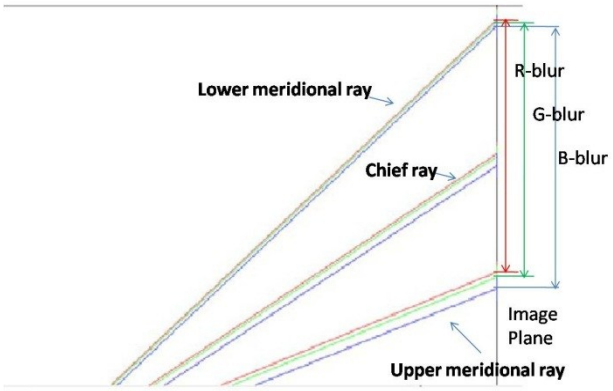

Fig.4.16 Zoom in of Fig.4.15 at the maximum field angle

Quantitatively, we give the RGB blur (in diameter of the blur circle) charts before and after LCA correction at three field angles in Fig.4.17 from the range 0 to 48 degree and also measured the blur size, which is listed in Tab.4.1.

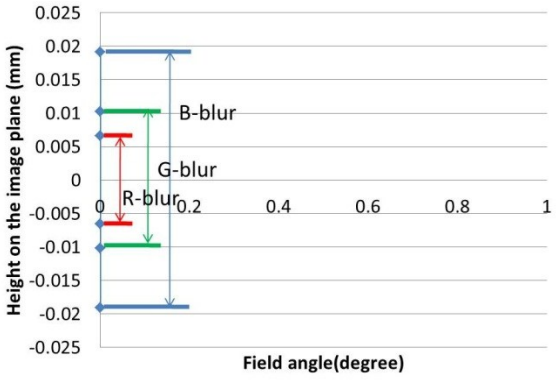

(a) RGB blur before LCA correction at 0 degree

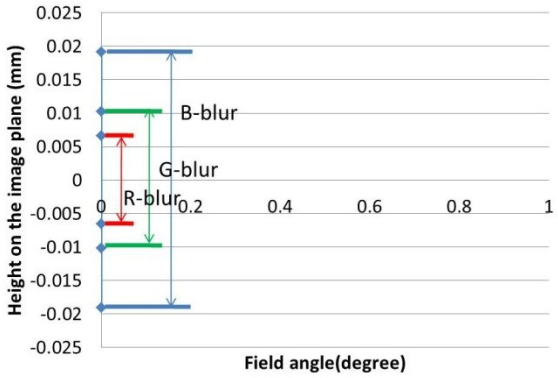

(b) RGB blur after LCA correction at 0 degree

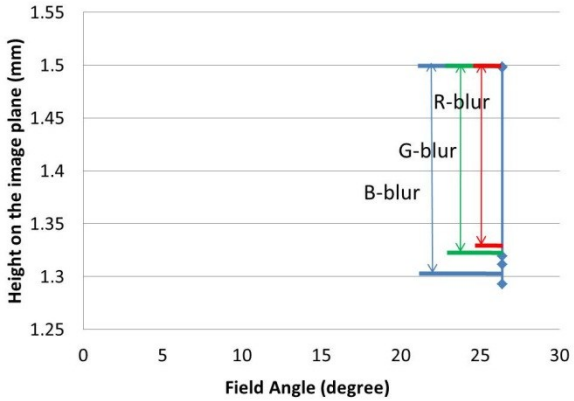

(c) RGB blur before LCA correction at 26.4 degree

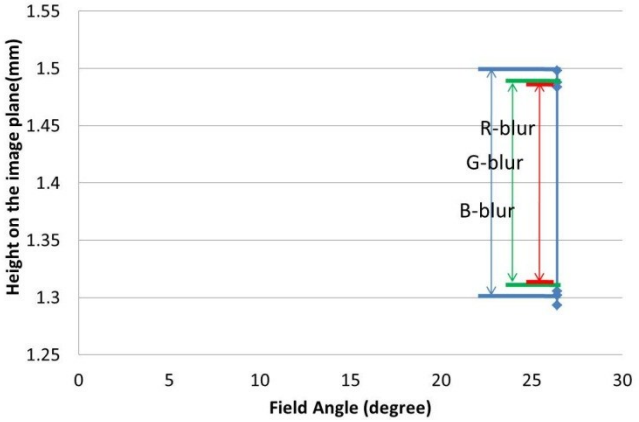

(d) RGB blur after LCA correction at 26.4 degree

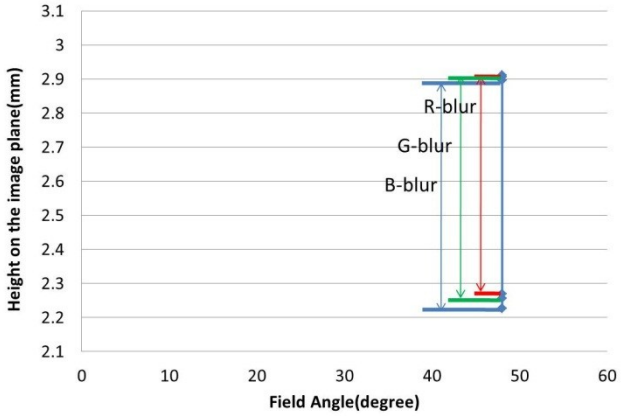

(e) RGB blur before LCA correction at 48 degree

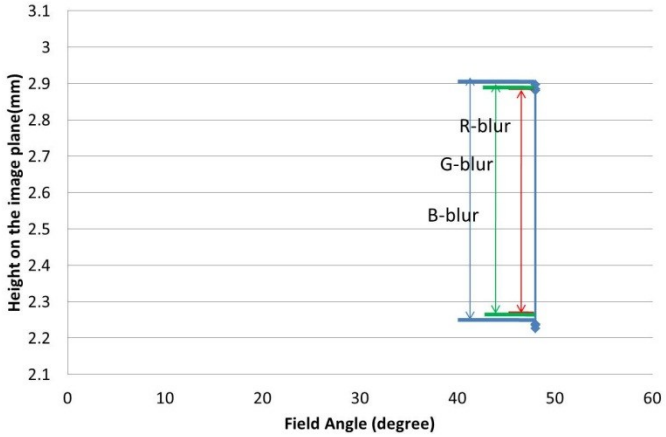

(f) RGB blur after LCA correction at 48 degree

Fig.4.17 RGB blur chart before and after LCA correction

Tab. 4.1 Blur size for R-blur, G-blur and B-blur of three different field angles

	R-blur(mm)	G-blur(mm)	B-blur(mm)
0 degree	0.0132	0.0204	0.0382
26.4 degree	0.1783	0.1861	0.2051
48 degree	0.6424	0.6504	0.6699

In Fig.4.17, R-blur, G-blur and B-blur are measured between image points of upper and lower meridional rays on the image plane for each field angles. Note that the lower meridional ray is higher than upper meridional ray on the image plane because the foci are prior to the image plane, just as shown in Fig.4.15.

It is obvious from Fig.4.15 that the blur caused by field curvature greatly surpass that caused by ACA: the foci of low field angle light beams are closer to the image plane while the foci of high field angle light beams are far from the image plane. This forms more complicated blurring on the image plane. Actually, other optical aberrations like coma, astigmatism all have contribution to the blurring on image plane. In other words, the blurring on the image plane could be considered as a combination of blurring effect contributed by all blur-forming aberrations.

According to Fig.4.17 and Tab.4.1, the blur size for R-blur, G-blur and B-blur at a specific field angle are different as well. B-blur is always greater than R-blur and G-blur for the three field angles. The difference of blur size between G-blur and R-blur for 0, 26.4 and 48 degree are 0.0072 mm, 0.0078mm and 0.0080mm, respectively. While the difference of blur size between B-blur and G-blur for 0, 26.4 and 48 degree are 0.0178mm, 0.0190 mm and 0.0195 mm, respectively. This indicates that the difference between B-blur and G-blur is more than two times the difference between G-blur and R-blur. Therefore, the B-blur is easier to be visible. Although we only showed three charts for three different angles, we can indicate by drawing RGB blur charts that B-blur is always greater than the other two blurs and the difference between B-blur and G-blur is always larger than that between G-blur and R-blur for all field angles. According to Fig.4.17, the position of B-blur center before LCA correction is lower than G-blur and R-blur center for 26.4 and 48 degree, which explains why blue blur can be seen on the inner borders but cannot be seen on the outer borders for images before LCA correction in Fig.4.6 to Fig.4.13. The position of B-blur center after LCA correction has almost been calibrated with G-blur and R-blur center but apparently B-blur is longer than G-blur and R-blur on both sides and the difference between B-blur and G-blur is more than two times the difference between G-blur and R-blur. That explains why the blue blur is still visible and appeared dimmed on both the inner borders and outer borders even if LCA is corrected in corrected images of third order case in Fig.4.6 to Fig.4.13.

Therefore, we can draw a conclusion that LCA correction cannot be eliminated thoroughly if a deblurring process prior to it is not carried out.

In conclusion, we have proved that LCA in Fig.4.5 (b) (which is formed by 2D imaging of the original image Fig.4.5 (a) through the designed single lens) can be successfully corrected, though there is a defect caused by blur.

4.4 Conclusion

In this chapter, improved first order lateral chromatic aberration equation is introduced to deal with lateral chromatic aberration for high field angle single lens. The improved equations use polynomial equation to replace the corresponding term of traditional first order equation in order to make it applicable to high field angles. Simulation results indicate the superiority of the proposed improved equations using higher order polynomial approximation compared to lower order case. Maximum deviation 2.511×10^{-6}mm from the real LCA values between Fraunhofer F line (486.1nm light beams) and C line (656.2 nm light beams) compared to 0.0027 mm by using first order approximation and maximum deviation 2.99×10^{-6}mm from the real LCA values between F line and d line (587.6nm light beams) compared to 0.0019mm by using first order approximation. Visually comparison showed that the third order polynomial approximation yields the most satisfactory corrected images compared to first order approximation. However, the lateral chromatic aberration correction results are influenced by blurring caused by all blur-forming optical aberrations such as axial chromatic aberration and field curvature. This indicates that restoration (also is known as deblurring) should be carried out prior to the correction of lateral chromatic aberration.

4.5 References

[4-1] Kozubek M, Matula P. “An efficient algorithm for measurement and correction of chromatic aberrations in fluorescence microscopy”, Journal of Microscopy; 200(Pt 3): 206-217 (2000)

[4-2] Boult TE, Wolberg G. “Correcting chromatic aberrations using image warping”, Image Understanding Workshop; 363-377 (1992)

[4-3] Kishikawa T. “Kougaku Nyumon”, Optronics Press (1990) (in Japanese)

Chapter 5 Blur restoration for single lens

Chapter 5 Blur restoration for single lens

5.1 Introduction

This chapter is devoted to the blur restoration technique for spherical single lens system. Restoration, also known as deblurring, is a historical problem that has been studied fiercely since decades ago. Not like geometrically distortion or lateral chromatic aberration, the blur effect is caused by inability of the imaging system to focus different objects on an image plane at the same time or relative motion between camera and object when the picture is being taken. A typical example of the former one is defocus: an object near the camera (e.g. people or animal) is sharp and clear while an object far from the camera (e.g. mountain) is blurred. A special case of defocus is radial blur, which is caused by inherent defect of the imaging system such as a single lens. This kind of lens forms sharp regions around the image center but blurred regions when the distance from image plane center increases. Typical examples of the latter type of blur are linear motion blur and rotational motion blur when people move their cameras parallel to the object as they are taking a picture, and another kind of radial blur (because of relative motion) that is occurred when the camera approaches the object at a high speed, and the combination of both parallel and vertical motion. It is well known that mathematically the blur can be simulated by convolving an original aberration-free image with a Point Spread Function (PSF). The inverse process, however, is not that simple. Although it is possible to deblur an image by inverse filters, the deblurred image will be visually unpleasing (because of noise and artifact) if the PSF matrix is not well-regularized or the boundary effect is not eliminated. On the other hand, it is easy to carry out deblurring when both the PSF and blurred image are known to us. For deblurring filters such as wiener filter, Lucy-Richardson filter etc., all PSF is known. However, for most of cases, PSF is unknown. Therefore the blind deconvolution technique was born that deblurs an image by giving an initial guess of the PSF and then adjusting the parameters several times until satisfactory result image is obtained.

In this chapter, a deblurring method to deal with radially variant blurred image created by inherent optical defect of a single lens system will be introduced. Researchers have already studied one kind of radial blur caused by vertical motion between camera and object [5-1] but few have studied on the other kind of radial blur for single lens system. In a Cartesian coordinate system, radially variant blur changes PSF at every pixel position (Fig.5.1 shows the detail, even if the PSFs on some Cartesian pixels have same size and take the same shape, the direction will certainly change), which indicates a Spatially Variant PSF(SVPSF) for everywhere. However, in a polar coordinate system, radially variant blur only changes the PSFs at polar pixels that have different radial distance to the image center. PSFs at polar pixels that have same radial distance to the polar image center can be seen as invariant, that is, they possess same shape, size and direction (Refer to Fig.5.1). PSFs for the whole image then become radially variant but rotationally invariant. The locally invariant PSF can be put into a BTTB (Block Toeplitzs with Toeplitz Blocks) matrix and the deblurring process becomes a linear mathematical system model [5-2]…[5-10]. The spatially variant PSF, however, does not have this property. This reason motivates us to deblur the image using polar coordinate system rather than Cartesian coordinate system.

In Fig.5.1 (a) and (b), the three PSFs are applied to pixels that have same distance to the image center. In a Cartesian coordinate system shown in Fig.5.1 (a), they possess the same size and shape but the direction is different. In a polar coordinate system shown in Fig.5.1 (b), however, they possess the same size, shape and direction. The intersection points in Fig.5.1 (a) and (b) represent Cartesian pixels and polar pixels, respectively. It is easy to find that the PSFs are represented by different pixels

in (a) but same pixels in (b), which indicates that PSFs in (a) are spatially variant and PSFs in (b) are spatially invariant. For pixels that have different distance to image center, both Cartesian PSF and polar PSF become spatially variant.

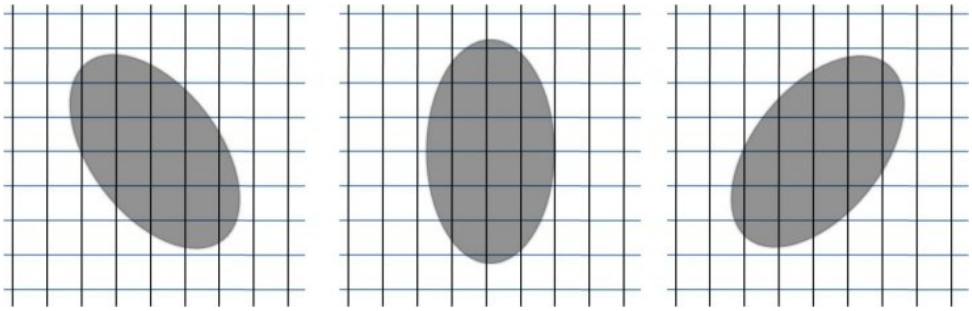

(a) PSFs in Cartesian coordinate system

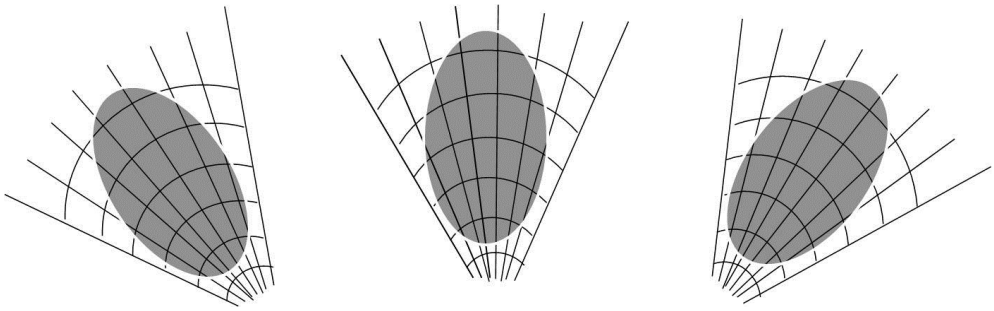

(b) PSFs in Polar coordinate system

Fig.5.1 PSF in Cartesian coordinate system and polar coordinate system for a radially blurred image

5.2 Comparison between Wiener Filter and filter used in this research

A large number of filters have been proposed to solve the deblurring problem [5-11], [5-12]. Generally, there are two categories of filters: linear and nonlinear filters. The former includes generalized inverse filter, constrained least-squares filter, parametric Wiener filter, geometrical mean filters, maximum entropy filter and pseudo-inverse filter. The latter, however, is not popular compared to the former because it requires costly computational procedure. Additionally, all nonlinear filters employ the iterative algorithm [5-12]. The detailed introduction of this category can be found in Chapter 9 of [5-11] so that we leave this part to readers who are interested in it.

Among all the linear filters, the most famous is Wiener Filter, whose general matrix form expression is as follows [5-11]:

$$\text{Wiener Filter} = \left([H]^{*t}[H] + [\phi_f]^{-1}[\phi_n]\right)^{-1}[H]^{*t} \tag{5.1}$$

where $[H]$ represents matrix of the point spread function(PSF) and $[\phi_f]$, $[\phi_n]$ are the signal and noise covariance matrices, respectively. The notation "$*t$" indicates conjugate transpose.

It should be noted that Wiener filter is also a constrained least-squares filter, whose general form is

$$([H]^{*t}[H] + \gamma[Q]^{*t}[Q])^{-1}[H]^{*t} \tag{5.2}$$

where γ is a reciprocal Lagrangian multiplier and $[Q]$ indicates linear operator. For Wiener filter, $\gamma = 1$ and $[Q]=[\phi_f]^{-1/2}[\phi_n]^{1/2}$.

The deblurring in this research used another type of constrained least-squares filter, which is simple to be implemented. It defines the linear operator as an identity matrix, that is $[Q]=[I]$ so that the filter

becomes

$$\text{Deblurring filter in this research} = ([H]^{*t}[H] + \gamma[I])^{-1}[H]^{*t} \quad (5.3)$$

This expression is also called Tikhonov Regularization, which is used to avoid singularity or ill-conditioning of the PSF matrix. In the definition of Tikhonov Regularization, γ is the regularization parameter and $[Q]$ is the regularization operator.

5.3 Methods

5.3.1 Radially variant PSFs

In this section, the radially variant PSF will be introduced. The radially variant PSF is formed by the single lens imaging system, illustrated in Fig.5.2.

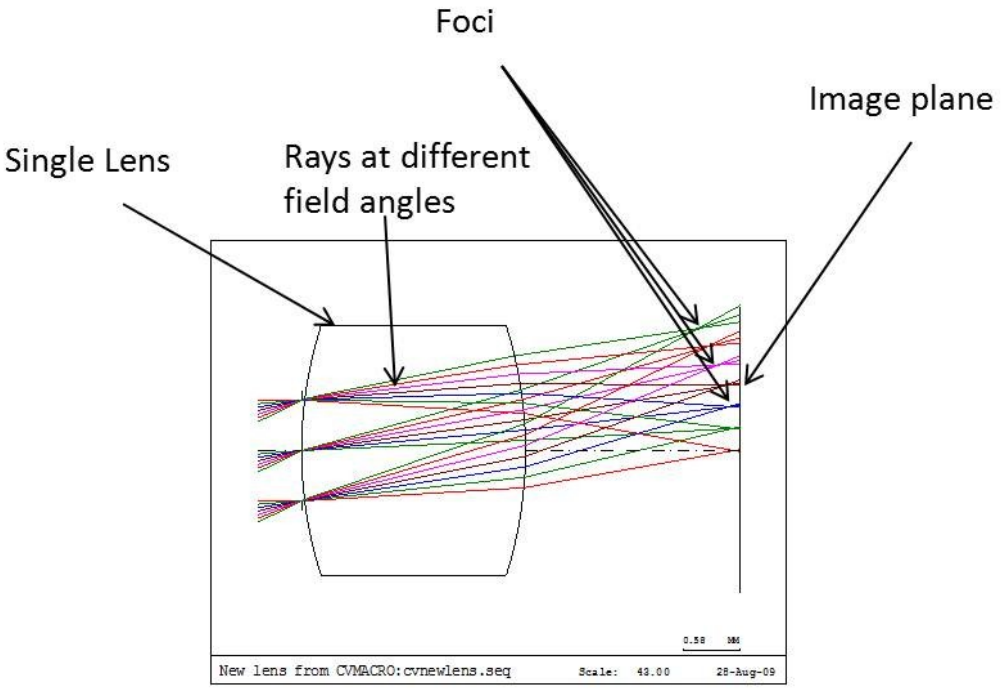

Fig.5.2 Single lens imaging system

Because of single lens property, stronger optical aberration will occur at high field angles than low field angles. For example, as shown in Fig.5.2, when field curvature (the foci deviates more and more from the image plane as the field angle increases, forming a curved shape) becomes stronger and stronger as the field angle increases, strong blur occur at high field in the resulting image. As a result, a normal image will become a visually blurred image after the single lens system. Fig.5.3 shows an original gray scale image and the resulting image created by the designed single lens imaging system (highest field angle is 21 degree).

(a) A visually normal image (b) resulting image

Fig.5.3 An original image and the resulting distorted and blurred image created by the single lens imaging system

From Fig.5.3 (b) we noticed that the four corners (high field angle) in the resulting image blurred strongly, whereas the central part is almost sharp. This attributes to the fact that the PSF varies as the field angle varies. We have examined some sample PSFs of our single lens system, shown in Fig.5.4.

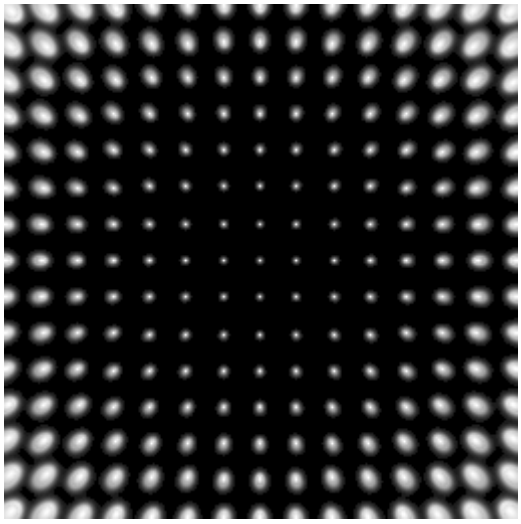

Fig.5.4 Radially variant PSF (15 sample PSFs in both horizontal and vertical directions.)

The PSFs shown in Fig. 5.4 only have 15 samples along horizontal and vertical directions. In the real imaging process, the original image not only convolves with sample PSFs but also a lot of PSFs that are in between sample PSFs. Those PSFs between the sample PSFs are interpolated.

5.3.2 Image conversion between Cartesian coordinate system and polar coordinate system

Because of the characteristic of the radially variant PSF, image deblurring can be much easier carried out on polar coordinate system than Cartesian coordinate system.

In this section, the algorithm to convert image from Cartesian coordinate system to polar coordinate system and the inverse conversion will be introduced.

The Cartesian coordinate system is illustrated in Fig.5.5, where each node is considered as one Cartesian pixel.

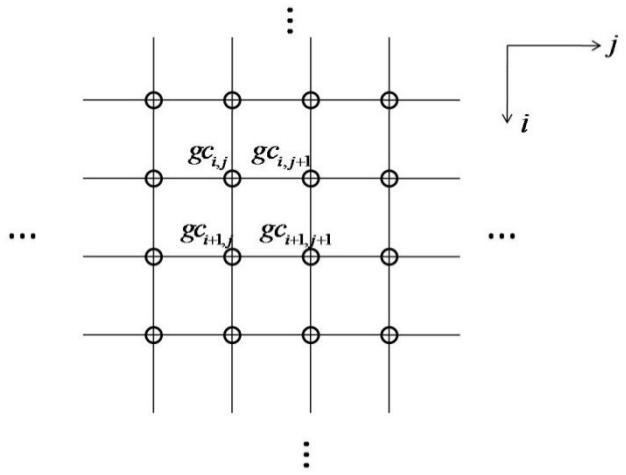

Fig.5.5 Cartesian coordinate system

In Fig.5.5, $gc_{i,j}$ represents a Cartesian pixel of the blurred and distorted image, i,j is the pixel index.

The origin of the Cartesian coordinate system is located at the top-left corner, and its coordinate is (1,1). (Note that unlike other coordinate system that has (0,0) origin, the origin in our research is (1,1) because the pixel index should be positive integers for digital image.) In addition, the pixel index is in matrix index order as well, by which the 2D digital image can be easily transferred to a matrix form:

$$\begin{pmatrix} gc_{1,1} & \cdots & gc_{1,n} \\ \vdots & \ddots & \vdots \\ gc_{m,1} & \cdots & gc_{m,n} \end{pmatrix}$$

Similarly, the polar coordinate system is illustrated in Fig.5.6, where each node is considered as one polar pixel. (Only 4 nodes are drawn in Fig.5.6 for simplicity.)

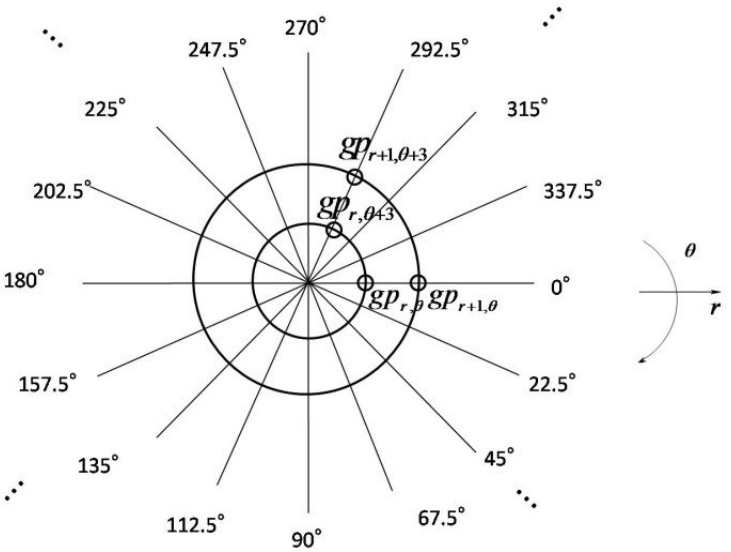

Fig.5.6 Polar coordinate system

In Fig.5.6, $gp_{r,\theta}$ indicates a polar pixel of the blurred and distorted image, r,θ is the pixel index. Both r and θ should be positive integers. Therefore, the origin of the polar coordinate system is also (1,1). The index r increases radially from the polar coordinate system center. The index θ increases clockwise from 0 to 360 degree. The maximum θ is determined by the number of equal parts that the whole circle (360 degree) is divided. In Fig.5.6, the whole circle is divided into 16 equal parts. Therefore, the maximum θ is 16. The equation for degree and index conversion is

$$\theta = \frac{\text{No.of equal parts} \times \text{degrees}}{360} + 1$$

For example, 0 degree corresponds to $\theta = 1$, 135 degree corresponds to $\theta = 7$, etc. The indices of the polar coordinate system can also be transferred to matrix form:

$$\begin{pmatrix} gp_{1,1} & \cdots & gp_{1,\xi} \\ \vdots & \ddots & \vdots \\ gp_{\rho,1} & \cdots & gp_{\rho,\xi} \end{pmatrix}$$

In this matrix, each row represents polar pixels that have same r. And each column represents polar pixels that have same θ. It should be emphasized that all polar pixels in the first row of the matrix are positioned on the polar coordinate grid center. Therefore, there are totally ξ pixels on the center, and the pixel value are equal to the origin of the polar coordinate system: $gp_{1,1} = gp_{1,2} = \cdots = gp_{1,\xi}$.

To convert Cartesian coordinate system to polar coordinate system, the two coordinate systems should be overlapped with each other. The Cartesian coordinate system center is also the polar coordinate system center. For simplicity, we give a 4×4 resolution image to introduce the coordinate conversion algorithm.

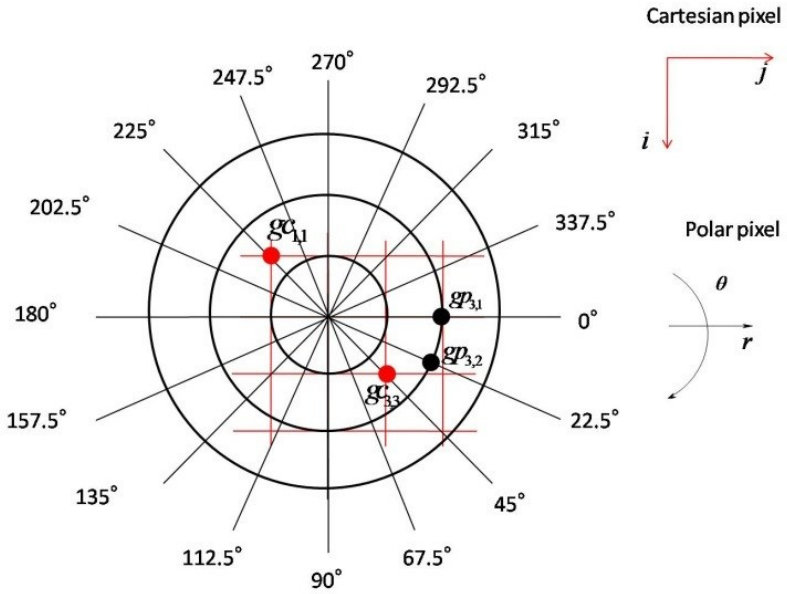

Fig.5.7 Cartesian coordinate system and polar coordinate system conversion

Firstly, the equations that convert Cartesian coordinate system to polar coordinate system are taking the following form:

$$r = \sqrt{(i - i_c)^2 + (j - j_c)^2} + 1 \tag{5.4}$$

$$\theta = \frac{q}{360} \arctan \frac{i - i_c}{j - j_c} + 1 \tag{5.5}$$

where i_c, j_c indicate image center of the Cartesian coordinate system and q is the number of equal parts that the whole circle (360 degree) of the polar coordinate system is divided. Note that the indices of the Cartesian coordinate system center of the 4×4 image are (2, 2) but not (2.5, 2.5) because the index should be positive integers.

The rules to build a polar coordinate system on a Cartesian coordinate system are that the polar coordinate system should not smaller than Cartesian coordinate system in size. It should encircle the whole Cartesian coordinate system. This can be done by obtaining maximum r from equation (5.4) by substituting maximum value of the index i and j and round off to the nearest larger integer. For example, in Fig.5.7, $i_{\max} = 4, j_{\max} = 4$ and $i_c = 2, j_c = 2$ therefore, $r_{\max}$=3.8284≈ 4.

The determination of $\theta_{\max}$ or q (number of equal parts) is:

1) $\theta_{\max}$ equals to q. q should be a number that can be divided exactly by 4. This is convenient because the imported PSFs from optical design software are generated for the 270 radial line. If q does not satisfy this condition, there will be no radial line that the 270 degree PSFs can be applied to. Therefore a transfer from 270 degree PSFs to PSFs of other angles is necessary, which is an undesirable and unnecessary task.

2) Within the Cartesian coordinate system region, there should be at least one polar pixel surrounded by four Cartesian pixels, especially when r reaches high value.

Note that $\theta_{\max}$ cannot be calculated directly from (5.5) by substituting the Cartesian pixel (*i,j*) that is located in the upper half polar circle and near the polar pixel (r_{max}, 1) into (5.5). For example, in Fig.5.7, when the polar coordinate grid is divided finer in the direction of θ, (e.g. q=32), substituting Cartesian pixel (1,4) will result in $\theta = 31$.

When r_{max} and θ_{max} are determined, the polar coordinate system can be built. The next step is to obtain the polar pixel value. This can be done by interpolating from the surrounded Cartesian pixels (Refer to Fig.5.8). Before carrying out the interpolation, the inverse conversion (polar coordinate system to Cartesian coordinate system) is necessary because the interpolation process needs Cartesian pixel indices. The equations of the inverse conversion can be derived directly from (5.4) and (5.5):

$$i = (r-1) \bullet \sin \frac{360 \bullet (\theta - 1)}{q} + i_c \tag{5.6}$$

$$j = (r-1) \bullet \cos \frac{360 \bullet (\theta - 1)}{q} + j_c \tag{5.7}$$

In equation (5.6) and (5.7), each polar pixel index ($r;\theta$) is integer and the obtained Cartesian pixel index (*i,j*) is decimal. Then each decimal Cartesian pixel value is obtained by bilinear interpolation from the surrounding 4 integer Cartesian pixels. Since the decimal Cartesian pixel is the same point as the integer polar pixel, the pixel value is same as well.

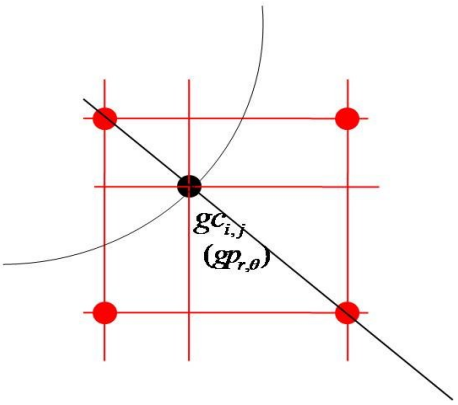

Fig.5.8 Obtain the polar pixel value by bilinear interpolation from the surrounded four integer Cartesian pixels

On the other hand, conversion from Cartesian image to polar image will create an extra region that does not belong to the Cartesian image. Fig.5.9 and Fig.5.10 show some blurred Cartesian images created by the designed single lens imaging system and the panorama of the corresponding blurred polar images. The polar pixels of the blurred polar image that are located outside Cartesian image region (we call it exterior Cartesian image region, hence there also exists interior Cartesian image region) has to be considered too. In some cases, these pixels' value cannot be treated as zero. When the transition between interior and exterior original aberration-free Cartesian image region involves an obvious sharp intensity drop, the exterior region of the blurred polar image should not be considered zeros, otherwise it will lose some pixel information so that not accurately represent the actual polar blurred image. This problem will be further explained in Section 5.4.

Blurred Cartesian image

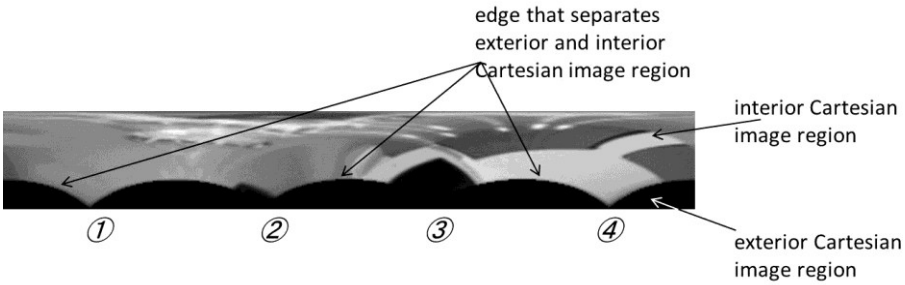

Panorama of the blurred polar image

Fig. 5.9 Blurred Cartesian image and panoramic blurred polar image

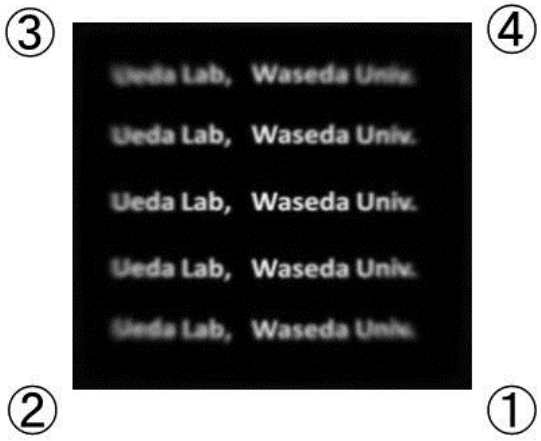

Blurred Cartesian image

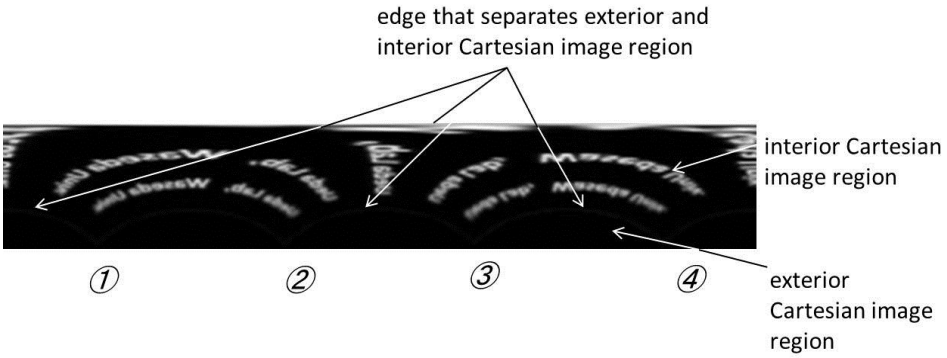

Panorama of the blurred polar image

Fig.5.10 Blurred Cartesian image and panoramic blurred polar image

In Fig.5.9, the edges that connect exterior Cartesian image region and interior Cartesian image region have sharp pixel intensity drop. However, Fig.5.10 does not show sharp intensity drop on the edges. In this case, the exterior Cartesian image region may be treated as zeros. We also marked four corners of the Cartesian image by numbers and corresponding positions in the panoramic polar images in Fig.5.9 and Fig.5.10.

It should be mentioned that at the final step of the deblurring process, the bilinear interpolation is necessary again in order to obtain Cartesian pixel values from the surrounded 4 integer polar pixels. This is similar to obtaining the polar pixel values from integer Cartesian pixels.

5.3.3 PSF conversion between Cartesian coordinate system and polar coordinate system

As is mentioned in Section 5.1 and 5.3.1, the PSF is radially variant but rotationally invariant in the polar coordinate system, therefore, it is easy to implement image deblurring on polar coordinate system. This necessitates not only the blurred image but also PSF in polar coordinate grid. In this section, PSF conversion from Cartesian coordinate system to polar coordinate system and the inverse conversion will be introduced.

The following figure gives two kinds of PSF for PSF conversion between Cartesian coordinate system and polar coordinate system:

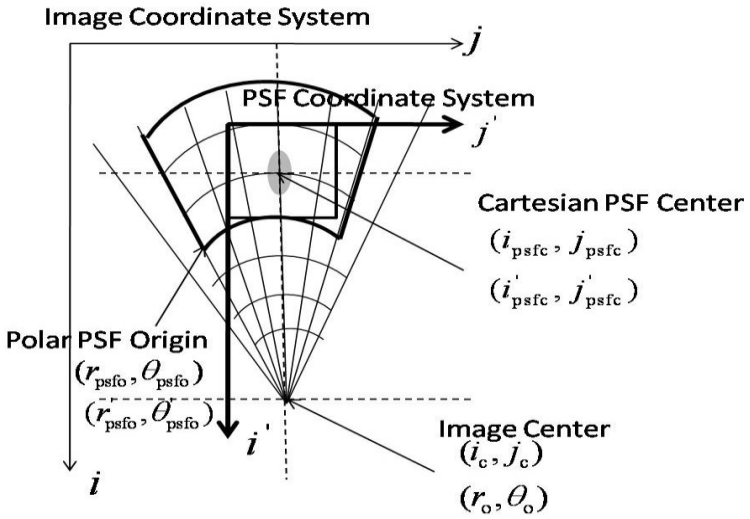

(a) The first kind of PSF

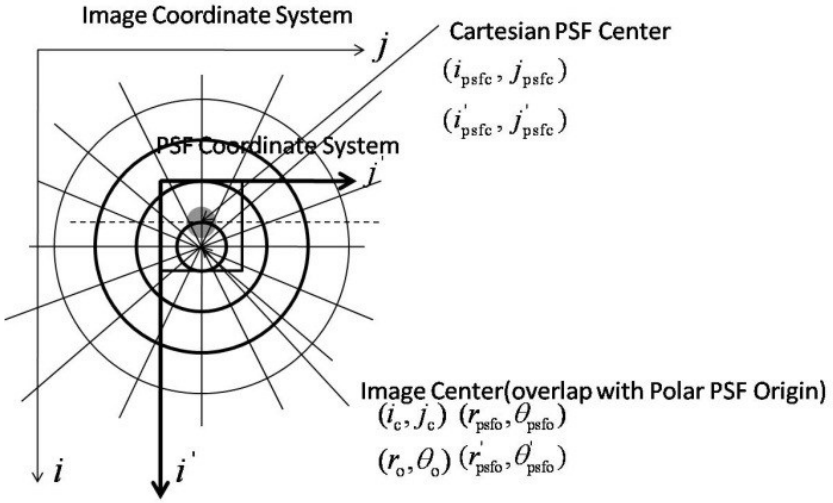

(b) The second kind of PSF

Fig.5.11 Two kinds of PSF for PSF conversion between Cartesian coordinate system and polar coordinate system

In Fig.5.11, the bolded square area represents Cartesian PSF and the bolded sectorial or circled area represents polar PSF. For the first kind: Image center is located outside Cartesian PSF or on the border of Cartesian PSF. As to the second kind: Image center is located inside Cartesian PSF. The rules to convert PSF from Cartesian coordinate to polar coordinate are as follows: The converted polar PSF should be on the same polar coordinate system as the polar image. The size and position of the polar PSF is determined by Cartesian PSF, the polar PSF should encircle the whole Cartesian PSF. The origin of the polar PSF is not necessarily on the image center (unless it is the second kind of PSF) and also not necessarily on Cartesian PSF center (unless Cartesian PSF center overlap with the image center).

The PSF conversion from Cartesian coordinate system to polar coordinate system can be achieved by equation (5.8) and (5.9).

$$r' = \sqrt{(i' + i_{\text{psfc}} - i'_{\text{psfc}} - i_{\text{c}})^2 + (j' + j_{\text{psfc}} - j'_{\text{psfc}} - j_{\text{c}})^2} + 1 - r_{\text{psfo}} + r'_{\text{psfo}} \tag{5.8}$$

$$\theta' = \frac{q}{360} \arctan \frac{i' + i_{\text{psfc}} - i'_{\text{psfc}} - i_{\text{c}}}{j' + j_{\text{psfc}} - j'_{\text{psfc}} - j_{\text{c}}} + 1 - \theta_{\text{psfo}} + \theta'_{\text{psfo}} \tag{5.9}$$

The dashed index indicates PSF coordinate system that is shifted from the image coordinate system (Fig.5.11).

The meaning of each notation is as follows:

r', θ': polar image index on PSF coordinate system

i', j': Cartesian image index on PSF coordinate system

$r_{\text{psfo}}, \theta_{\text{psfo}}$: index of polar PSF origin on image coordinate system

$r'_{\text{psfo}}, \theta'_{\text{psfo}}$: index of polar PSF origin on PSF coordinate system

$i_{\text{psfc}}, j_{\text{psfc}}$: index of Cartesian PSF center on image coordinate system

$i'_{\text{psfc}}, j'_{\text{psfc}}$: index of Cartesian PSF center on PSF coordinate system

$r_{\text{o}}, \theta_{\text{o}}$: index of polar image origin on image coordinate system

$i_{\text{c}}, j_{\text{c}}$: index of Cartesian image center on image coordinate system

Equation (5.8) and (5.9) can be derived by the following two steps:

Step 1: Transfer the image coordinate system to PSF coordinate system

Suppose there is a Cartesian pixel (*i,j*) in image coordinate system, its corresponding Cartesian index on PSF coordinate system is i', j':

According to Fig.5.11, we have

$$i' = i'_{\text{psfc}} + (i_c - i_{\text{psfc}}) - (i_c - i) \Rightarrow$$

$$i' = i - i_{\text{psfc}} + i'_{\text{psfc}} \tag{5.10}$$

$$j' = j'_{\text{psfc}} + (j_c - j_{\text{psfc}}) - (j_c - j) \Rightarrow$$

$$j' = j - j_{\text{psfc}} + j'_{\text{psfc}} \tag{5.11}$$

Similarly, suppose there is a polar pixel (r, θ) in image coordinate system, its corresponding polar index on PSF coordinate system is r', θ':

Then from Fig.5.11 we have

$$r' = r'_{\text{psfo}} + (r - r_o) - (r_{\text{psfo}} - r_o) \Rightarrow$$

$$r' = r - r_{\text{psfo}} + r'_{\text{psfo}} \tag{5.12}$$

$$\theta' = \theta'_{\text{psfo}} + (\theta - \theta_o) - (\theta_{\text{psfo}} - \theta_o) \Rightarrow$$

$$\theta' = \theta - \theta_{\text{psfo}} + \theta'_{\text{psfo}} \tag{5.13}$$

Step 2: Substitute (5.4), (5.5), (5.10) and (5.11) into (5.12) and (5.13)

$$\begin{aligned} r' &= r - r_{\text{psfo}} + r'_{\text{psfo}} \\ &= \sqrt{(i-i_c)^2 + (j-j_c)^2} + 1 - r_{\text{psfo}} + r'_{\text{psfo}} \\ &= \sqrt{(i' + i_{\text{psfc}} - i'_{\text{psfc}} - i_c)^2 + (j' + j_{\text{psfc}} - j'_{\text{psfc}} - j_c)^2} + 1 - r_{\text{psfo}} + r'_{\text{psfo}} \end{aligned}$$

$$\begin{aligned} \theta' &= \theta - \theta_{\text{psfo}} + \theta'_{\text{psfo}} \\ &= \frac{q}{360} \arctan \frac{i-i_c}{j-j_c} + 1 - \theta_{\text{psfo}} + \theta'_{\text{psfo}} \\ &= \frac{q}{360} \arctan \frac{i' + i_{\text{psfc}} - i'_{\text{psfc}} - i_c}{j' + j_{\text{psfc}} - j'_{\text{psfc}} - j_c} + 1 - \theta_{\text{psfo}} + \theta'_{\text{psfo}} \end{aligned}$$

which are exactly equation (5.8) and (5.9).

When r', θ' are obtained, the next step is to obtain the polar PSF pixel values by interpolation from Cartesian PSF pixels. This is similar to interpolate polar image pixels from Cartesian image pixels so we neglect detailed description. The inverse conversion from polar coordinate system to Cartesian coordinate system is necessary before the interpolation, which is expressed in (5.14) and (5.15).

$$i' = (r' - 1 + r_{\text{psfo}} - r'_{\text{psfo}}) \bullet \sin \frac{360(\theta' - 1 + \theta_{\text{psfo}} - \theta'_{\text{psfo}})}{q} + i_{\text{c}} - i_{\text{psfc}} + i'_{\text{psfc}} \tag{5.14}$$

$$j' = (r' - 1 + r_{\text{psfo}} - r'_{\text{psfo}}) \bullet \cos \frac{360(\theta' - 1 + \theta_{\text{psfo}} - \theta'_{\text{psfo}})}{q} + j_{\text{c}} - j_{\text{psfc}} + j'_{\text{psfc}} \tag{5.15}$$

5.3.4 Comparison between traditional BTTB structure and the special BTCB structure of PSF matrix

Before introducing image deblurring, it is necessary to introduce image blurring, which is the convolution between PSF and the original image. The matrix form of blurring an image without considering noise can be expressed in (5.16):

$$\mathbf{G} = \mathbf{T} \bullet \mathbf{F} \tag{5.16}$$

In expression (5.16), **T** represents PSF matrix, **F** represents original image column vector and **G** is the blurred image column vector. For spatially invariant (SI) PSF, **T** is a BTTB (Block Toeplitz with Toeplitz Blocks) matrix. The following paragraph explains the reason why the structure is a BTTB. For spatially variant (SV) PSF, the BTTB structure will break. However, the SV PSF can be treated as locally SI PSF.

The following figure explains convolution between PSF and the original image.

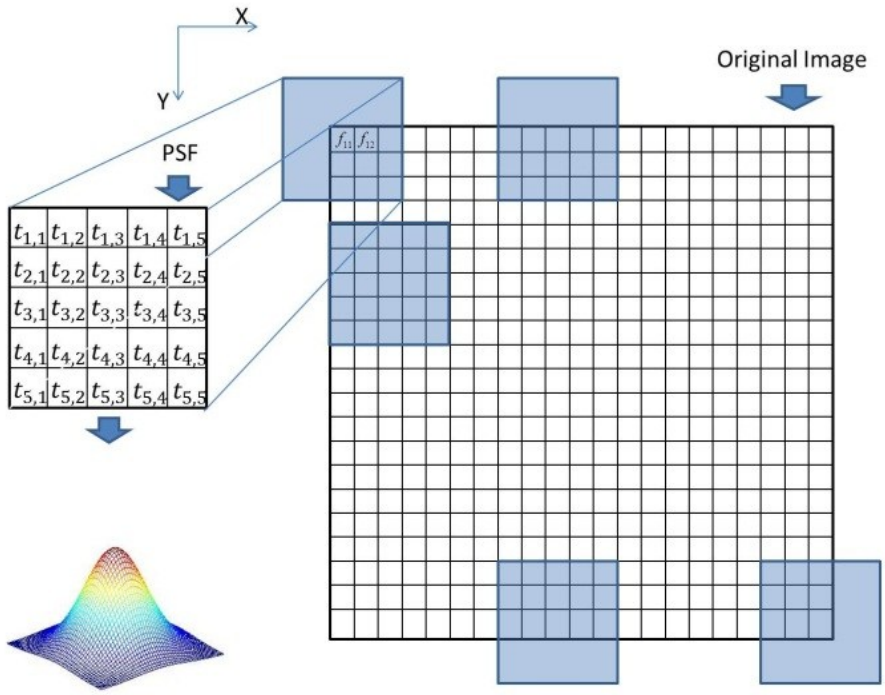

Fig.5.12 Convolution between PSF and the original image

In Fig.5.12, each pixel of the blurred image is obtained by weighted average of pixels of the original image, where the weights are elements (pixels) of the PSF:

$$\begin{cases} g_{i,j} = \dfrac{\sum_{a=1}^{m}\sum_{b=1}^{n} t_{a-i+i'_{\text{psfc}},\,b-j+j'_{\text{psfc}}} f_{a,b}}{S} (i=1\sim m, j=1\sim n) \\ S = \sum_{i'_{\text{psf}}=1}^{P}\sum_{j'_{\text{psf}}=1}^{Q} t_{i'_{\text{psf}},j'_{\text{psf}}} \end{cases} \tag{5.17}$$

where *a,b* are pixel index of the original image, *i,j* are pixel index of the blurred image, i'_{psf} , j'_{psf} is index of the PSF. *m,n* and *P,Q* are maximum pixel index of the original, blurred image and PSF, respectively. i'_{psfc} and j'_{psfc} represent center index of the PSF. In the numerator of equation (5.17), *t* serves as weight for each pixel of the original image, *S* means summation of all pixels of the PSF. Expanding equation (5.17) :

$$g_{i,j} = \frac{t_{1-i+i'_{\text{psfc}},1-j+j'_{\text{psfc}}}}{S} f_{1,1} + \frac{t_{1-i+i'_{\text{psfc}},2-j+j'_{\text{psfc}}}}{S} f_{1,2} + \ldots + \frac{t_{m-i+i'_{\text{psfc}},n-j+j'_{\text{psfc}}}}{S} f_{m,n} \tag{5.18}$$

We found that each $\dfrac{t_{a-i+i'_{\text{psfc}},\ b-j+j'_{\text{psfc}}}}{S}$ in (5.18) indicates normalization of the PSF pixel. That is, summation of all pixels of the normalized PSF equals to 1.

For Gaussian shaped PSF, the PSF center element $t_{i'_{\text{psfc}},j'_{\text{psfc}}}$ is always the summit of the PSF. To obtain $g_{i,j}$, the position of $t_{i'_{\text{psfc}},j'_{\text{psfc}}}$ must overlaps with $f_{i,j}$ when carrying out the convolution.

1) Traditional BTTB structure of spatially invariant PSF matrix

If we express the convolution in matrix form, we have Fig.5.13 and Fig.5.14. For simplicity, the

PSF size in Fig.5.12 is 5×5, the maximum pixel index of the original image satisfies $m = n$.

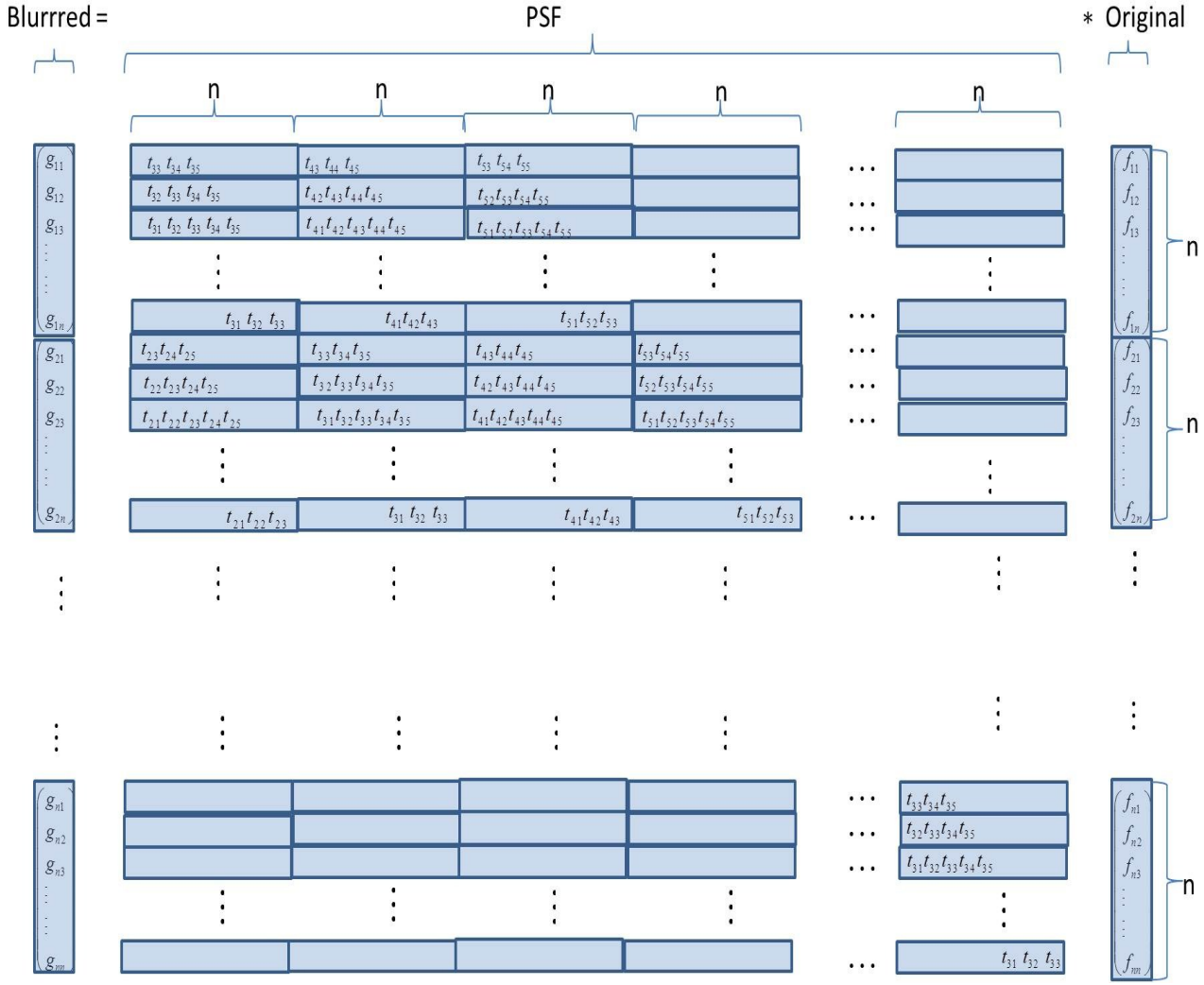

Fig.5.13 Matrix form of image blurring for spatially invariant PSF

$$\begin{pmatrix} G_1 \\ G_2 \\ G_3 \\ \vdots \\ \vdots \\ \vdots \\ G_n \end{pmatrix} = \begin{pmatrix} T_{11} & T_{12} & T_{13} & & & & \\ T_{21} & T_{11} & T_{12} & T_{13} & & & \\ T_{31} & T_{21} & T_{11} & T_{12} & T_{13} & & \\ & \ddots & \ddots & \ddots & & & \\ & & \ddots & \ddots & \ddots & & \\ & & & T_{31} & T_{21} & T_{11} & T_{12} & T_{13} \\ & & & & T_{31} & T_{21} & T_{11} & T_{12} \\ & & & & & T_{31} & T_{21} & T_{11} \end{pmatrix} \bullet \begin{pmatrix} F_1 \\ F_2 \\ F_3 \\ \vdots \\ \vdots \\ \vdots \\ F_n \end{pmatrix}$$

Fig.5.14 Simplified version of Fig.5.13

From Fig.5.13 and Fig.5.14 we know that row elements (pixels) of the original image are stacked to column vector F_i(i = 1~n) so that F_i includes elements of the *i*th row of the original image. Similarly, G_i(i = 1~n)means column vector of the blurred image. G_i includes elements of the *i*th

row of the blurred image. In Fig.5.13, each $n \times n$ block in the PSF matrix is a Toeplitz block (TB), which is represented by T in Fig.5.14. The whole Toeplitz blocks in Fig.5.14 also take the form of Toeplitz matrix, which can be called block Toeplitz (BT). Therefore, for SI case, the PSF is a BTTB matrix.

According to Fig.5.12, it is easy to observe that pixels along the image boundaries are obtained by convolving less PSF elements (not all PSF elements) than pixels of inner image. These pixels are called boundary pixels. For example, only 9 PSF elements (not 25 elements): $t_{33}, t_{34}, t_{35}, t_{43}, t_{44}, t_{45}, t_{53}, t_{54}, t_{55}$ are available to obtain g_{11}. This is also observable from the first row of PSF matrix in Fig.5.13. In general, the number of PSF elements in each Toeplitz block T is controlled by the following rule: the number of PSF elements to be convolved increases as the PSF "enters" the image from the left boundary and stop increasing when the PSF "enters" the image completely along X-direction. Then it decreases again as the PSF "leaves" from the right boundary of the image. Take the first Toeplitz block T_{11} for example, the number of PSF elements along X-direction is 5. The number of PSF elements increases from 3 (first row of the PSF matrix) to 5(third row of the PSF matrix) and then stop increasing, because all 5 pixels along X-direction "entered" image from the left boundary. Then it decreases from the (n-1) th row. Finally, the number of PSF elements to be convolved in X-direction returns to 3 at the nth row of PSF matrix. Similar rule can be found on BT in Fig.5.14. The number of TBs increases continuously from 3(first row) to 5(third row) and then stop increasing, which means PSF "enters" the image from the upper boundary until it "enters" the image completely in Y-direction. Then the number of T decreases from the (n-1) th row until the number returns to 3 at the nth row, which indicates PSF "leaves" from the lower boundary of the image. A property that is common for both TBs and BT is that the elements are always distributed around the matrix diagonal.

2) BTCB structure of radially variant PSF matrix in this study

Now, let us examine the structure of radially variant PSF matrix in this study. Fig.5.15 illustrates the convolution between original polar image and polar PSF. Fig.5.16 is the panorama of Fig.5.15. Fig.5.17 shows the simplified matrix form of image blurring for radially variant PSF. Fig.5.18 gives the first Toeplitz block T_{11} of Fig.5.17.

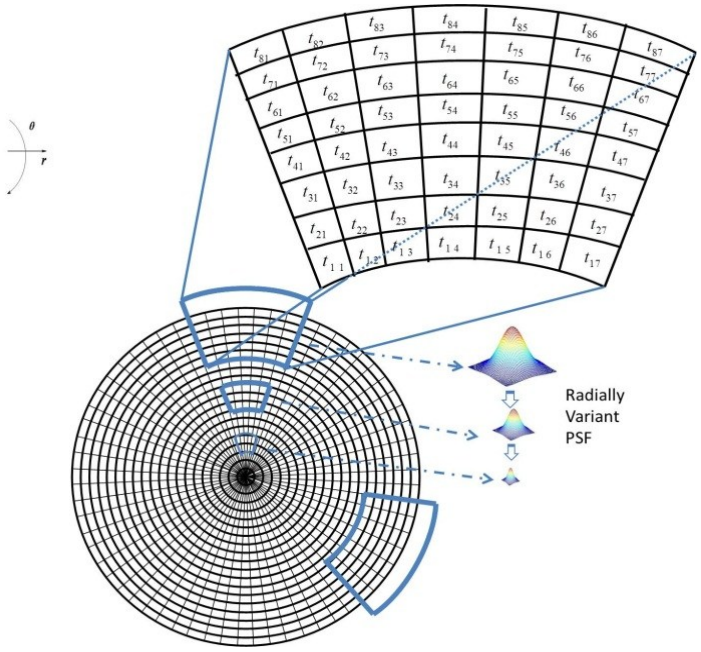

Fig. 5.15 Convolution between original polar image and polar PSF

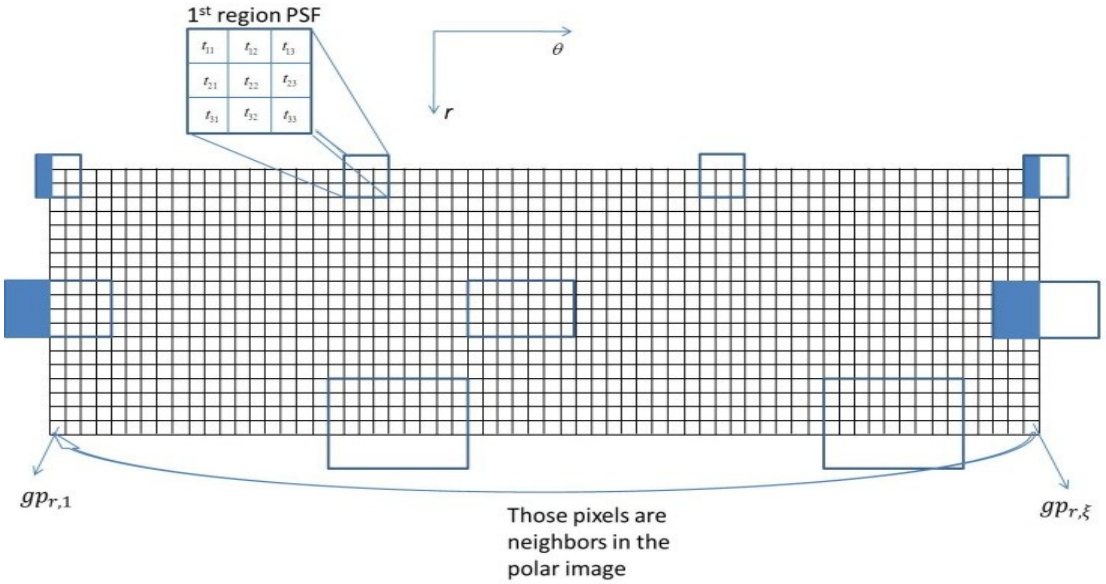

Fig. 5.16 Panorama of the convolution shown in Fig.5.15

$$\begin{pmatrix} G_1 \\ G_2 \\ G_3 \\ \vdots \\ G_\rho \end{pmatrix} = \begin{pmatrix} T_{11} & T_{12} & & & & \\ T_{21} & T_{22} & T_{23} & T_{24} & & \\ T_{31} & T_{32} & T_{33} & T_{34} & T_{35} & \\ & \ddots & \ddots & \ddots & \ddots & \\ & & \ddots & \ddots & \ddots & \ddots \\ & & & \ddots & \ddots & \ddots \\ & & & & \ddots & \ddots \\ & & & & & T_{\rho\rho} \end{pmatrix} \bullet \begin{pmatrix} F_1 \\ F_2 \\ F_3 \\ \vdots \\ F_\rho \end{pmatrix}$$

Fig.5.17 Simplified matrix form of image blurring for radially variant PSF

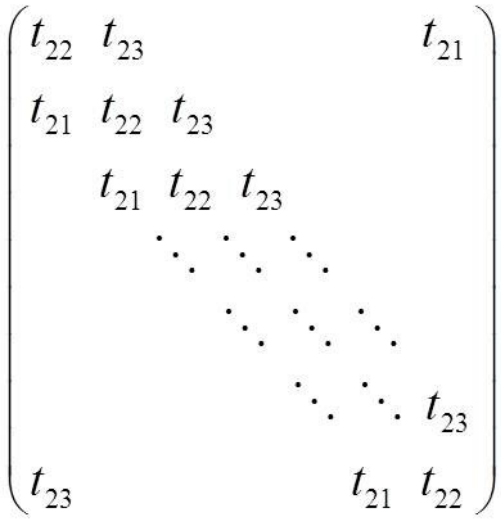

Fig.5.18 First Toeplitz block T_{11} of Fig.5.17

The bolded sectorial and square areas in Fig.5.15 and Fig.5.16 represent polar PSFs. The polar image origin (center pixel) of Fig.5.15 corresponds to pixels of the first row in Fig.5.16. From Fig.5.15 and Fig.5.16 we can observe that the size of polar PSF expands as the radial distance from the polar image origin increases but does not change as θ increases. For radially variant PSF matrix shown in Fig.5.17, the number of Toeplitz Blocks (TBs) changes at each row, even if the polar PSF "enters" the polar image completely. When the PSF becomes larger in size as *r* increases, the number of TBs also increases from the first row, and continue increasing when PSF "enters" the image completely. This is different from spatially invariant PSFs. Then it decreases when PSF "leaves" from the lower boundary. The bigger the size of PSF at a certain radial distance from image center, the greater the number of TBs at certain row of PSF matrix in Fig.5.17. As pixels at different rows of the panoramic polar image are obtained by convolving different PSFs, the elements in TBs at different rows of PSF matrix shown in Fig.5.17 belong to different PSFs. However, elements in TBs at same row belong to same PSF. For example, elements in T_{11}, T_{12} belong to PSF which is applied to the first row of panoramic polar image, elements in $T_{21}, T_{22}, T_{23}, T_{24}$ belong to PSF which is applied to the 2nd row of panoramic polar image, etc. As a result, the whole TBs in Fig.5.17 will not take the form of Toeplitz matrix any more. In other words, it is not a Block Toeplitz(BT). In this case, a method to treat the PSF as locally invariant (PSF is invariant at some rows of the panoramic polar image) is available. This approach has been studied by predecessors before, which is to divide the image into several regions, each region has its corresponding locally invariant PSF. This method is actually the piecewise approximation of real PSF. As to our polar image case, the PSF at each region will become a BTCB matrix (Block Toeplitz with Circulant Blocks). This is easy to observe from Fig.5.16 and Fig.5.18: Assume the first *n* ($n<\rho$) rows of the panoramic polar image belong to region 1, whose spatially invariant PSF is shown in Fig.5.16. Allow us to name it the first region PSF. The size of the first region PSF is 3×3. Note that Fig.5.16 only shows the convolution between the first region PSF and the first row. The pixels at far right $(gp_{r,\xi})$ of the panorama are neighbouring pixels of those at far left $(gp_{r,1})$ because the original image shown in Fig.5.15 is a polar image. Thus, although the shaded area of PSF at the left boundary convolves with no panoramic polar image pixels, it convolves with pixels at the right boundary. Therefore, the pixels of the first row of panoramic polar image that are convolved with the shaded area of the first region PSF correspond to element t_{21} at the top right corner of T_{11} matirx in Fig.5.18. Similarly, we can predict that another element t_{23} is located at the lower left corner (the shaded area is not shown in Fig.5.16). By observing matrix structure of Fig.5.18, we found that it is a special kind of Toeplitz matrix: Circulant matrix. As the elements as a whole in each TB of a spatially invariant PSF region also takes the form of circulant

matrix, and the whole Circulant Blocks(CB) in each region takes the form of Toeplitz matrix, we can call it BTCB(Block Toeplitz with Circulant Blocks) matrix.

5.3.5 Deblurring of the radially variant blurred image

The image deblurring is realized by deconvolution using polar image and polar PSFs obtained in 5.3.2 and 5.3.3. As is mentioned before, this is a locally spatially invariant (SI) PSF problem. SI deblurring is a famous linear mathematical system problem that involves a BTTB (Block Toeplitz with Toeplitz Blocks) matrix which is the PSF and a column vector which includes the matrix elements of the blurred image. In our case, the locally invariant PSFs becomes a BTCB (Block Toeplitz with Circulant Blocks) matrix because the pixels at the far left of the panoramaic polar image are neighboring pixels of those at the far right. During the deblurring process, fast algorithm using FFT and component-wise multiplication for padded BCCB (Block Circulant with Circulant Blocks) matrix is used to simplify the calculation. In addition, the deblurring is also an ill-posed problem and the Tikhonov Regularization is to be used to deal with it. The deblurring is realized using constrained least-squares method introduced in Section 5.2 and the linear operator is an identity matrix. This method is a non-iterative method which means the deblurring can be realized in just one step. More details about BTTB and BCCB, Tikhonov Regularization and constrained least-squares method can be found in [5-2] to [5-12].

Note that there are two deblurring methods implemented in this study: 1) debluring by applying SIPSF to sub-regions and then sewing the sub-restored regions together; 2) deblurring by applying SIPSF to whole image, preserving the well-restored regions and removing the unsatisfied restored regions, then sewing the sub-restored regions together. The difference is as follows: method 1) has to eliminate the boundary ringing artifact of each restored region and the ratio between bandwidth of the BTCB matrix and the number of CBs in BTCB matrix β/n is likely to become high if too many spatially invariant regions are defined, which results in poor restored image quality (The relationship between β/n and image quality will be discussed in Section 5.4.) The image quality restored by method 2) is unlikely to become poor compared to method 1) because low β/n ratio is guaranteed.

5.4 Results and Discussions

5.4.1 Deblurring of blurred images produced by 4.5mm double convex single lens

In this section, image deblurring simulation on blurred image produced by 4.5mm double convex single lens will be introduced and the results will be discussed. The radially blurred images are created by CODE V 2D image simulation. In this simulation, an aberration free two-dimensional image is regarded as the object. The optical design software: CODE V simulates the real situation where there is a single lens and the object and output the resulting image. The single lens imaging system for the simulation is illustrated in Fig.5.2. In the simulation, the objects are monochromatic test images generated by computer and RGB true color photographs with black background around the four sides of them. The total size of the object is 1024 ×1024. The maximum field angle is 21 degree. It should be emphasized PSFs at field angles that are larger than 21 degree will results in inaccurate assessment of blurred image quality. We know it by a warning message of CODE V, which says" this system is not isoplanatic at field angles larger 21 degree. Any PSF results are of questionable value for assessing the image quality. The image quality for the unacceptable fields varies significantly over a lateral region of 12 Airy disc diameters." Therefore the maximum field angle is 21 degree.

The simulation consists of the following six steps:

1) Input the aberration-free 2D image to CODE V and output the blurred Cartesian image.

2) Convert the blurred Cartesian image to polar image using the algorithm introduced in section 5.3.2.
3) Determine the number of spatially invariant regions for the polar image and select PSF at a certain field angle within each region.
4) Convert Cartesian PSF to polar PSF for each region using algorithm introduced in section 5.3.3, PSF pixel size has to match the image pixel size before the conversion.
5) Deblur the radially blurred image created in step 1) by method introduced in Section 5.3.5. For deblurring method 1) introduced in the 2nd paragraph of Section 5.3.5, region boundary expansion is necessary during the deconvolution in order to avoid boundary artifact.
6) Crop the black background of the deblurred image

Fig.5.19 shows the reason why the aberration-free image should have the black background around the four sides. The squared area with slash lines indicates the actual image size (without black background). The blurred image is created by convolving the aberration-free image and PSFs. There is no problem for pixels of the blurred image in the interior Cartesian image region. However, those located in the exterior Cartesian image region are obtained by convolving with some pixels in the interior Cartesian image region as shown in Fig.5.19. The influence of these pixels results in non-zero pixels of the blurred image in the exterior Cartesian image region. Therefore, directly convert from Cartesian image to polar image without a larger background will lose those non-zero pixels in the blurred polar image.

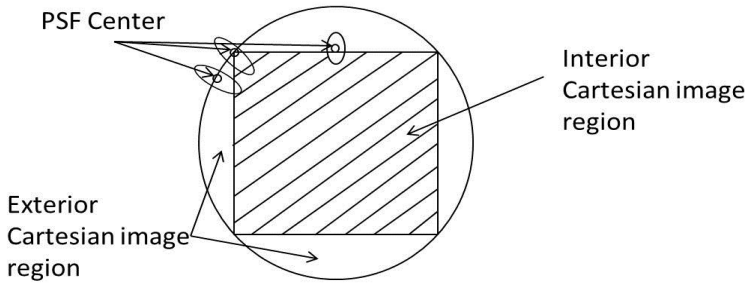

Fig.5.19 Convolution between the aberration-free image and PSFs

In step 2) and 4), the unit of PSFs and blurred image measured in CODE V is in millimeter while the deblurring process requires unit of the PSF and image in pixels. Therefore, a unit conversion is necessary before deconvolving the PSFs with the image. In addition, the PSF is also finer than the image so that adjusting the PSF pixel size to match the image pixel size is also necessary. The resolution of the PSF is 1024×1024 and size of each PSF pixel is 0.937μm. For the natural color photographs, we use light beams whose wavelengths range from 410nm to 700nm as the light source in order to represent visible light and deblur images using PSFs of the reference light beam: 587.6nm. The blurred image is also 1024×1024 but size of each pixel is 1.558μm. Thus the resolution of PSF in the blurred image is $1024 * 0.937/1.558 \approx 616$ pixels.

For the polar image, we can determine $r_{\max}$ and $\theta_{\max}$ by rules discussed in Section 5.3.2. The maximum index of the Cartesian image is $i_{\max} = 1024$ and $j_{\max} = 1024$. The image center index is $i_{\mathrm{c}} = 512$ and $j_{\mathrm{c}} = 512$. According to equation (5.4), we have

$$r_{\max} = \sqrt{(i_{\max} - i_c)^2 + (j_{\max} - j_c)^2} + 1 \approx 726$$

And we determine q=3600 so that $\theta_{\max}$=3600 because this number can be divided exactly by 4 and at least two polar pixels are surrounded by four neighboring Cartesian pixels (by examining the furthest pixels from the Cartesian image center, e.g. when four neighboring Cartesian pixels (1023,

1023); (1023,1024); (1024,1023); (1024, 1024) are selected, the two polar pixels inside them are (451,724) and (451,725).

In step 3), we found that region between 14 and 21 degree (The corresponding rows in the blurred polar image are $472 \ll r \ll 726$) has no more image information but zero valued pixels because of the black background in the Cartesian image. Therefore, it is actually no need to deblur this region. The rest regions of the polar image (0 ~14 degree: $1 \ll r \ll 472$) are segmented into four spatially invariant regions, and PSFs for deblurring the specific region are considered as spatially invariant. Tab.5.1 shows the detail of the four segmented regions and the corresponding PSFs. Note that in Tab.1 there is another column named "Expanded regions", which is necessary to avoid boundary ringing artifact if the deblurring is implemented by applying SIPSF to sub-regions. The boundary ringing artifact is caused by high frequency drop off at boundary pixels where there is sharp intensity contrast in the image when using FFT. The padding from BTCB to BCCB equals to adding additional rows to the polar image and replicating the polar image (Refer to Fig.5.20). If pixels around those boundaries have sharp intensity drop, ringing artifact occurs near them. That is why the regions must be expanded. Same reason applies to the object in the image. If the object has sharp intensity drop compared with the background, ringing artifact will occurs when using the FFT deconvolution.

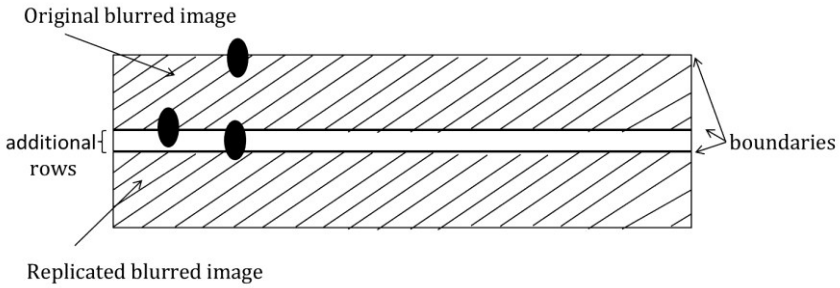

Fig.5.20 Boundary ringing artifact

Tab.5.1 Spatially Invariant field regions, their expanded regions and PSFs

Field regions (degree)	Expanded regions(degree)	PSFs at which field angle (degree)
0~3 (r1 ~r101)	0~4 (r1 ~r134)	3
3~6 (r101 ~r202)	2~7 (r67 ~r235)	6
6~10 (r202 ~r336)	5~11 (r168 ~r370)	9
10~14 (r336 ~r472)	9~15 (r303 ~r506)	10
14~21 (r472~r726)		

In Tab.5.1, "*r*" indicates row of the polar image. The PSFs in the third column were selected within each spatially invariant field region listed in the first column. If the deblurring is realized by applying SIPSF to sub-regions, the determination of appropriate PSF for each region is an important issue. Generally, any PSF can be selected if the field region is not large (For example, not larger than 7 degree field angles), which means the PSF does not change dramatically. However, the larger the PSF, the stronger the ringing artifact will appear in the deblurred region, especially at high field regions. Therefore we tend to select PSF at low field angle for a high field region: e.g. PSF at 10 degree is selected to deblur field region 10~14 degree.

Fig.5.21 uses a real image example to explain the deblurring method

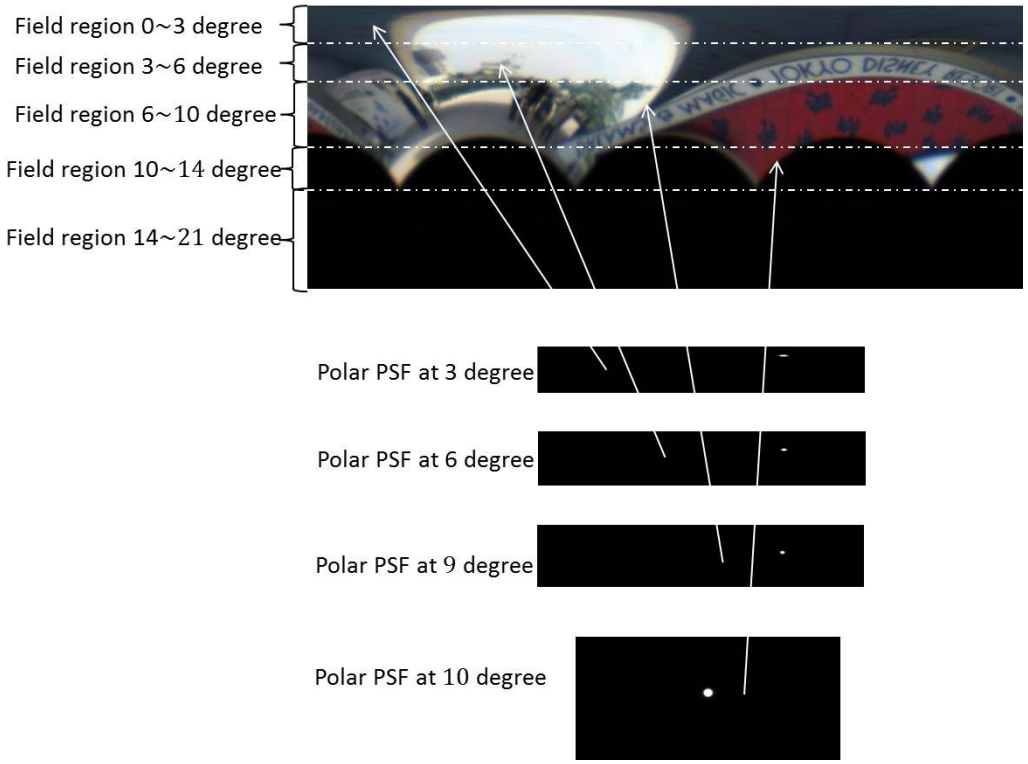

Fig.5.21 Panorama of the blurred polar image and the field regions to be deblurred using polar PSFs

Fig.5.22 to Fig.5.25 demonstrates the deblurring results for four RGB color photograph examples by using the deblurring method that applies SIPSF to sub-regions.

(a) Original image (b) Blurred image (c) Deblurred using 4 PSFs (d) Deblurred using single PSF

(e) Deblurred without larger black background (f) Deblurred without boundary expansion (g) Blurred area 1 enlarged (h)Deblurred area 1 enlarged

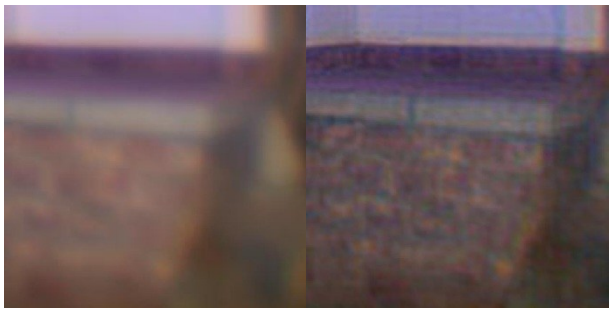

(i) Blurred area 2 enlarged (j) Deblurred area 2 enlarged

Fig.5.22 Color photograph 1

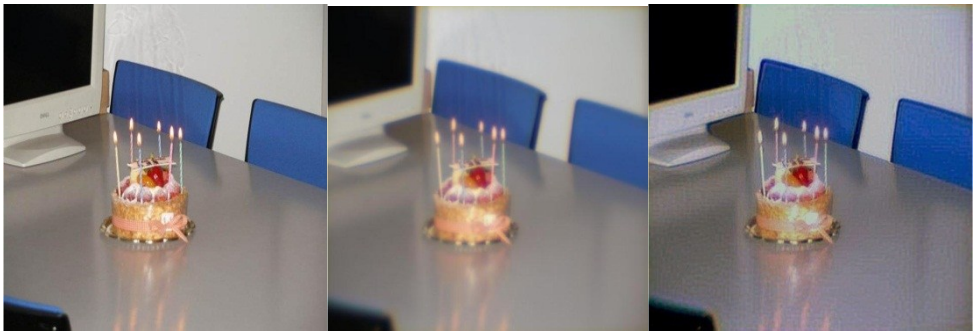

(a) Original image (b) blurred image (c) Deblurred using 4 PSFs

Fig.5.23 Color photograph 2

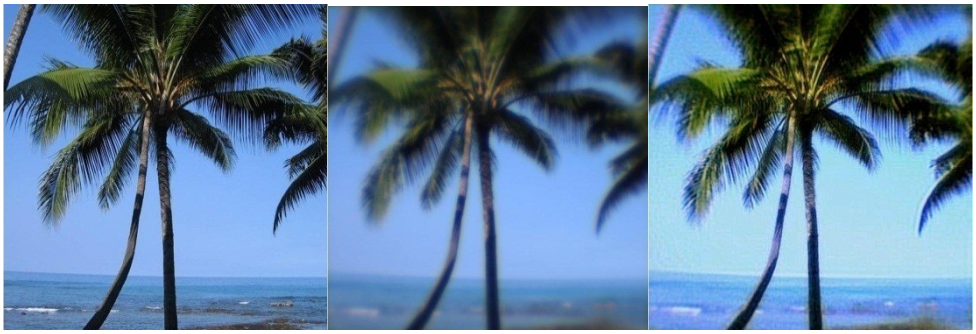

(a) Original image (b) blurred image (c) Deblurred using 4 PSFs

Fig.5.24 Color photograph 3

(a) Original image (b) blurred image (c) Deblurred using 4 PSFs

Fig.5.25 Color photograph 4

Fig.5.26 to Fig.5.30 show the deblurring results for two monochromatic images and three RGB color photographs by using deblurring method that applies SIPSF to whole image.

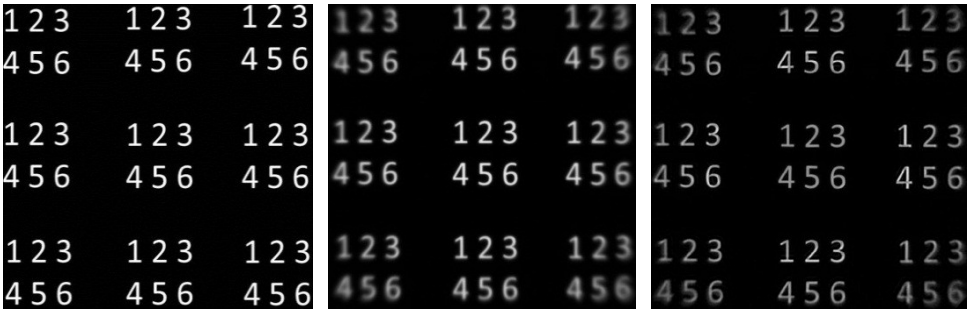

(a) Original image (b) blurred image (c) deblurred image

Fig.5.26 Deblur of monochromatic image 1

(a) Original image blurred image (c) deblurred image

Fig.5.27 Deblur of monochromatic image 2

(a) Original image (b) blurred image (c) deblurred image

Fig.5.28 Deblur of color image 1

(a) Original image (b) blurred image (c) deblurred image

Fig.5.29 Deblur of color image 2

(a) Original image (b) blurred image (c) deblurred image

Fig.5.30 Deblur of color image 3

In Fig.5.22 to Fig.5.25, (a) shows the original image that is aberration free, (b) is the radially blurred image produced by the single lens system (Note that it also includes distortion and chromatic aberration.) and (c) shows the deblurred resulting image using four spatially invariant PSFs for four segmented field regions listed in Tab.5.1. In Fig.5.22, we also give the resulting images by different simulation conditions in order to compare with the four PSFs case. (d) shows the resulting image by applying single PSF (PSF at field angle 10 degree) to the whole image. Although the high field region deblurring is visually acceptable, the low field regions did not obtain satisfactory result: The ringing artifact becomes stronger around the center of the deblurred image than the far-from-center area. This attributes to inaccurate approximation of real radially variant PSFs at low field regions. In other words, the real PSFs change dramatically throughout the whole image (0~21 degree) (Refer to Fig.5.4) so that applying single PSF to whole image deviates too much from real PSFs. Fig.5.22(e) illustrates the deblurred resulting image without the black background around the four sides of the actual image, as is analyzed in Fig.5.19. Obviously, the low field regions are visually acceptable as expected while the high field regions are deteriorated by strong ringing artifact. Fig.5.22 (f) tells us the deblurred image without boundary expansion results in boundary ringing artifact at the upper and lower boundaries of each field region of the polar image. The boundary artifact is visible when the deblurred regions are connected together. In addition, the boundary ringing artifact around high field boundaries is stronger than that at the low field boundaries because of the increasing of PSF size. Fig.5.22 (g),(h),(i) and (j) show some enlarged blurred areas and their enlarged deblurred counterparts. Fig.5.22 (g) and (i) enlarge the top right corner and bottom right corner of Fig.5.22 (b), respectively. (h) and (j) give the deblurred image for (g) and (i). By comparing different deblurred results in Fig.5.22, one can tell that the deblurred image using 4 PSFs obtained visually satisfactory image than single PSF deblurring, no black background deblurring and no boundary expansion deblurring. In order to testify the effectiveness of the proposed deblurring technique, three more color photographs are simulated by using 4 PSFs which is shown in Fig.5.23 to Fig.5.25.

The deblurring results by using deblurring method that applies SIPSF to whole image shown in Fig.5.26 to Fig.5.30 are also satisfactory. As the boundary ringing artifact no longer exists in case of this method, the deblurring process becomes simpler than deblurring method that applies SIPSF to sub-regions. It should be noted from Fig.5.22 to Fig.5.30 that deblurring of gray scale images is realized using PSFs of mono-wavelength (656.3nm), while the deblurring of color images is realized by deblurring R-plane (610nm~700nm), G-plane (510nm~600nm) and B-plane (410nm~500nm) respectively, and then synthesize them to an RGB color image. Therefore, selecting proper PSFs for each color plane is necessary. In our simulation, we applied PSFs of uniform wavelength (587.6nm) to R, G and B image planes and obtained acceptable resulting image, just for simplicity. More accurate restoration requires PSFs that belong to three different wavelengths for R,G and B plane.

As to deblurring method that applies to SIPSF to sub-regions, there is a question left regarding the number of PSFs applied to the spatially invariant field regions. How many PSFs are necessary to

deblur the radially blurred image? Will the deblurred images in Fig.5.22 to Fig.5.25 become better when more than 4 PSFs are used? Actually, this is a compromise problem between "how accurate does the PSF in each spatially invariant region represent real PSF" and "whether the field region is large or not". As we discussed in section 5.3.5, polar PSF should be transferred to a BTTB matrix form (in our case it is a BTCB matrix) to make the deblurring problem a mathematically linear system: $\tilde{F} = T^{-1}G$. where $\tilde{F}$ means deblurred image vector, T is the PSF BTCB matrix whose No. of elements is $nm \times nm$ and G is the blurred image vector whose No. of elements is $nm \times 1$. n and m are the number of rows and columns of the panoramic polar blurred image, respectively. The regularized version of the above equation is as follows:

$$\tilde{F} = (T^*T + \alpha L^*L)^{-1}T^*G \tag{5.19}$$

where α serves as the regularization parameter and L is the regularization operator. "*" is the symbol for conjugate transpose. The above equation can be rewritten by the following equation in order to simplify the computation by using FFT

$$\tilde{F}_e = (C_T^*C_T + \alpha C_L^*C_L)^{-1}C_T^*G_e \tag{5.20}$$

where C_T is a BCCB padded from T and its No. of elements is $(n+\beta)m \times (n+\beta)m$. G_{e} is the extended blurred image vector padded from G and suppose it is an zero-padding: $G_{\mathrm{e}} = \begin{pmatrix} G \\ G_p \end{pmatrix} = \begin{pmatrix} G \\ 0 \end{pmatrix}$. The No. of elements of G_p is then $\beta m \times 1$. Here β is known as the bandwidth of the BTCB matrix. The bandwidth can also be considered as the number of Circulant Blocks (CBs) to be padded to a BTCB in order to form a BCCB. $\tilde{F}_e$ can be written as

$$\tilde{F}_e = \begin{pmatrix} \tilde{F}_{e1}^{\,nm\times 1} \\ \tilde{F}_{e2}^{\,\beta m\times 1} \end{pmatrix}$$

where the superscript means No. of elements, Here $\tilde{F}_{e1}$ approximately equals to $\tilde{F}$ when a condition is satisfied: the bandwidth β is relatively small compared to n. To verify this, we could write the BCCB matrix in the following block matrix form which includes the BTCB matrix and three additional block matrices

$$C_T = \begin{pmatrix} T^{\,n\times n} & T_{12}^{n\times\beta} \\ T_{21}^{\beta\times n} & T_{22}^{\beta\times\beta} \end{pmatrix}$$

Note that the superscript means No. of CBs, not the No. of matrix elements this time. For simplicity, L is an identity matrix that has same size as T so that we have

$$C_L = \begin{pmatrix} I^{\,n\times n} & 0 \\ 0 & I^{\,\beta\times\beta} \end{pmatrix}$$

Then we have the similar derivation as introduced in [5-9] as follows:

$$(C_T^*C_T + \alpha C_L^*C_L)^{-1} = \begin{pmatrix} M^{\,n\times n} & M_{12}^{n\times\beta} \\ M_{21}^{\beta\times n} & M_{22}^{\beta\times\beta} \end{pmatrix}$$

where $M,\ M_{12},\ M_{21},\ M_{22}$ are also BTCBs. And

$$(C_T^*C_T + \alpha C_L^*C_L) = \begin{pmatrix} T^*T + T_{21}^*T_{21} + \alpha I & T^*T_{12} + T_{21}^*T_{22} \\ T_{12}^*T + T_{22}^*T_{21} & T_{12}^*T_{12} + T_{22}^*T_{22} + \alpha I \end{pmatrix}$$

Since

$$(C_T^* C_T + \alpha C_L^* C_L)^{-1}(C_T^* C_T + \alpha C_L^* C_L) = I$$

we have

$$\begin{pmatrix} M^{n\times n} & M_{12}^{n\times\beta} \\ M_{21}^{\beta\times n} & M_{22}^{\beta\times\beta} \end{pmatrix}\begin{pmatrix} T^*T + T_{21}^*T_{21} + \alpha I & T^*T_{12} + T_{21}^*T_{22} \\ T_{12}^*T + T_{22}^*T_{21} & T_{12}^*T_{12} + T_{22}^*T_{22} + \alpha I \end{pmatrix} = \begin{pmatrix} I & 0 \\ 0 & I \end{pmatrix} \quad (5.21)$$

by which we obtain

$$M(T^*T + T_{21}^*T_{21} + \alpha I) + M_{12}(T_{12}^*T + T_{22}^*T_{21}) = I \quad (5.22)$$

The maximum rank of $T_{21}^*\,T_{21}$ and the second term in (5.22) is β. If β is relatively small compared to n , (5.22) approximately equals to

$$M(T^*T + \alpha I) = I$$

Therefore we have

$$M = (T^*T + \alpha I)^{-1} \quad (5.23)$$

From (5.20) we know that

$$\tilde{F}_e = (C_T^* C_T + \alpha C_L^* C_L)^{-1} C_T^* G_e =$$
$$\begin{pmatrix} M & M_{12} \\ M_{21} & M_{22} \end{pmatrix}\begin{pmatrix} T^* & T_{21}^* \\ T_{12}^* & T_{22}^* \end{pmatrix}\begin{pmatrix} G \\ 0 \end{pmatrix} =$$
$$\begin{pmatrix} (MT^* + M_{12}T_{12}^*)G \\ (M_{21}T^* + M_{22}T_{12}^*)G \end{pmatrix} \quad (5.24)$$

The maximum rank of $M_{12}T_{12}^*$ is also β, its No. of CBs is $n \times n$. So that

$$(MT^* + M_{12}T_{12}^*)G \approx MT^*G \quad (5.25)$$

when β is relatively small compared to n.

Substitute (5.23) into (5.25), we have

$$MT^*G = (T^*T + \alpha I)^{-1}T^*G = \tilde{F}$$

which means $\tilde{F}_{e1} \approx \tilde{F}$.

Then we derive the simplified FFT calculation from (5.20) as follows:

C_T and C_L can be decomposed into C_T=$Ft^*\Lambda_T\,Ft$ and C_L=$Ft^*\Lambda_L\,Ft$, where Λ_T and Λ_L indicate diagonal matrices that include the eigenvalues of C_T and C_L, respectively. Ft is the unitary discrete Fourier transform matrix, which has the characteristic of Ft^*=Ft^{-1}. Then (5.20) can be rewritten as

$$(C_T^* C_T + \alpha C_L^* C_L)^{-1} C_T^* G_e = Ft^*(|\Lambda_T|^2 + \alpha|\Lambda_L|^2)^{-1}\Lambda_T^* Ft G_e. \quad (5.26)$$

Since the eigenvalue of a BCCB matrix can be obtained by FFT of its first column and the matrix-vector multiplication involving a BCCB matrix could be simplified to component-wise multiplication using only first column of BCCB matrix, we have

$$\tilde{F}_e = ifft\,\{1./([fft(c_T)]^2 + \alpha[fft(c_L)]^2).\bullet\,[fft(c_T)]^*.\bullet\,fft(G_e)\} \quad (5.27)$$

where fft and $ifft$ mean FFT and inverse FFT, respectively and c_T, c_L are first column of C_T and C_L, respectively. Here the operators "./" and ".•" indicate component-wise division and multiplication, respectively.

By now it is clear that the simplified FFT calculation using (5.27) obtains good deblurred result only if β is relatively small compared to n. This is an essential factor affecting the deblurred image quality.

The relationship between n and β can be further examined by Fig.5.20, the No. of rows in the panoramic polar blurred image equals to n and the No. of additional rows equals to β. Therefore, applying a single PSF to a large field region (with bigger n) will obtain a deblurred vector near $\tilde{F}$. However, large field region also means dramatic PSF change, in which the single PSF cannot represent the real PSF. As a result, it becomes a compromise problem as we mentioned above. In our simulation, the polar blurred image was segmented into 4 regions. The No. of rows for each region and the No. of additional rows are listed in Tab.5.2. The ratio β/n is used to examine the relationship between β and n. The reason why we did not segment the blurred image into more than 4 regions is that the ratio β/n will become higher for each region.

Tab.5.2 No. of rows of each field region, No. of padded rows and their ratio

Field region	n	β	$\beta/$ n
0°~3°	134	11	8.2%
3°~6°	169	15	8.9%
6°~10°	203	20	9.9%
10°~14°	204	23	11.3%

5.4.2 Deblurring of blurred images produced by 1.0mm plano-convex single lens

In this sub section, deblurring of blurred images produced by 1.0mm plano-convex is implemented. The structure and specifications of the 1.0mm lens can be found in Section 2.2 of Chapter 2. We evaluate the deblurring results by visual comparisons among different deblurred images using different number of PSFs and resolution of the polar image. Additionally, quantitative evaluation using Mean Square Error (MSE) is carried out for polar images whose resolutions are 726×1800. Similar to the simulation using 4.5mm lens, the blurred images were generated by 2D image simulation of CODE V. Three color images were used for evaluation, of which the Cartesian image resolutions are 1024×1024, but this time the semi-maximum field angle reached 48 degree compared to 21 degree of the 4.5mm lens simulation. In order to avoid strong boundary ringing artifact after image deblurring, we also put the original image into a larger black background. Simulation procedures are similar to that of the 4.5mm lens simulation except the fifth step, in which only the deblurring method 2) introduced in the second paragraph of Section 5.3.5 was used.

A unit conversion from millimeter to pixel is indispensable before deblurring. It is also necessary to adjust the PSF pixel size to match the size of image pixel. The resolution of PSF is 1024×1024 and size of each PSF pixel is 0.4μm×0.4μm. Each pixel size of blurred image is 0.814μm×0.814μm. Therefore, the number of pixels of PSF in the blurred image is $(1024 \times 0.4/0.814)^2 \approx 503^2$.

We converted blurred image from Cartesian coordinate system to polar coordinate system using

different polar image resolution in order to investigate the difference in visual comparisons. One converted polar image has 726×1800 pixels and the other has 726×3600 pixels. The determination of $r_{\max}$ and $\theta_{\max}$ is based on the rule described in Section 5.3.2. We found that at least two polar pixels are surrounded by four neighboring Cartesian pixels (by examining farthest pixels from Cartesian image center, e.g. when four neighboring Cartesian pixels (1023, 1023), (1023, 1024), (1024, 1023), (1024, 1024) are selected, the polar pixels inside them are (724,226), (725,226) and (724,451), (725,451) for 726×1800 and 726×3600 polar image, respectively.

The four vertexes of the blurred image with black background correspond to semi-maximum field angle 48 degree and the region between 30 degree and 48 degree has no image information because of the black background. Therefore, we segmented the blurred image from 0 degree to 30 degree. In this simulation, we observe the deblurring results by applying different number of PSFs to different number of segmented regions. The image was segmented into 3, 5, 8 and 10 regions, to which the same number of PSFs was applied. The deblurred result without image segmentation and by using single PSF was also compared.

MSE were calculated between original image and deblurred images by

$$\mathrm{MSE} = \frac{1}{nm}\sum_{i=1}^{n}\sum_{j=1}^{m}\left|o(i,j) - r(i,j)\right|^2 \tag{5.28}$$

where $o(i,j)$ and $r(i,j)$ indicate pixels of original and restored image, respectively. n and m define resolution of the original and restored image. Note that MSE for the color image is a summation of individual MSEs calculated for R, G and B plane separately.

Visual comparisons for color image 1 to 3 are shown from Fig.5.31 to Fig.5.33. In each figure, we compare original, blurred and restored images using single PSF, 3PSFs, 5PSFs, 8PSFs and 10PSFs. The Polar Image Resolution or PIR are directly written under each restored image and MSEs are added to those using PIR=726×1800 so that the visual and quantitative results can be compared simultaneously. To observe details of the deblurred image, we enlarge some regions and compare them with the enlarged regions of blurred image.

The graphs showing MSE vs. No. of PSFs were drawn separately for each of the three color images in Fig.5.34. β/n ratios vs. No. of PSFs were also added in Fig.5.35 in order to investigate their effect on MSE. These ratios are summation of separate β/n ratio of PSF BTCB matrix used to deblur each spatially invariant region.

Original

Blurred

Restored using single PSF

PIR=726×1800, MSE=0.0715

Restored using 3PSFs

PIR=726×1800, MSE=0.0541

Restored using 5PSFs

PIR=726×1800, MSE=0.0531

Restored using 8PSFs

PIR=726×1800, MSE=0.0528

Restored using 10PSFs

PIR=726×1800, MSE=0.0556

Restored using 3PSFs

PIR=726×3600

Regions to be enlarged

PIR=726×3600

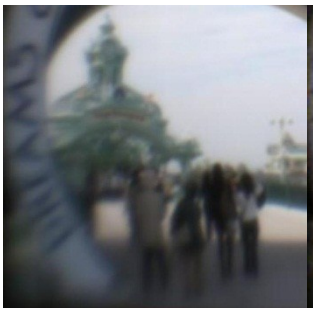

Enlarged blurred region 1

Enlarged deblurred region 1

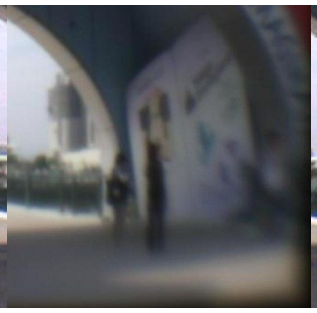

Enlarged blurred region 2

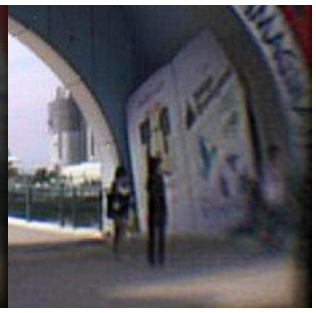

Enlarged deblurred region 2

PIR=726×1800

PIR=726×3600

Fig.5.31 Deblur of color image 1

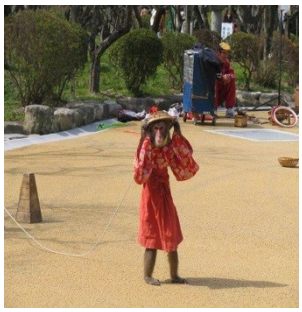

Original

Blurred

Restored using single PSF

PIR=726×1800, MSE=0.1081

Restored using 3PSFs

PIR=726×1800, MSE=0.0788

Restored using 5PSFs

PIR=726×1800, MSE=0.0785

Restored using 8PSFs

PIR=726×1800, MSE=0.0747

Restored using 10PSFs

PIR=726×1800, MSE=0.0786

Restored using 3PSFs

PIR=726×3600

Regions to be enlarged

PIR=726×3600

Enlarged blurred region 1

Enlarged deblurred region 1

Enlarged blurred region 2

Enlarged deblurred region 2

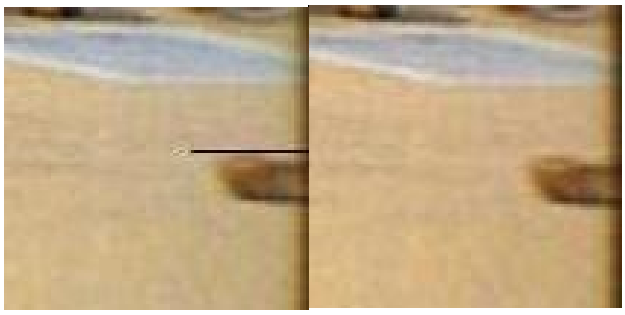

PIR=726×1800 PIR=726×3600

Fig.5.32 Deblur of color image 2

Original

Blurred

Restored using single PSF

PIR=726×1800, MSE=0.1593

Restored using 3PSFs

PIR=726×1800, MSE=0.1449

Restored using 5PSFs

PIR=726×1800, MSE=0.1464

Restored using 8PSFs

PIR=726×1800, MSE=0.1417

Restored using 10PSFs

PIR=726×1800, MSE=0.1453

Restored using 3PSFs

PIR=726×3600

Regions to be enlarged

PIR=726×3600

Enlarged blurred region 1 | Enlarged deblurred region 1 | Enlarged blurred region 2 | Enlarged deblurred region 2

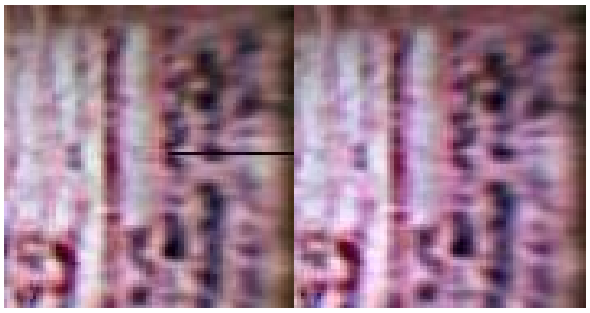

PIR=726×1800 PIR=726×3600

Fig.5.33 Deblur of color image 3

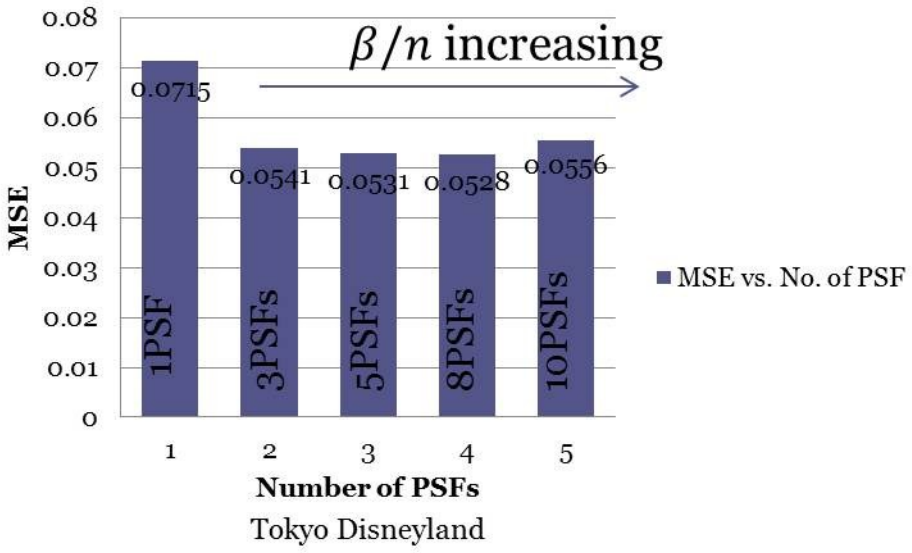

(a)

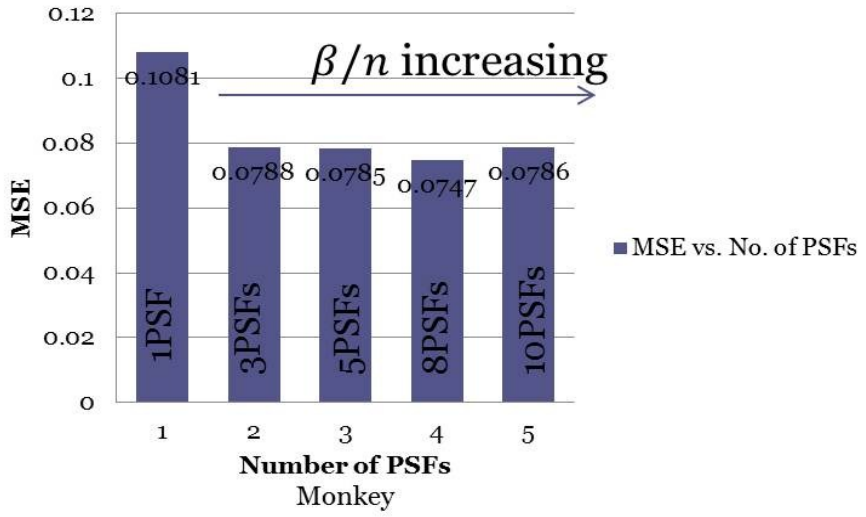

(b)

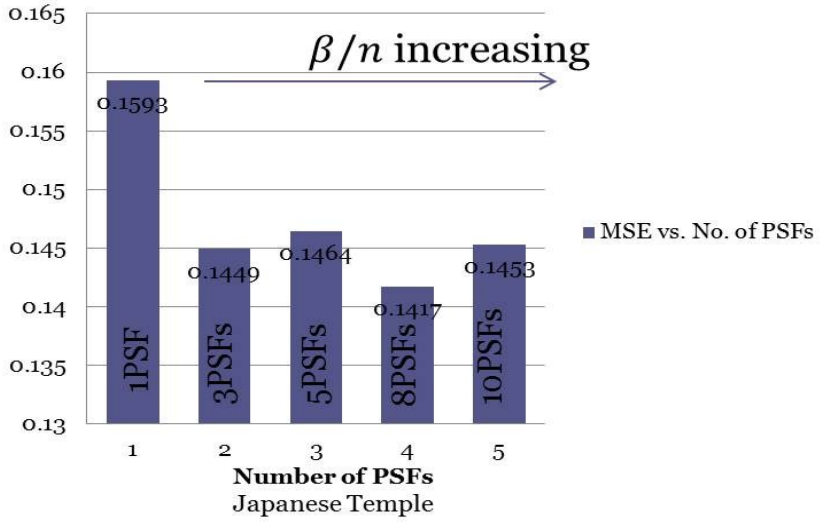

(c)

Fig.5.34 MSE versus number of PSFs, PIR=726×1800

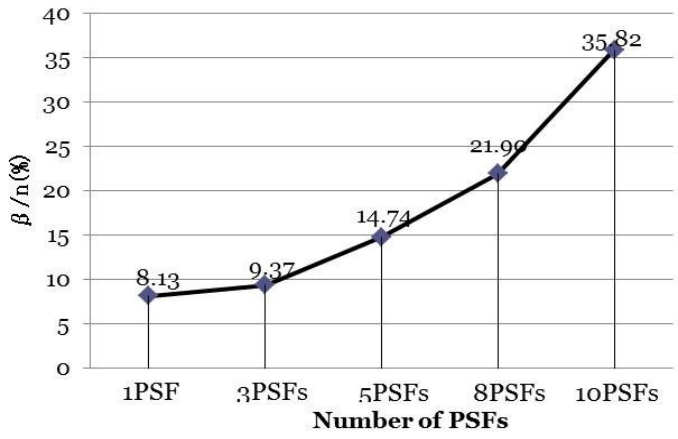

Fig.5.35 β/n ratio versus number of PSFs

According to the results shown from Fig.5.31 to Fig.5.35, the deblurred images using PIR=726×3600 obtained visually better results than those using PIR=726×1800. Although both of them obey the rule that at least one polar pixel should be located inside four Cartesian pixels, the former obtained good pixel continuity whereas the latter had a black region near the right border, which indicates pixel vacancies (shown in the last two enlarged sub images of Fig.5.31, Fig.5.32 and Fig.5.33). This suggests that increasing polar image resolution results in better pixel continuity.

In Fig. 5.34(a), quantitative evaluation revealed that MSE declined from 0.0715 of 1PSF to 0.0528 of 8PSFs and rose again to 0.0556 of 10PSFs. Similar tendencies can be found in Fig. 5.34(b) and (c), except that a slight rising was detected from 3PSFs to 5 PSFs in (c). The β/n ratio increased continuously from 8.13% of 1PSF to 35.82% of 10PSFs for all three color images along with the increment of number of PSFs as shown in Fig.5.35. The effect of β/n and number of PSFs on MSE is now clear that when number of PSFs and β/n is small, the change of real radially variant PSF as the field angle increases (Fig.5.4) cannot be accurately reflected; when number of PSFs and β/n rise to high values (such as 10PSFs), the FFT calculation using (5.27) for BTCB matrices of high field angle PSFs (e.g. PSF at 27 and 30 degree) obtains unsatisfactory deblurred results because β is not relatively small compared to n, which has been proved an essential factor affecting the deblurred image quality in Section 5.4. Compared to PSF at low field angles, these high field angle PSFs contribute much to the deterioration of whole deblurred image, thus high MSE was obtained.

5.5 Conclusion

This chapter introduced a deblurring method for radially variant blurred image that is produced by single lens system. This type of radial blur occurs because of inherent optical defect of single lens, not because relative motion between camera and object. This method converts blurred image and PSFs from Cartesian coordinate system to polar coordinate system, by which the deblurring problem becomes a locally Spatially Invariant (SI) problem. The polar PSF then becomes a BTCB matrix. The deblurring was based on constrained least-square method using FFT. Simulations using 4.5mm double convex single lens have been carried out on monochromatic image and natural color photographs. Two deblurring methods were implemented and satisfactory results were obtained for both methods. As to the deblurring method by applying SIPSF to sub-regions, four PSFs applied to four segmented spatially invariant regions obtained visually the best deblurred image compared to the single PSF deblurred image, the deblurred image without a larger black background and the deblurred image without boundary expansion. Further segmenting the blurred image to more than four regions will be undesirable because of high β/n ratio. In the simulation using 1.0mm plano-convex lens, visual and quantitative evaluation using MSE showed that deblurred image using 8PSFs obtained smallest MSE and best image quality compared to that using single PSF, 3PSFs, 5PSFs and 10 PSFs. Deblurred image using polar image resolution (PIR) 726×3600 outperformed that using PIR=726×1800 in that the latter generated a visually discontinuous region around the right border due to the insufficiency of polar image pixels.

5.6 References

[5-1] Webster, C.B., Reeves, S.. "Radial deblurring with FFTS", Proc. ICIP Internat. Conf. of Image Process, Sant Antonio, USA (2007)

[5-2] R.H.Chan, J.G. Nagy and R.J. Plemmons. "FFT-based preconditioners for Toeplitz-block least-squares problems", SIAM J. Numer. Anal.,30,no.6, 1740-68 (Dec.1993)

[5-3] S.Rathee, Z.J. Koles. "Image Restoration in Computed Tomography: Restoration of Experimental CT Images", IEEE Trans. on Med. Imaging, 11 , 546-553(Dec. 1992)

[5-4] G.J.Tee, "Eigenvectors of block circulant and alternating circulant matrices", Res. Lett.Inf.Math.Sci.,8. 123-142(2005)

[5-5] C.Yang, E.G.Ng and P.A.Penczek. "Matrix-free constructions of circulant and block circulant preconditioners", Numer Linear Algebra Appl. 11:773-793 (2004)

[5-6] T.F.Chan, "Circulant preconditioners for Toeplitz-block matrices", Numerical Algorithms 6. 89-101(1994)

[5-7] A. K. Katsaggelos, J. Biemond,R.W. Schafer, and R. M . Mersereau, "A Regularized Iterative Image Restoration Algorithm", IEEE Trans. on Image Processing 39(4). 914-929 (Apr.,1991)

[5-8] R. W. FREUND, G. H. GOLUB, AND N. N. NACHTIGAL, "Iterative solution of linear systems", Acta Numerica, 57- 100(1991)

[5-9] M. Hanke and J.G. Nagy, "Toeplitz approximate inverse preconditioner for banded Toeplitz matrices", Numer. Algorithms 7, 183–199(1994)

[5-10] S. J. Reeves, "Fast image restoration without boundary artifacts", IEEE Transactionson Image Processing, 14-10, 1448–1453(2005)

[5-11] H.C.Andrews, B.R.Hunt, "Digital Image Restoration", Prentice–Hall, Englewood Cliffs, NJ,
(1977)

[5-12] M. Takagi, H. Shimoda, "Handbook of Image Analysis", University of Tokyo Press, Tokyo (1991) (in Japanese)

Chapter 6 Experiment using real single lens system

Chapter 6 Experiment using real single lens system

6.1 Introduction

In previous chapters, we have introduced aberration correction methods for a virtual single lens system created by optics design software CODEV and carried out simulations on this virtual system. Although the simulation results showed satisfactory aberration corrected and blur restored images, it is highly desirable that those aberration correction methods be testified on a real system. In this chapter, we introduce a real double-convex spherical single lens system that is developed in our laboratory and evaluate our aberration correction algorithms on this real system. Since this system is designed for a maximum semi-field angle 22 degree, distortion and chromatic aberration are almost undetectable compared with the radially variant blur phenomenon. Therefore, we mainly evaluate the blur restoration algorithm in this chapter. It should be mentioned that we are planning to build a real plano-convex single lens system, which is capable of reducing the overall thickness to approximately 1.0mm. However, as the image sensor required for the new single lens has a diagonal dimension of 1.18mm (to the best of our knowledge, the current smallest image sensor type 1/8 ″ has a diagonal dimension of 2.00mm) and the resolution should be at least 3Megapixels, which is not possible to be manufactured yet, we used a large image sensor with a large single lens system instead. The detailed structure and specification will be given in Section 6.2.

The structure of this chapter is as follows: firstly, we illustrate the schema of the double convex spherical single lens and the CMOS image sensor attached to the real camera module, together with their specifications. Then we describe each part of the camera module by showing top and side view photos. Secondly, we give an improved restoration algorithm that is based on the polar domain deconvolution method introduced in Chapter 5, by which the radial and rotational resolution of the blurred polar image can be increased. The comparison between simulation results and experimental results using the proposed deblurring method is implemented afterwards, followed by a discussion and some aspects on improvement of the current system. Finally, we conclude this chapter by a brief summary.

6.2 Methods

6.2.1 The real double-convex single lens system

A schematic drawing of the double convex spherical single lens is shown in Fig.6.1 and dimensions of the attached CMOS image sensor is demonstrated in Fig.6.2. Lens specifications are both marked on the corresponding positions of Fig.6.1 and listed in Tab.6.1.

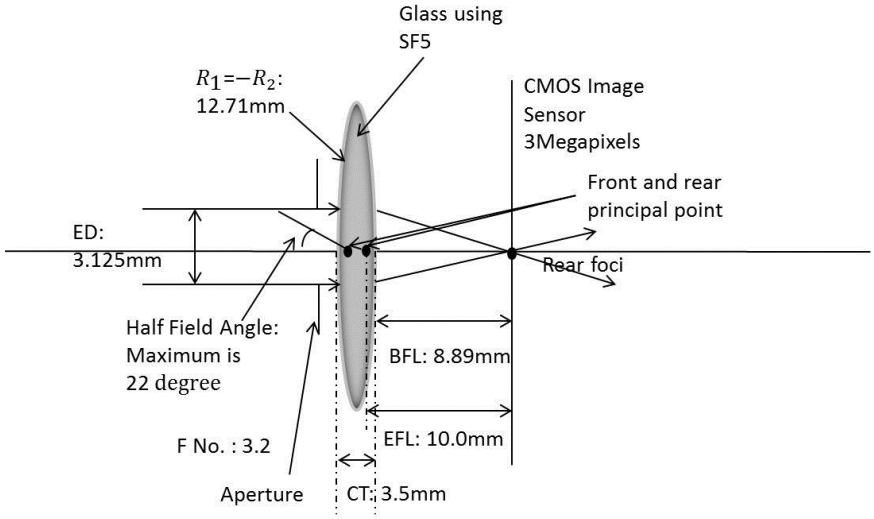

Fig. 6.1 Schema of the double convex spherical single lens

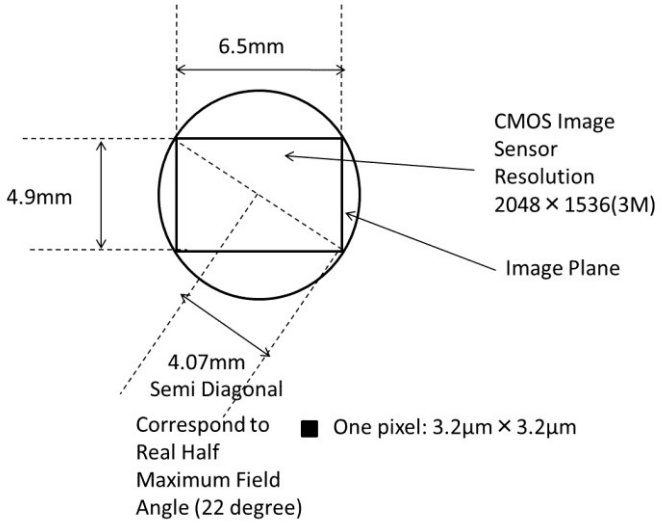

Fig.6.2 The CMOS image sensor attached to the camera module

Tab. 6.1 Lens Specifications

Glass material	SF5
Lens diameter (mm)	10.00
Effective Diameter (ED) or entrance pupil diameter (mm)	7.00
Effective Focal Length (EFL) (mm)	10.00
Back Focal Length (BFL) (mm)	8.89
F number. (EFL/ED)	1.4
Central Thickness (CT) (mm)	3.5
Radius of curvature ($R_1 = -R_2$) (mm)	12.71
Design wavelength (nm)	587.6
Maximum semi field angle (degree)	22

As is shown in Fig.6.1 and Tab.6.1, we selected SF5 as the glass material because it has a refractive index of 1.673, higher than that of the commonly used BK7 (which is 1.517) so that shorter focal length and hence smaller thickness can be obtained. The F number (or F No.) is directly proportional

to the Effective Focal Length (or EFL) and inversely proportional to the Effective Diameter (or ED) of the single lens. Because the EFL is 10.00mm and ED is 7.00mm, the F number can be calculated by EFL/ED≈1.4. It should be emphasized that although more light enters the lens system and irradiates the image sensor according to this F number, spherical aberration is also augmented because the entrance pupil diameter is relatively large. We found that the spherical aberration is negligible when ED is reduced to approximately 3.1mm or below.

The CMOS image sensor attached to the circuit board of the single lens camera module has a horizontal dimension of 6.5mm and vertical dimension of 4.9mm. The resolution is 2048×1536 megapixels and size of each pixel is 3.2μm ×3.2μm. The semi diagonal is calculated by length and width of the sensor and corresponds to the position of the maximum semi-field angle.

The maximum semi-field angle is determined by EFL and the semi diagonal of the image sensor. Let r be the dimension of semi-diagonal and f be the EFL of the lens, an equation that defines maximum semi-field angle θ can be expressed as follows

$$\theta = \arctan\frac{r}{f} \tag{6.1}$$

We also took photos of the real single lens camera module from different directions, which are illustrated in Fig.6.3.

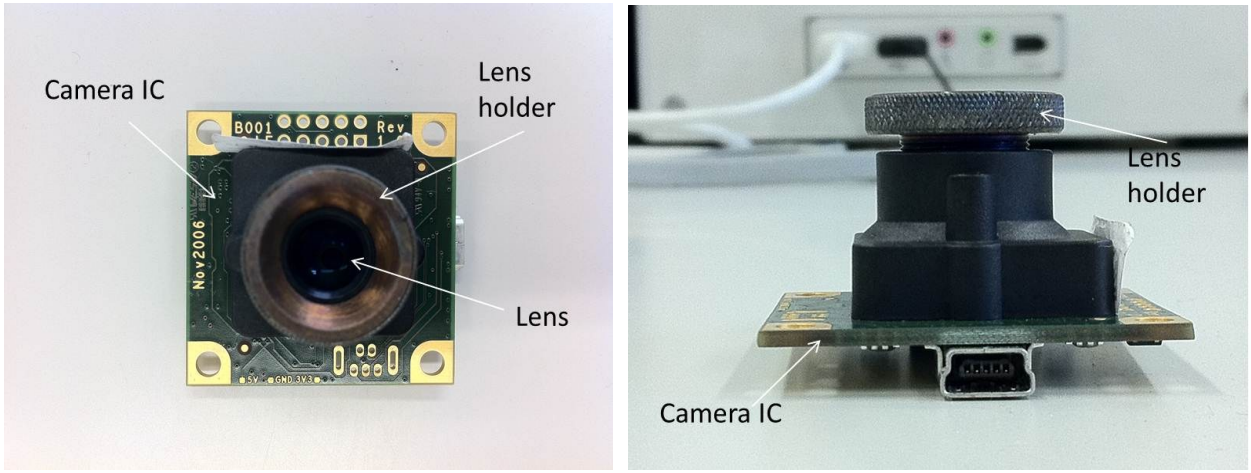

top view side view

Fig 6.3 Top and side view of the real single lens camera module

The single lens is fixed in the lens holder, which is then screwed into the camera module. The image sensor is directly under the lens and attached on the camera IC. A USB port is provided in order to view captured image on a PC. The distance between lens and image sensor is adjustable by screwing the lens holder towards to or away from the sensor. This gives us a possibility of taking in-focus photos of both nearby and distant objects. For example, when the image sensor is positioned exactly on the foci of the single lens, only object of infinite distance will be projected clearly on the image sensor. If the object is near the single lens, one has to adjust the distance between lens and image sensor to a position larger than the focal length (10mm) in order to obtain clear image. In this experiment, it is assumed that the radially variant blurred image is formed by capturing an object of infinite distance.

6.2.2 The improved blur restoration algorithm

The blur restoration algorithm used in the experiment on real single lens system is based on the polar domain deconvolution method introduced in Chapter 5, but with some improvement. Previously, we derived a set of equations that performs Cartesian to polar coordinate conversion and the inverse

conversion for blurred image and PSFs but the resolution of the Cartesian image was only 1024×1024. Since a condition has to be satisfied when converting a Cartesian image to a polar image, which depicts that there should be at least one polar pixel surrounded by four Cartesian pixels (otherwise the resolution of the polar image will be too low to obtain acceptable pixel continuity), we obtained a polar image that had 726 × 3600 polar pixels. This polar image already satisfied the above condition and was visually smooth. However, in case of the real camera system, the Cartesian image has higher resolution (2048×1536) so that we have to increase the resolution of the polar image correspondingly on both the radial and rotational directions to obtain acceptable pixel continuity. A variable k is added to previous equations to realize resolution control on radial direction. The resolution control on rotational direction is realized simply by setting the value of q. The set of equations for the current camera systems are expressed below:

Conversion from Cartesian coordinate to polar coordinate for the blurred image:

$$r = k\sqrt{(i-i_c)^2+(j-j_c)^2}+1 \tag{6.2}$$

$$\theta = \frac{q}{360}\tan^{-1}\frac{i-i_c}{j-j_c}+1 \tag{6.3}$$

Conversion from polar coordinate to Cartesian coordinate for the blurred image:

$$i = \frac{r-1}{k}\bullet\sin\frac{360(\theta-1)}{q}+i_c \tag{6.4}$$

$$j = \frac{r-1}{k}\bullet\cos\frac{360(\theta-1)}{q}+j_c \tag{6.5}$$

where $(r;\theta)$ and (i,j) represent pixel index in polar coordinate system and Cartesian coordinate system, respectively. i_c and j_c are pixel index of Cartesian image center. q is the number of equal parts that 360 degree is divided. k determines the radial resolution of the blurred polar image.

Conversion from Cartesian coordinate to polar coordinate for PSFs:

$$r' = k\sqrt{(i'+i_{psfc}-i'_{psfc}-i_c)^2+(j'+j_{psfc}-j'_{psfc}-j_c)^2}+1-r_{psfo}+r'_{psfo} \tag{6.6}$$

$$\theta' = \frac{q}{360}\tan^{-1}\frac{i'+i_{psfc}-i'_{psfc}-i_c}{j'+j_{psfc}-j'_{psfc}-j_c}+1-\theta_{psfo}+\theta'_{psfo} \tag{6.7}$$

Conversion from polar coordinate to Cartesian coordinate for PSFs:

$$i' = \frac{r'-1+r_{psfo}-r'_{psfo}}{k}\bullet\sin\frac{360(\theta'-1+\theta_{psfo}-\theta'_{psfo})}{q}+i_c-i_{psfc}+i'_{psfc} \tag{6.8}$$

$$j' = \frac{r'-1+r_{psfo}-r'_{psfo}}{k}\bullet\cos\frac{360(\theta'-1+\theta_{psfo}-\theta'_{psfo})}{q}+j_c-j_{psfc}+j'_{psfc} \tag{6.9}$$

where (r', θ') and (i', j') indicate pixel index of polar image in PSF coordinate system and Cartesian image in PSF coordinate system, respectively. $(r'_{psfo}, \theta'_{psfo})$ and $(r_{psfo}, \theta_{psfo})$ mean pixel index of polar PSF origin in PSF coordinate system and image coordinate system, respectively. (i'_{psfc}, j'_{psfc}) and (i_{psfc}, j_{psfc}) represent pixel index of Cartesian PSF center in PSF and image coordinate system, respectively.

6.3 Comparison between simulation and experiment results

In this section, we evaluate the blur restoration algorithm for the real double convex spherical single lens system introduced in Section 6.2 and compare the experiment results with the simulation

results. The object to be captured has two-dimensionality, e.g. a piece of printed paper. In this experiment, we use two printed test images as the objects. One image includes English characters and is a monochromatic image generated by computer. The other one is a RGB photograph, originally taken by stand-alone digital camera. The camera is placed approximately 450mm in front of the two-dimensional object, with the center of the 2D object aligned with the optical axis of the camera module. The experimental environment has natural light source and the room temperature is 26℃.

The blurred image taken by the real single lens camera module is then converted to polar image by equation (6.2) and (6.3) of Section 6.2. Acceptable pixel continuity is obtained by setting k=4 in equation (6.2) and rotationally segmenting the 360 degree into 7200 parts, that is, setting q=7200. Therefore the polar image resolution is 5121×7200. We did not further increase the polar image resolution because of the processing speed.

Restoration of both monochromatic image and RGB image are realized by using PSFs of the reference wavelength (587.6nm). Restoration of the RGB image has to be done separately on R, G and B color plane and synthesize a new RGB image by superimposing the R, G and B restored image.

The restoration results are shown from Fig.6.4 to Fig.6.9. Fig.6.4 to Fig.6.7 show the overall view of the blurred image and the restored image for the monochromatic and RGB color images. Additionally, Fig.6.5 and Fig.6.7 demonstrate the restoration results for the real single lens camera module introduced in Section 6.2 in order to compare with the restoration results for the virtual single lens system created by CODEV shown in Fig.6.4 and Fig.6.6. In order to examine the restored images for the real single lens system in detail, we enlarged some interested regions of Fig. 6.5 and Fig.6.7, which are shown in Fig.6.8 and Fig.6.9. Since the single lens produce a radially variant blur, which means regions far from the image center blur stronger than regions near the image center, we enlarged the upper left, upper right, lower left and lower right regions of the restored images shown in Fig. 6.5 and Fig.6.7.

The monochromatic image example:

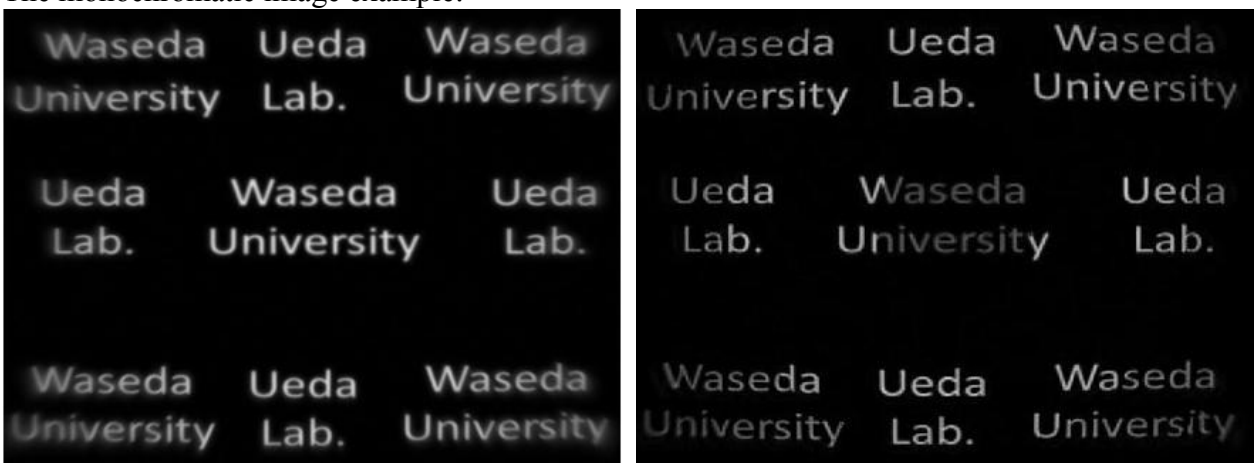

Blurred image Restored image

Fig.6.4 Restoration results for the virtual single lens system created by CODEV

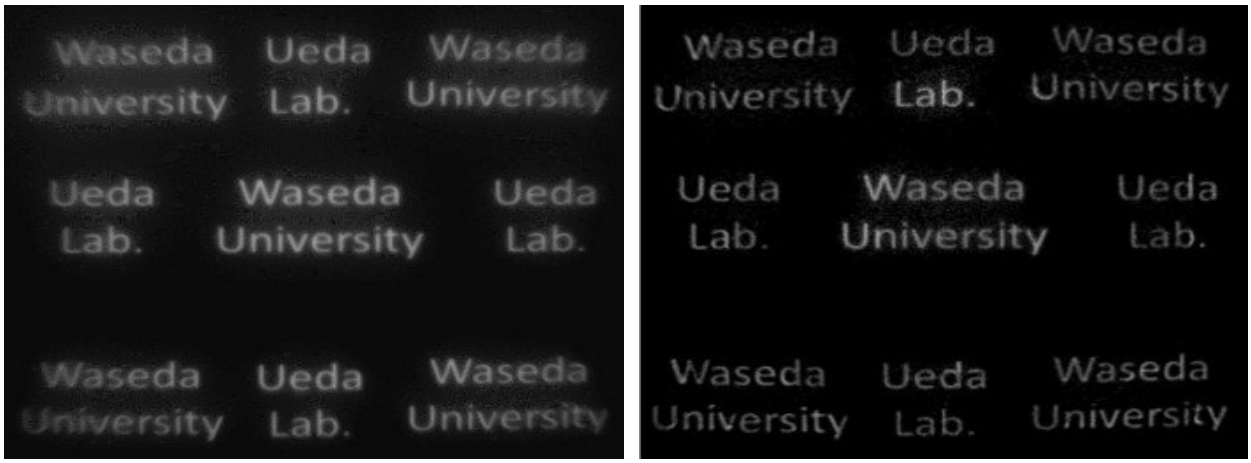

Blurred image Restored image

Fig.6.5 Restoration results for the real single lens camera module

The RGB color image example:

Blurred image Restored image

Fig.6.6 Restoration results for the virtual single lens system created by CODEV

Blurred image Restored image

Fig.6.7 Restoration results for the real single lens camera module

blurred restored blurred restored

Comparison of upper left region Comparison of lower left region

blurred restored blurred restored

Comparison of upper right region Comparison of lower right region

Fig.6.8 Zoom in of four interested regions of monochromatic image

blurred restored blurred restored

Comparison of lower left region Comparison of upper left region

blurred restored blurred restored

Comparison of upper right region Comparison of lower right region

Fig.6.9 Zoom in of four interested regions of RGB color image

The restoration algorithm is effective for both virtual single lens system and real single lens system by observing visual comparisons between blurred and restored images shown from Fig.6.4 to Fig.6.9. The restored images at the four enlarged regions all showed acceptable results. However, the restored image has very low contrast compared to the blurred image due to the implementation of regularization in the deconvolution process. Therefore, we employed an image enhancement technique to increase the contrast of the restored images.

6.4 Discussions and improvement in the future

As was mentioned in Section 6.2, diameter of the entrance pupil is relatively large compared to lens

diameter, which results in augmented spherical aberration. As a result, parallel light beams coming from different distance to the optical axis converge to different positions on the image side, which explains blurring around center of the blurred image in Fig.6.5 and Fig.6.7. This problem can be solved by decreasing diameter of the entrance pupil but it will reduce light irradiation on the image sensor simultaneously. Therefore, one has to scarify the image brightness and contrast to obtain a spherical aberration-free image. Fortunately, image enhancement could also be used in this case. In addition, we applied PSF at the design wavelength (587.6nm) to RGB image for simplicity. More precise restored image can be expected if PSFs at different wavelengths are applied to different color planes, e.g. PSFs in the range 401nm~500nm are applied to B-plane, 501nm~600nm to G-plane and 601nm ~700nm to R-plane. Moreover, we took photo on a printed paper using the real single lens camera in this experiment. In future work, experiment on a 3-dimensional spatial object that is located at a certain distance from the camera module is desirable. The spatial object can be considered a 2D object as long as it is located in a plane perpendicular to the optical axis of the camera. Finally, as to the future development of the single lens imaging system, we considered four aspects: 1) Further slimness is necessary and achievable by employing plano-convex single lens with higher refractive index such as LaSF9 (refractive index is 1.850) and smaller central thickness. We are currently developing a real cell phone camera system that could reduce the overall thickness to approximately 1.0mm. 2) Currently, the blur restoration algorithm is realized by computer program, implementation of the algorithm on a real time image signal processor (ISP) in a camera is highly desirable. 3) Incorporating other camera features such as autofocus and zooming features so as to compete with other types of next-generation camera. 4) Although the overall thickness of the camera can be reduced by employing single lens system, the overall dimension of cell phone or stand-alone camera is not easy to be reduced due to the use of silicon semiconductor technology. A promising breakthrough of semiconductor technology: Carbon nanotube (or CNT) that is in nanometer scale could probably replace silicon and achieve further minimization of the future camera phones and stand-alone cameras.

6.5 Conclusion

In this chapter, we introduced a real double convex spherical single lens system and successfully restored the radially variant blur by employing an improved algorithm based on the polar coordinate domain deconvolution method introduced in Chapter 5. Experiment on a 3Megapixels, 2D monochromatic image and a RGB photograph suggests that the blur restoration algorithm is effective on the real spherical single lens imaging system. Our next step is to fabricate a real single lens camera module for cell phones using plano-convex surface and material with higher refractive index such as LaSF9, which can reduce the overall thickness to approximately 1.0mm.

Chapter 7 Conclusions

Chapter 7 Conclusions

This chapter summarizes this study on the following three aspects: 1) originality and objectives of this research; 2) current achievements in this research; 3) future research plan for the single lens system.

The originality of this research can be summarized as follows: this study provides a new option for future cell phone camera because the number of lens elements is limited to one so that thickness of the camera could be reduced to unprecedented level by using appropriate lens. The optical aberrations caused by the single lens system can be minimized by digital image processing techniques, even if the conventional optical means is not used. Therefore, there are two objectives in this study: 1) Replace compound lens system with a spherical single lens system in order to reduce thickness of the cell phone camera; 2) Correct optical aberrations of the single lens system by using digital image processing.

In this dissertation, we demonstrated a virtual spherical single lens system designed by optics design software CODEV and successfully corrected distortion, lateral chromatic aberration and restored the radially variant blurred image for the resulting images produced by this virtual system. In addition, a real spherical single lens system was also developed to evaluate proposed algorithms and satisfactory results were obtained by experiment. These all proved the possibility of a spherical single lens system to replace the compound lens camera system.

However, this system needs further improvement such as 1) Implementation of the proposed algorithms on a real time image signal processor (ISP) in a camera. 2) Incorporating autofocus and zooming features etc. 3) Further slimness of both embedded camera and the cell phone body. With the rapid development of optical, electrical, electronics and semiconductor technology, we believe that these improvements will be realized continually in the not too distant future.

Acknowledgments

As the author of this Ph.D dissertation, I would particularly thank my supervisor, Prof. Toshitsugu Ueda, a renowned professor in the field of MEMS, sensor and sensing technology, for his direction and kind assistance in this project. It is Prof. Ueda's insightful advices and comments that facilitate the research on the single lens imaging system. Prof. Ueda has financially supported this project since 5 years ago and actively devoted himself to this project. Without his support and contribution, this research cannot be continued.

We wish to express our sincere appreciation to Prof. Hiroshi Inujima and Prof. Sei-ichiro Kamata, who are the Vice-examiners of this Ph.D dissertation. Prof. Inujima is a renowned professor and specialist in the field of machine diagnosis and spectrum analysis. Prof. Kamata is also a well-known specialist and famous for his achievements in the research discipline of image processing and pattern recognition and applications. Their comments and advices on revising this dissertation are crucial to the completion of the final version.

As a long term partner of this research since 2005, Mr. Ikumi Minema has positively participated in this project, provided useful suggestions on improving the correction algorithms, shared his creative ideas with us and most importantly, made great effort to facilitating realization of real time implementation of our algorithms on a cell phone ISP. His endeavor is highly appreciated.

We are also indebted to Prof. Lev Zimin of Kyushu Institute of Technology, who helped us build the real double convex spherical single lens module. His professional skill and experience on imaging system ensured the successful fabrication of the real lens system.

We want to express our thankfulness to Prof. Joanna Pawlat, who has been carefully reviewed and revised the dissertation.

We also would like to take this opportunity to express our gratefulness to Mr. Tsuno, a technical supporter in Ueda Laboratory, who provided powerful hardware environment for smoothly running our aberration correction algorithms.

Mr. Tomita, who is an employee in GE Corp. , has been kindly helping us revise this Ph.D dissertation. We also feel grateful to him.

Moreover, we want to thank all members of Ueda Lab., especially Dr. Satoshi, Ikezawa, who provided useful information and suggestions throughout the creation of this Ph.D dissertation.

Finally, I am grateful to my parents who gave me a desire for knowledge and courage to walk through all sorts of difficulties in my life.

Yupeng Zhang
Feb.6, 2011

Achievements

- 学術誌原著論文 (Journal Papers)
- 1. Yupeng Zhang, Toshitsugu Ueda , "Deblur of radially variant blurred image for single lens system", IEEJ Trans. Electrical and Electronic Engineering. Vol.6 S1 (Feb.,2011) (in press)
- 2. Yupeng Zhang, Toshitsugu Ueda , "Design of a singlet lens and the corresponding aberration correction approaches for cell phone camera", IEEJ Trans. Electrical and Electronic Engineering. Vol.5 No.4 (Jul.,2010), pp.474-485
- 3.Yupeng Zhang, Toshitsugu Ueda, "Field-dependent distortion coefficient and backward mapping for distortion correction of singlet lens cameras", IEEJ Trans. Electrical and Electronic Engineering.Vol.5 No.2 (Mar.,2010), pp.203-210
- 4.Yupeng Zhang, Ikumi Minema, Toshitsugu Ueda,"A texture dependent interpolation for barrel distorted and longitudinal chromatic aberrated image", IEEJ Trans. Sensors and Micromachines, Vol.128, No.11 (Nov.,2008),pp.423-430

- 査読のある国際会議、シンポジウム論文(International Conference Papers with Review)

5. Yupeng Zhang, Ikumi Minema, Lev Zimin and Toshitsugu Ueda. "A Real Double-convex Spherical Single Lens System with Blur Restoration Feature", The 2011 International Conference on Communication and Electronics Information (ICCEI 2011), Haikou, China (Feb. 22-24, 2011) (Accepted)

6. Yupeng Zhang, Ikumi Minema, Toshitsugu Ueda,"Restoration of Radially Blurred Image Created by Spherical Single Lens System of Cellular Phone Camera", IEEE Sensors 2010 Conference,Hawaii, pp.1333-1337, USA, (Nov. 1-4, 2010)

7.Yupeng Zhang, Ikumi Minema, Toshitsugu Ueda. "Geometrically distorted image correction for single lens using decimal number mapping. " Proceedings of the 10th IASTED International Conference on Signal and Image Processing (SIP2008),pp.26-31,Hawaii, USA (Aug.,2008)

8.Yupeng Zhang, Ikumi Minema, Toshitsugu Ueda , "Case analysis oriented interpolation and a two-step interpolation after correction of barrel distortion and lateral chromatic aberration," Proceedings of the 24th Sensor Symposium, pp. 236-239,Tokyo,Japan (Oct.,2007)

- 国内会議発表 (Domestic Conference Presentation)
- 9. Yupeng Zhang, Ikumi Minema, Toshitsugu Ueda, "Blur restoration for a spherical single lens system of cell phone camera", 4th IPS International Collaboration Symposium,pp.57, Fukuoka, Japan (Nov. 17-19, 2010)
- 10. Yupeng Zhang, Ikumi Minema, Toshitsugu Ueda ,"Correction of barrel distortion for simple digital camera systems," Joint Conference of Electrical and Electronics Engineers in Kyushu, pp. 470 (Sep. 2006)

受賞等 (Award)

- Finalist for IEEE Sensors 2010 Conference Best Student Paper Award